Development of T2K 280m Near Detector Software for Muon and Photon Reconstruction

Ian James Taylor

High Energy Physics
Blackett Laboratory
Imperial College London
London, UK

A thesis submitted for the degree of
Doctor of Philosophy
of the University of London
and the Diploma of Imperial College.

June 2009

Dedicated to the three people
I love the most:
my mother,
my father
and
my wife.

Abstract

A Monte Carlo investigation into the efficiencies of the electromagnetic calorimeters in T2K's off-axis near detector was undertaken. T2K is a long baseline neutrino oscillation experiment in Japan, running 295 km from the J-PARC facility in Tokai to the Super-Kamiokande detector in the Kamioka mine. The near detector will be installed on the J-PARC site during 2009, and has been designed to measure the neutrino flux, through charged current neutrino interactions, as well as the neutral current π^0 cross-section. To make these measurements, the calorimeters must reconstruct muons and photons with high efficiency, and it has been shown that 90% efficiency can be achieved for muons above 100 MeV and 80% for photons over 150 MeV. These are the two particles most important for the planned measurements; electrons are also very important and are expected to have efficiencies similar to photons. The efficiency deteriorates for particles with less energy, but this is clearly shown to be caused by the minimal signal created in the detector.

To validate the Monte Carlo characterisation of the calorimeter, the same reconstruction methods were applied to data from the SciBooNE experiment. With the aim of measuring neutrino interaction cross-sections, the SciBooNE experiment was based at FermiLab in Illinois and used the Booster Neutrino Beam. One of SciBooNE's detectors was the SciBar, a scintillating plastic detector similar in design to T2K's calorimeter. The reconstruction showed 100% efficiency for locating charged muon tracks, with excellent position and direction reconstruction, and simultaneously confirmed the reconstruction of photon showers.

Acknowledgements

I would like to thank Prof. Dave Wark; from convincing me to join T2K in my first year, through to the completion of my PhD, he has always been a source of both knowledge about and enthusiasm for neutrino physics, important qualities in any supervisor. However, no one person can provide expertise on every subject, and for that reason I was lucky to work in the T2K group at Imperial College, a team of people who all helped me frequently (and occasionally graciously). Dr. Steve Boyd, was also an excellent supervisor, before he left for pastures new, and provided a healthy amount of cynicism along with all his advice. Without the assistance of Dr. Yoshi Uchida I might not have learnt how to write code properly (i.e. in vi) or experienced quite so many karaoke bars, and without Dr. Morgan Wascko I would not have had the opportunity to join SciBooNE's pub crawl, the best London-based pub crawl I've ever been on.

Dr. Antonin Vacheret and Dr. Matt Noy were two excellent post-docs, who demonstrated how the job should be done, and I appreciate all the advice they gave me, whether it was in the lab or the pub. I hope that I live up to that example myself. Francois van Schalkwyk, joining T2K together made it easier and I enjoyed working with him over the years, not to mention the chess games.

Whilst there are far too many people within T2K to list, it is true to say that I appreciate the support and assistance from everyone. I must mention the ND280 software group, amongst whom I did the majority of my work. The work in this thesis has been tested in our meetings, and I thank everyone who provided me with (much needed) feedback and criticism. The ECal reconstruction group, Dr. Neil McCauley, Ben Still, Antony Carver, Martin Haigh and Tom Maryon, all contributed enormously, and I would not have been able to finish without that help. I would also grateful to the Stony Brook group, Prof. Chang Kee Jung, Prof. Clark McGrew, et al. for their input on my analysis and their patience towards the end.

However, I was fortunate enough to work with two collaborations during my PhD, and being part of SciBooNE was an absolute joy. I would like to thank the co-spokespersons, Prof. Tsuyoshi Nakaya and Morgan for the opportunity, without which this thesis would be two chapters shorter and a whole lot poorer. I would also like to thank Joe Walding, for taking time out of his own studies to help me with mine; I hope that he found it equally beneficial. For the rest of the collaboration, I

wish to say thank you for the warm and welcoming attitude, their enthusiasm was truly infectious and every experiment should have a social club and formal Fridays.

On a more personal note, I am grateful for my fellow Imperial students, Francois, Tom, Phil, Matt, Aaron, Claire (×2) and Anastasios. You were all there for me at one point or another, pint in hand, and I hope that I was there for you too. I'm not sure that I would have been sane at the end of my time if it weren't for you. You probably have something to add, but I'll leave it there...

And finally, I wish to thank the people closest to me. Mum and Dad, without your constant support I wouldn't have got anywhere near as far as I have. And Pam, my wonderful wife, you have done so much, and put up with so much, I couldn't ask for anything more. Thank you.

Contents

List of Figures

List of Tables

Chapter 1

Introduction to Neutrino Physics and Modern Neutrino Experiments

The T2K experiment is a next generation, long baseline, neutrino oscillation experiment based in Japan. The experiment derives its name from the beam of neutrinos it will study; the neutrinos are produced using the J-PARC accelerator at Tokai and travel 295 km to the Kamioka mine, where some will be detected by the Super-Kamiokande detector. The experiment aims to measure flavour oscillations of the neutrinos, especially searching for evidence of $\nu_\mu \rightarrow \nu_e$ oscillations.

Accelerator-based neutrino experiments have been around for some time; in 1962 a neutrino beam at Brookhaven National Laboratory was used to demonstrate that ν_e and ν_μ were different particles [1]. Since then, the technologies and techniques involved have been improved, producing much more intense and energetic neutrino beams, but the central interactions remain the same: an accelerator produces a beam of high energy pions, which decay in-flight to provide energetic muon neutrinos.

The distance from the neutrino source to the far detector, referred to as the baseline of an experiment, is varied depending on which parameters of neutrino oscillations (explained fully in section 1.3.2) it aims to measure. Short baselines are generally between 10^1 and 10^3 m, such as KARMEN (18 m from source to detector [2]), LSND

(30 m [3]) and MiniBooNE (541 m [4]). In contrast, long baseline experiments such as T2K have baselines of 10^5 to 10^6 m; specifically T2K will be 295 km. The K2K (KEK to Kamioka) experiment [5], in many ways the predecessor of T2K, had a baseline of 250 km. MINOS [6] and NOνA [7], which are competing experiments to T2K, will have 735 km and 810 km beamlines respectively, using the same neutrino beam. These two experiments are capable of investigating the same oscillations as T2K with a longer beamline because the neutrino beam is also of higher energy, a relationship that will be explained shortly.

Modern long baseline neutrino experiments tend to have three major sections: the neutrino source, a far detector and a near detector suite. The same is true for T2K; the source is a high power (0.75 MW) beam of muon neutrinos, produced in the J-PARC facility in Tokai, and the far detector is Super-Kamiokande (Super-K), a 50 kt water Čerenkov detector under Mt. Ikenoyama, near Kamioka village.

The near detector suite is situated 280 m from the start of the beam, and includes a range of detectors, which will be installed in late 2009. The work detailed in this thesis concentrates mostly on one sub-detector, a set of sampling electromagnetic calorimeters, specifically looking at the task of reconstructing the particles which will pass through them.

Full technical details of the experiment will be given in chapter 2. Chapter 3 will explain the software used, especially that for the reconstruction, and then chapter 4 will demonstrate the efficiencies that the software hopes to achieve, using photons and muons as examples of particles important to the measurements that the near detectors will undertake.

As the T2K experiment will not see first beam until May 2009, these efficiency studies are based on Monte Carlo simulations of the detectors. To provide a more conclusive proof of the reconstruction's success, data from another neutrino experiment, the SciBar Booster Neutrino Experiment (SciBooNE), were used as a test.

The SciBooNE experiment was based at the Fermi National Accelerator Laboratory (Fermilab) in Illinois, and used an existing beam and detectors from past neutrino

experiments. The data collected are being used to measure neutrino interaction cross-sections, which will also be of use to the T2K experiment.

Chapter 5 details the SciBooNE set up, explaining the similarities in detector design between T2K and SciBooNE, which make the analysis of SciBooNE data using T2K techniques a valid test. The results of that analysis are shown in chapter 6.

1.1 The Standard Model of Particle Physics

Before progressing to the physics of the T2K experiment, it is important to introduce the theory of particle physics used today, the standard model (SM). It is known that the original standard model was not a complete view of the universe; it did not account for gravity and the original state of the theory was incompatible with the discovery of neutrino oscillations.

This has been corrected by the addition of neutrino masses; however the correction required a further Higgs term, which has not yet been confirmed. Still, the corrected model is sufficient to explain the work of this thesis.

The fundamental particles within the SM are separated into two categories, fermions and bosons. Fermions are spin half particles, which obey Fermi-Dirac statistics, and they account for the matter that is observed in the universe. In contrast, the bosons have integer spin and act as force carriers for the strong and electroweak forces.

The known particles of the SM can be seen in figure 1.1, including the mass, charge and spin of each particle. For each of the 12 fermion particles, there is also an antiparticle, identical in all aspects except electric charge, which is of opposite polarity. The 12 particles can be further subdivided into leptons and quarks.

The six leptons are three charged particles, the electron, muon and tau, and the three corresponding neutrinos, ν_e, ν_μ and ν_τ. Studying the properties of these neutrinos is the objective of experiments such as T2K, and they will be covered in section 1.3.2.

The six quarks are massive particles, of which the lightest and most stable combine to form baryons such as the protons and neutrons. It is predominantly through the

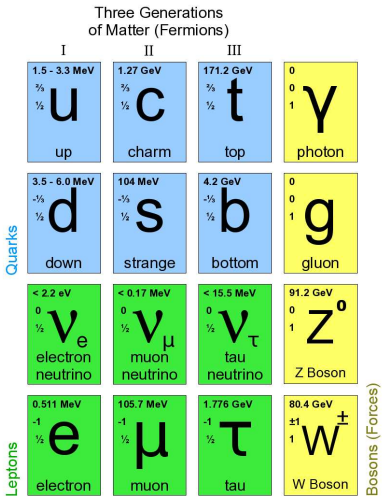

Figure 1.1: The known particles of the standard model, separated into quarks, leptons and force carriers [8]. For each particle, the mass, electric charge and spin are shown in the top left corner. Each of the fermions has a corresponding antiparticle, identical except for a reversed charge.

interactions of neutrinos with the protons and neutrons of the nuclei in the target mass that T2K is able to examine the neutrino's properties.

The four known force carriers are split between three forces: strong, electromagnetic and weak. The strong force is mediated by gluons, which interact with any particle with colour charge, namely quarks and other gluons. The strong force holds quarks together in particles such a baryons and mesons. As the strong force does not diminish with distance, quarks are never seen individually, but only within colour neutral particles such as mesons or baryons.

The second force carrier is the photon, which is associated with the electromagnetic force, and will interact with any charged particle. Due to its zero mass and zero charge, the photon is the only boson to travel large distances, a situation which makes it an observable particle in the T2K and SciBooNE detectors, the vital importance of which will be explained in chapter 2.

1.1.1 The Weak Interaction

The final force is the weak force, so called because its typical field strength is only 10^{-11} that of the electromagnetic force and 10^{-13} of the strong force. Despite this,

the weak interaction is incredibly important, as it is responsible for all flavour changing interactions and it is the only force to violate charge parity (CP) symmetry. In context, CP violation is one of the three Sakharov conditions [9] required to produce the matter/antimatter imbalance which allowed the universe to form stable matter.

The weak force carriers are $W^{\pm}$ and Z^0, the only known gauge bosons to have mass, and they only interact with quarks or left-handed leptons (i.e. leptons whose spin is pointed in the opposite direction to their motion). This makes it the only force to interact with neutrinos (other than gravity, which is negligibly small), giving the neutrino a very small interaction cross-section.

The neutrino interaction generator used by T2K, NEUT [10, 11], predicts that a 1 GeV neutrino will have a total cross-section of 1.2×10^{-38} cm^2. As an example, the interaction length for high energy electrons in Pb is 0.56 cm, but a neutrino would have a mean free path of more than a light year.

The Super-K detector, which contains 50 kt of water, sees only a handful of atmospheric neutrino events per day. When the J-PARC beam has reached its design intensity, Super-K expects to see 1000 beam events each year. In contrast, the off-axis near detector will see 64 neutrino interactions per beam spill; although many of these will be in the magnet and of no use.

1.2 Neutrino Interactions

One of the difficulties of neutrino physics is that the neutrino only interacts through the weak force; it can never be observed directly in a neutrino detector. Instead, its existence, energy and momentum must be inferred from the particles which leave the interaction. As there are two types of force carriers for the weak interaction, there are two types of neutrino interaction.

1.2.1 Charged Current

The main measurements made by T2K will be through one form of the weak interaction, those involving a $W^{\pm}$ boson called charged current (CC) interactions. The

neutrino is converted in to a charged lepton of the same flavour (this is a simplification, and will be explained in section 1.3.2). Observing and identifying this charged lepton is the only way to determine the flavour of the original neutrino.

Charged current interactions are generally identified as one of three types. The fractional cross-sections for the three types are dependent on energy, as can be seen in figure 1.2(a). The other plots in figure 1.2 show the general forms of the three interaction types.

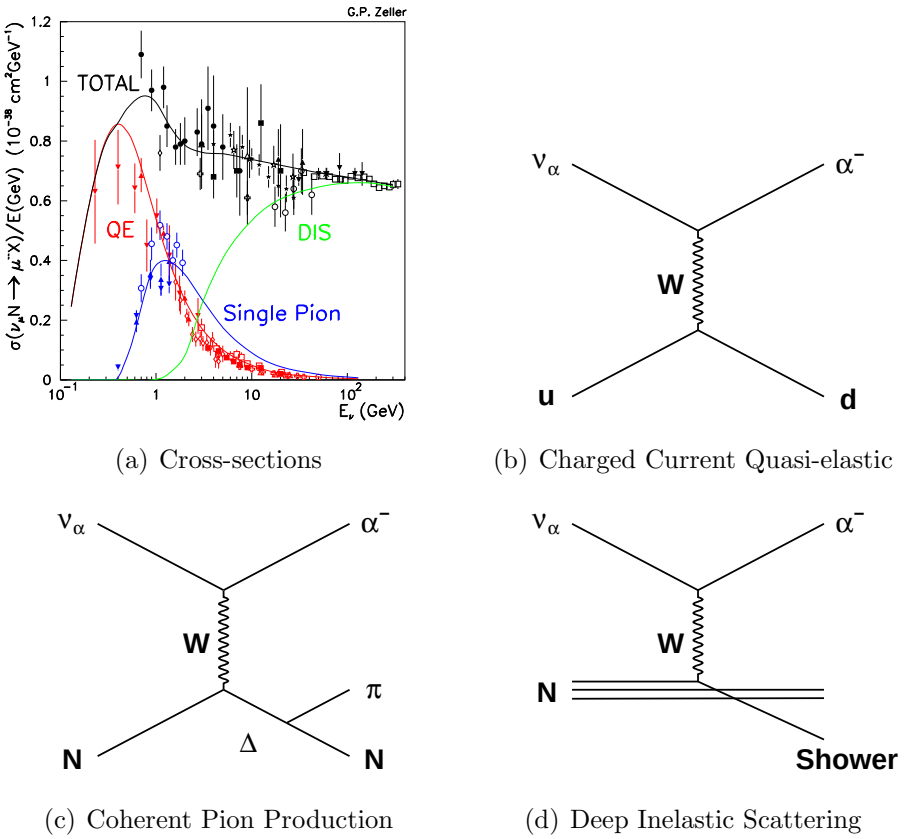

(a) Cross-sections

(b) Charged Current Quasi-elastic

(c) Coherent Pion Production

(d) Deep Inelastic Scattering

Figure 1.2: Plot (a) shows the total charged current neutrino cross-section, varying between 0.1 and 100 GeV, and was kindly provided by G.P. Zeller. (b), (c) and (d) show the categories of neutrino interactions.

The first interactions to be observed are charged current quasi-elastic (CCQE), in which the momentum transfer, Q^2, of the W boson is insufficient to break up the target nucleon. The interaction process is $\nu_l + n \rightarrow l^- + p$, where l is either e or μ, as there is insufficient energy to produce a τ. This is the channel that T2K intends

to use to measure the fluxes of muon and electron neutrinos. The direction of the neutrino beam and the reconstruction of the charged lepton's energy and direction are all that is required to reconstruct the energy of the incident neutrino. This process is dominant up to 1.1 GeV.

Above 10 GeV, the majority of interactions are categorised as deep inelastic scattering (DIS); the neutrino interacts directly with the quark structure of a nucleon, instead of the nucleon as a whole. As Q^2 is large, sufficient energy is passed to the nucleon for it to break apart, forming a hadronic shower. However, DIS will be rare in T2K, due to the large neutrino energy required.

The cross-over region between the two categories is covered by resonant pion production. The W boson transfers enough energy to convert the nucleon into an excited resonant baryon state. The lowest mass such baryons are the $\Delta(1232)$ resonances, with isospin of 3/2 and strangeness of zero. These will decay to a nucleon and a pion, for example

$$\Delta^{++} \rightarrow p + \pi^+$$

$$\Delta^{0} \rightarrow n + \pi^0$$

or

$$\Delta^{-} \rightarrow n + \pi^-$$

and the final interaction will be either $\nu_\mu + N \rightarrow \mu + N + \pi$ for CC interactions or $\nu_\mu + N \rightarrow \nu_\mu + N + \pi$ for NC. Higher energy resonances can produce more pions, but at T2K's energy single pion production is most common.

1.2.2 Neutral Current

Interactions mediated by the Z^0 boson are called neutral current (NC), because there is no flow of charge. As can be seen in figure 1.3, only momentum and energy are transferred in the interaction. For lower transfers, the target nucleon remains unchanged, and may or may not leave the target nucleus. At higher transfers, sufficient energy may be passed to create other particles, generally pions.

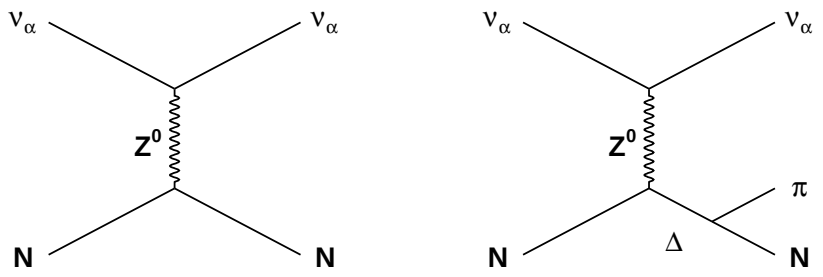

(a) Neutral Current Low Energy (b) Neutral Current Pion Production

Figure 1.3: Neutral current neutrino interactions, mediated by the Z^0 boson. Both interactions are independent of neutrino flavour.

As no charge is transferred in the NC interaction, the neutrino is unchanged, except for a transfer of energy and momentum. This makes it impossible to determine the flavour of the neutrino, and these interactions are not used as part of the oscillation search. However, the other particles produced in a NC interaction will still be detected in the detectors.

Neutral Current π^0 Production

The largest NC background interaction is the neutral current single π^0 (NCπ0) interaction. In this interaction, only a single new particle is produced, a π^0 meson. The π^0 decays very quickly (mean life time = $(8.4 \pm 0.6) \times 10^{-17}$ s), and 99% of the time it decays to two photons [8].

The photons are produced back to back in the π^0 rest frame, but Lorentz boosted in the lab frame. Depending on the angle between the photons and the boost, they can come out of the decay with a significant variation in energy. In a Čerenkov detector such as Super-K (details of which follow in chapter 2), many of the possible outcomes are indistinguishable from a CCQE ν_e interaction.

The NCπ0 cross-section is not well known in the T2K energy region. Therefore, determining the rate of NCπ0 interactions in Super-K is an important part of T2K's analyses; the background should be measured to 10% in the desired energy region [12]. Much of the work described in this thesis was towards that goal.

1.3 A History of Neutrino Physics

The neutrino was first proposed by Wolfgang Pauli in 1930 [13], as a solution to the problems of beta decay, specifically that energy, momentum and angular momentum were not being conserved in the observed interaction. The electron left the nucleus not with a definite energy and momentum, expected from a two body decay, but with a distribution. This could be explained by an invisible particle of half-integer spin, carrying off energy and momentum undetected.

The particle would have to be without charge and have a very small cross-section to escape detection. It would also need a very small, or possibly zero, mass to explain the electron's energy distribution. Pauli originally proposed this particle be called the neutron, however this name was taken two years later by James Chadwick, before the neutrino was observed experimentally, so the name neutrino was suggested by Enrico Fermi, coming from the Italian for "little neutral one".

The first detection of the neutrino was achieved by the Cowan and Reines neutrino experiment [14], which detected antineutrinos from a nuclear reactor via induced beta decay

$$\bar{\nu}_e + p \rightarrow n + e^+$$

an interaction which produced a neutron and a positron, both detectable particles. In the same year, Ray Davis attempted to detect neutrinos from a reactor using capture on a chlorine atom

$$\bar{\nu}_e + {}^{37}\mathrm{Cl}(n) \rightarrow {}^{37}\mathrm{Ar}(p) + e^-$$

but no signal was observed. This failure provided evidence for neutrinos and antineutrinos being different particles, in which case the above interaction is forbidden, as it violates lepton number. The possibility of neutrinos being Majorana particles instead of Dirac is immensely interesting [15], but beyond the scope of this introduction.

Following the discovery of the electron neutrino was the discovery of the muon neutrino in 1962 [1], using the Alternating Gradient Synchrotron at Brookhaven, the

first example of the neutrino beam that has become a staple of neutrino physics. The discovery of the tau lepton at SLAC in 1975 immediately suggested the existence of a third neutrino type, the first direct interactions of which were detected at Fermilab, by the DONUT collaboration in 2000 [16], although missing energy and momentum in tau decays had been observed before, analogous to the original beta decay observations.

1.3.1 The Solar Neutrino Problem

The solar neutrino problem is one of the most interesting stages in neutrino physics. In the 1960s, the neutrino was believed to be well enough understood to use it as a tool for studying the standard solar model (SSM), from which the neutrino flux is an observed quantity. The model predicted a neutrino rate between 6.6 and 8.1 Solar Neutrino Units (1 SNU = one interaction per 10^{36} target atoms per second). However, when Ray Davis's Homestake experiment attempted to measure the flux, the neutrino rate detected was 2.56 ± 0.16(stat) ± 0.16(syst) SNU, only one-third the predicted rate [17]. A number of different experiments followed, trying to confirm or disprove the deficit.

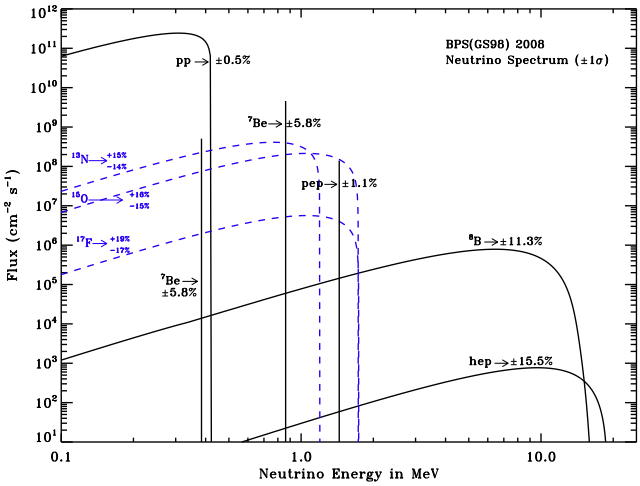

Figure 1.4: The flux of neutrinos arriving at the earth, as predicted by the Standard Solar Model, as a function of energy and the interaction which produced them. Reproduced with permission from Prof. Serenelli [18].

The deficit was first confirmed by the Kamioka Nucleon Decay Experiment, a 3 kt water Čerenkov detector which was upgraded to search for solar neutrinos. Čerenkov detectors (which are further explained in section 2.2) can only detect neutrinos from the beta decay of boron-8, the highest energy neutrinos to come from the SSM, but are capable of determining the direction of the inbound neutrino. This was coupled with the position of the sun to show an excess of neutrino events from the sun, the first clear signal of solar neutrinos [19].

The measured flux was $2.35 \pm 0.02(\text{stat}) \pm 0.08(\text{syst}) \times 10^6\,\text{cm}^{-2}\text{s}^{-1}$, approximately half of the SSM prediction for ^{8}B neutrinos:

$$\Phi_{\text{SSM}}(\nu_e) = 5.05^{+1.01}_{-0.81} \times 10^6\,\text{cm}^{-2}\text{s}^{-1}$$

Several models were suggested to explain the deficit, based on neutrino decay or oscillations, but it was results from the SNO collaboration in 2002 which showed "direct evidence for neutrino flavour transformation" [20]. Whilst the SNO detector could also only detect ^{8}B neutrinos, it could do so through three channels:

$$\begin{aligned}
\nu_e + d &\rightarrow e^- + p + p \\
\nu_x + e^- &\rightarrow \nu_x + e^- \\
\nu_x + d &\rightarrow \nu_x + n + p
\end{aligned}$$

charged current (CC), elastic scattering (ES) and neutral current (NC) interactions respectively. The rates measured for the three interactions varied significantly:

$$\begin{aligned}
\Phi^{\text{CC}}_{\text{SNO}}(\nu_e) &= 1.76 \pm 0.06(\text{stat}) \pm\ 0.09(\text{syst}) \times 10^6\,\text{cm}^{-2}\text{s}^{-1} \\
\Phi^{\text{ES}}_{\text{SNO}}(\nu_x) &= 2.39 \pm 0.24(\text{stat}) \pm\ 0.12(\text{syst}) \times 10^6\,\text{cm}^{-2}\text{s}^{-1} \\
\Phi^{\text{NC}}_{\text{SNO}}(\nu_x) &= 5.09 \pm 0.44(\text{stat}) \pm\ 0.46(\text{syst}) \times 10^6\,\text{cm}^{-2}\text{s}^{-1}
\end{aligned}$$

These results can be explained by neutrino oscillations. As the NC interaction is independent of the neutrino flavour, any ν_e that oscillated to ν_μ or ν_τ still contributed to the observed rate, hence good agreement between the NC flux and the SSM prediction for ^{8}B neutrinos.

The CC and ES measurements both agree with neutrino oscillations; the CC is only sensitive to the ν_e and the ES interaction has different cross-sections for the

three neutrinos; the ν_e cross-section is 6.5 times larger than the ν_μ or ν_τ. Whilst no one measurement was enough to prove neutrino oscillations, the non-ν_e component was $\Phi_{\mu\tau} = 3.41^{+0.45}_{-0.45}(\text{stat})^{+0.48}_{-0.43}(\text{syst}) \times 10^6\ \text{cm}^{-2}\text{s}^{-1}$. This was 5.3σ above zero, and combined with all previous results was sufficient to convince most physicists.

1.3.2 Neutrino Oscillations

Neutrino oscillation is a quantum mechanical phenomenon, based on the premise that if neutrinos have mass, the flavour eigenstates, $|\nu_e\rangle$, $|\nu_\mu\rangle$ and $|\nu_\tau\rangle$, and the mass eigenstates, $|\nu_1\rangle$, $|\nu_2\rangle$ and $|\nu_3\rangle$, are not necessarily the same. Specifically, a neutrino would be produced in a flavour-specific interaction, where the flavour is defined by the accompanying lepton in the interaction, but would propagate as a mass eigenstate.

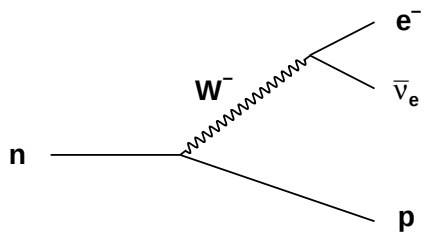

Figure 1.5: Beta decay.

For example, in beta decay, the antineutrino produced is electron flavour because of the electron simultaneously produced (see figure 1.5). For the T2K experiment, it is generally assumed that there are three neutrino flavours[1]. In this assumption, the particle which travels from the source to the detector is defined by one of the mass eigenstates, which are related to the flavour eigenstates by the 3×3 leptonic mixing matrix, U, sometimes referred to as the Maki-Nakagawa-Sakata matrix or the Pontecorvo-Maki-Nakagawa-Sakata matrix, after four scientists who proposed

[1]The LSND experiment produced results which suggested a fourth, sterile neutrino, but follow-up measurements by MiniBooNE were unable to confirm this result.

mixing and oscillation in neutrinos [21, 22]. The matrix is simply

$$U = \begin{bmatrix} U_{e1} & U_{e2} & U_{e3} \\ U_{\mu 1} & U_{\mu 2} & U_{\mu 3} \\ U_{\tau 1} & U_{\tau 2} & U_{\tau 3} \end{bmatrix}$$

which can be rewritten in terms of the three mixing angles, θ_{ij}, and a complex phase, δ. (The abbreviations c_{ij} and s_{ij} are used for $\cos\theta_{ij}$ and $\sin\theta_{ij}$.)

$$U = \begin{bmatrix} 1 & 0 & 0 \\ 0 & c_{23} & s_{23} \\ 0 & -s_{23} & c_{23} \end{bmatrix} \times \begin{bmatrix} c_{13} & 0 & s_{13}e^{-i\delta} \\ 0 & 1 & 0 \\ -s_{13}e^{i\delta} & 0 & c_{13} \end{bmatrix} \times \begin{bmatrix} c_{12} & s_{12} & 0 \\ -s_{12} & c_{12} & 0 \\ 0 & 0 & 1 \end{bmatrix} \tag{1.1}$$

In this formalism, the leftmost matrix relates to $\nu_\mu \rightarrow \nu_\tau$ mixing, the central to $\nu_e \rightarrow \nu_\tau$ mixing and the right to $\nu_e \rightarrow \nu_\mu$ mixing.

The amplitude for the oscillation $\nu_\alpha \rightarrow \nu_\beta$ is a coherent sum over the contributions from the three mass eigenstates. The contribution from an individual mass state is determined by three parts, the amplitude for a neutrino of type α to produce a mass state i, the propagation of that mass state and the amplitude of ν_i to produce ν_β.

$$\mathrm{Amp}(\nu_\alpha \rightarrow \nu_\beta) = \sum_i U^*_{\alpha i} \times \mathrm{Prop}(\nu_i) \times U_{\beta i}$$

The propagation term is derived from quantum mechanics as being $\mathrm{Prop}(\nu_i) = e^{-im_i\tau_i}$, where m_i is the mass, τ_i is the proper time observed by the neutrino as it propagates and natural units are being used ($c = h = 1$). Past oscillation experiments have often used a two neutrino approximation. The approximation can be used because two of the oscillation parameters that affect propagation, Δm^2_{23} and Δm^2_{13} (which will be explained shortly), are very similar, so that over certain distance and energy ranges two of the three neutrino mass eigenstates are degenerate. This approximation is not valid for T2K, but it can be useful for introducing oscillations.

In this approximation, the two neutrino eigenstates after time t and distance $\bar{x}$ are given by:

$$\begin{bmatrix} |\nu_\alpha(\bar{x},t)\rangle \\ |\nu_\beta(\bar{x},t)\rangle \end{bmatrix} = \begin{bmatrix} \cos\theta & \sin\theta \\ -\sin\theta & \cos\theta \end{bmatrix} \begin{bmatrix} e^{-im_1 t} & 0 \\ 0 & e^{-im_2 t} \end{bmatrix} \begin{bmatrix} \cos\theta & -\sin\theta \\ \sin\theta & \cos\theta \end{bmatrix} \begin{bmatrix} |\nu_\alpha(0)\rangle \\ |\nu_\beta(0)\rangle \end{bmatrix}$$

If the initial state is pure ν_α, then $|\nu_\alpha\rangle = 1$ and $|\nu_\beta\rangle = 0$, and the probability of oscillation is:

$$P(\nu_\alpha \to \nu_\beta) \equiv ||\nu_\beta(\bar{x}, t)\rangle|^2 = \sin^2(2\theta)\sin^2(m_2\tau_2 - m_1\tau_1)$$

Lorentz invariance gives the relationship $m_i\tau_i = E_i t - p_i L$, where E_i and p_i are the energy and momentum, L is the distance travelled and t is the time taken, all within the lab frame. The time can be determined from the distance, L and mean velocity, $\bar{v}$, of the ν_1 and ν_2 components, so that $t = L/\bar{v}$ and

$$\bar{v} \equiv \frac{p_1 + p_2}{E_1 + E_2}$$

Therefore, the argument of the sine oscillation term becomes

$$\begin{aligned}
(m_2\tau_2 - m_1\tau_1) &= (E_2 t - p_2 L) - (E_1 t - p_1 L) \\
&= (p_1 - p_2)L - (E_1 - E_2)t \\
&= \frac{p_1^2 - p_2^2}{p_1 + p_2}L - \frac{E_1^2 - E_2^2}{p_1 + p_2}L \\
&= (m_2^2 - m_1^2)\frac{L}{p_1 + p_2} \\
&\cong \Delta m_{21}^2 \frac{L}{2E}
\end{aligned}$$

where the approximation $p_1 = p_2 = E$ has been used for the highly relativistic neutrinos. Δm_{ij}^2 is the difference between the two squared masses, m_i^2 and m_j^2. The probability for oscillations becomes:

$$P(\nu_\alpha \to \nu_\beta) = \sin^2(2\theta)\sin^2\left(\Delta m_{21}^2 \frac{L}{2E}\right)$$

This equation can be expanded and generalised for the three neutrino case, and is then given by:

$$\begin{aligned}
P(\nu_\alpha \to \nu_\beta) &= |\mathrm{Amp}(\nu_\alpha \to \nu_\beta)|^2 \\
&= \delta_{\alpha\beta} - 4\sum_{i>j} \mathrm{Re}(U_{\alpha i}^* U_{\beta i} U_{\alpha j} U_{\beta j}^*)\sin^2(\Delta m_{ij}^2 L/4E) \\
&\quad + 2\sum_{i>j} \mathrm{Im}(U_{\alpha i}^* U_{\beta i} U_{\alpha j} U_{\beta j}^*)\sin(\Delta m_{ij}^2 L/2E)
\end{aligned}$$

Oscillations are now defined by seven parameters, three mixing angles and three mass differences which are shown with the current best values or limits [8, 23, 24] and an unknown CP-violating phase, δ:

$$\begin{aligned}
\theta_{13} &< 3.2^\circ \\
\theta_{12} &= 33.9^{\circ\,+2.4^\circ}_{\quad -2.2^\circ} \\
\theta_{23} &= 45 \pm 7^\circ \\
\Delta m^2_{21} &= 8.0^{+0.6}_{-0.4} \times 10^{-5}\text{eV}^2 \\
\Delta m^2_{31} &\approx \Delta m^2_{32} \\
\Delta m^2_{32} &= 2.4^{+0.6}_{-0.5} \times 10^{-3}\text{eV}^2
\end{aligned}$$

When the units of $\hbar$ and c are reintroduced into the equation, then the $\Delta m^2_{ij} L/2E$ term becomes a dimensionless $1.27\Delta m^2_{ij}(\text{eV}^2)L(\text{km})/E(\text{GeV})$.

The final correction required before the oscillation probability is complete is due to the matter effect. When neutrinos travel through matter, there is a continuous possibility of coherent forward scattering from the electrons, neutrons and protons. For the most part this scattering is mediated by the Z boson, and thus the effect is equal for all three neutrino flavours and has no bearing on oscillations. However, there is one process which involves the W boson, coherent forward $\nu_e e \rightarrow \nu_e e$ scattering (as seen in figure 1.6).

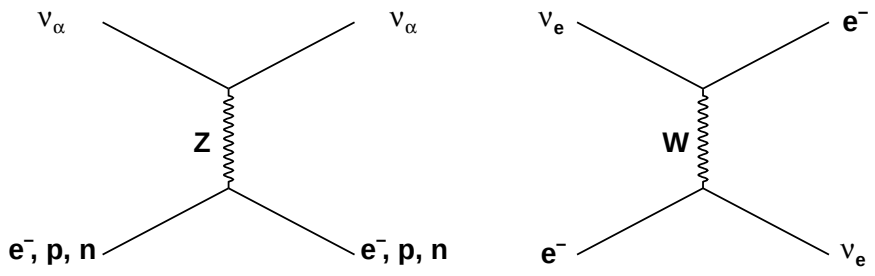

(a) Neutral Current (b) Charged Current

Figure 1.6: Coherent forward scattering matter interactions, mediated by Z or W bosons.

This interaction changes the oscillation, such that the apparent values for Δm^2 and θ measured in the presence of significant matter effects deviate from the true values:

$$\Delta m^2_M = \Delta m^2 \sqrt{\sin^2 2\theta + (\cos 2\theta - x_\nu)^2}$$

and

$$\sin^2 2\theta_M = \frac{\sin^2 2\theta}{\sin^2 2\theta + (\cos 2\theta - x_\nu)^2}$$

where Δm^2_M and θ_M are the effective values of Δm^2 and θ, and

$$x_\nu \equiv \frac{2\sqrt{2} G_F N_e E}{\Delta m^2}$$

x_ν is a measure of the importance of matter effects; it is linear in both energy, E, and the electron density of the matter, N_e. G_F is the Fermi coupling constant, which is a measure of the amplitude of the charged current interaction, figure 1.6(b). As $N_e \to 0$, Δm^2_M and θ_M revert to the vacuum values, Δm^2 and θ.

With this change, the full probability for a $\nu_\mu \to \nu_e$ oscillation can be written out. The equation has been approximated slightly, using the knowledge that $\alpha \equiv \Delta m^2_{21}/\Delta m^2_{31} \sim 1/30$ and $\sin^2 2\theta_{13} < 0.2$, which allows higher order terms to be ignored.

$$P(\nu_\mu \to \nu_e) \cong \sin^2 2\theta_{13} T_1 - \alpha \sin 2\theta_{13} T_2 + \alpha \sin 2\theta_{13} T_3 + \alpha^2 T_4 \tag{1.2}$$

where

$$T_1 = \sin^2 \theta_{23} \frac{\sin^2[(1-x_\nu)\Delta]}{(1-x_\nu)^2} \tag{1.3}$$

$$T_2 = \sin\delta \sin 2\theta_{12} \sin 2\theta_{23} \sin\Delta \frac{\sin(x_\nu\Delta)}{x_\nu} \frac{\sin[(1-x_\nu)\Delta]}{(1-x_\nu)} \tag{1.4}$$

$$T_3 = \cos\delta \sin 2\theta_{12} \sin 2\theta_{23} \cos\Delta \frac{\sin(x_\nu\Delta)}{x_\nu} \frac{\sin[(1-x_\nu)\Delta]}{(1-x_\nu)} \tag{1.5}$$

and

$$T_4 = \cos^2 \theta_{23} \sin^2 2\theta_{12} \frac{\sin^2[x_\nu\Delta]}{x_\nu^2} \tag{1.6}$$

In these equations, $\Delta \equiv \Delta m^2_{31} L/4E$ is the kinematical phase of the oscillation, terms T_1 and T_4 correspond to the oscillations for splittings Δm^2_{31} and Δm^2_{21} respectively and T_2 and T_2 are CP-violating and CP-conserving interference terms.

1.4 The T2K Oscillation Measurements

In the previous section, the seven parameters of neutrino oscillations were introduced; three mass splittings, three mixing angles and a CP violating phase, δ. The

mass splittings are known to reasonable accuracy, and so are two of the mixing angles. The main goal of the T2K experiment is therefore to measure the third mixing angle, θ_{13}. Equation 1.1 shows that the final parameter δ is only seen in conjunction with $\sin\theta_{13}$, i.e. CP violation will only be possible if $\theta_{13} \neq 0$. Therefore, only if T2K measures a non-zero θ_{13} can a later phase of the experiment attempt to measure δ.

To measure θ_{13}, T2K will make an electron neutrino appearance measurement. That is to say, Super-K will search for ν_e in the beam from Tokai, a beam which is predominantly ν_μ. The oscillation probability, $P(\nu_\mu \rightarrow \nu_e)$, can be extracted from the ratio of ν_e to ν_μ events at Super-K, and CCQE interactions will be selected, so that the neutrino energy can be reconstructed. However several corrections must be made, corrections which will require their own measurements.

The T2K beam will not be purely ν_μ when it leaves Tokai; roughly 1% of the beam will be ν_e. This is an unavoidable part of the beam production, and will be explained in section 2.1. The near detector suite will measure this initial contamination, so that it can be accounted for in the oscillation analysis.

Also, not all Super-K events that are reconstructed as ν_e CCQE interactions will be so; the NCπ0 interaction has already been mentioned as the major background. The near detectors (which will see a much higher event rate than Super-K) will be used to accurately measure (to 10%) the NCπ0 cross-section on water. Along with the neutrino flux at Super-K, this will provide an estimation of the number of background events, which can be subtracted from the number of ν_e CCQE signal-like events.

The final measurement required comes from the physics of the oscillations. Equations 1.2 through 1.6 show that a measurement of θ_{13} will always depend on the accuracy to which θ_{23} and Δm^2_{23} are known. To improve the sensitivity to θ_{13}, T2K will make a separate measurement of θ_{23} and Δm^2_{23}, through the ν_μ disappearance channel. The flux of ν_μ at Super-K, predicted by flux measurements at the near detector, will be compared to the measured flux, which will give $P(\nu_\mu \rightarrow \nu_\mu)$, from which θ_{23} can be determined.

1.4.1 The Near Detector Measurements

Full details of the T2K experimental setup will be given in chapter 2, but a brief overview of the near detector is included here, to explain how the near detector will make the measurements mentioned above, and how the work described later in this thesis relates to those measurements.

The ND280 is the main near detector suite, 280 m from the target and 2.5° off-axis from the beam. ND280 is separated into two main regions, both of which are contained within a 0.2 T magnet.

The downstream region is called the 'tracker', as it contains detectors designed to provide good tracking and reconstruction efficiencies for charged particles. The tracker's main responsibility is the CCQE measurements. By measuring momentum and direction of the lepton and proton produced by a CCQE interaction, the flavour, energy and direction of the neutrino can be determined. This determines the flux of neutrinos created at J-PARC and travelling to Super-K.

To make this measurement, two detector regions with fine granularity (fine grain detectors or FGDs) act as an instrumented target mass. The fine granularity means that many protons will leave a long enough track for a reconstruction, but the FGDs are not designed to stop the charged lepton. These will leave the FGD and enter a time projection chamber (TPC), a detector design with excellent spatial resolution and little mass to cause scattering. The curvature of the particles will be measured, which gives the momentum, and the direction.

The final requirement is for particle identification, as this allows a conversion from momentum to energy. To this end, the FGDs and TPCs are surrounded on seven sides by electromagnetic calorimeters (ECals). The calorimeters will allow for particle identification, as well as energy reconstruction of some particles and direction reconstruction. The first stage of the particle reconstruction, the clustering, is the central work of this thesis; the methods used will be described in section 3.4.5 and then the effectiveness of these methods will be investigated in chapter 4.

The upstream region of the ND280 is the π^0 detector or P0D. The P0D is an active target region, just like the FGDs, but is larger and includes layers of absorber (either brass or lead). The design aim is that particles will not leave the P0D, especially not the photons produced by π^0 decay, allowing for a contained measurement of the NCπ0 interaction.

However, the tracker region will also be attempting a measurement of the NCπ0 cross-section. The intention is for this measurement to provide a useful cross-check of the P0D's measurement, just as the P0D will make a measurement of CCQE interaction rates. The NCπ0 measurement in the tracker region will rely on the ECals to reconstruct the energy and direction of photons from the π^0 decay. Therefore, the methods explained in section 3.4.5 have been optimised for the reconstruction of muons and electromagnetic particles such as electrons and photons.

The results in chapter 4 show a clear energy dependency for reconstruction; many of the lower energy particles do not leave a sufficient deposit to be clustered (without opening the reconstruction up to noise backgrounds), but approximately 90% of muons above 100 MeV are correctly reconstructed. For photons, this drops to 75% in the 100 – 250 MeV region, with the main loss in efficiency coming from showers being split into multiple reconstructed clusters.

1.5 Using SciBooNE Data to Test the ECal Reconstruction

As the T2K experiment will not start running until April 2009, the investigation described in chapter 4 is completely Monte Carlo-based. Particles are simulated and reconstructed within the software, but there is no confirmation that the simulation will correctly match the real world scenario. To address this issue, data from another neutrino experiment, the SciBooNE experiment, have been used.

SciBooNE's experimental goals and setup are explained in chapter 5, introducing the SciBar detector and Booster Neutrino Beam. As the SciBar has a similar design

concept to parts of the ND280, it is shown that the ECal reconstruction methods from T2K can be applied to the SciBooNE data.

Chapter 6 analyses the effectiveness of these methods on the SciBar data, and the results prove that, for charged particles, they have an efficiency comparable to SciBooNE's own methods. A full π^0 reconstruction is not attempted, but the comparison of SciBooNE's data and MC shows clear evidence that photon signals are being reconstructed.

Chapter 2

The T2K Experiment

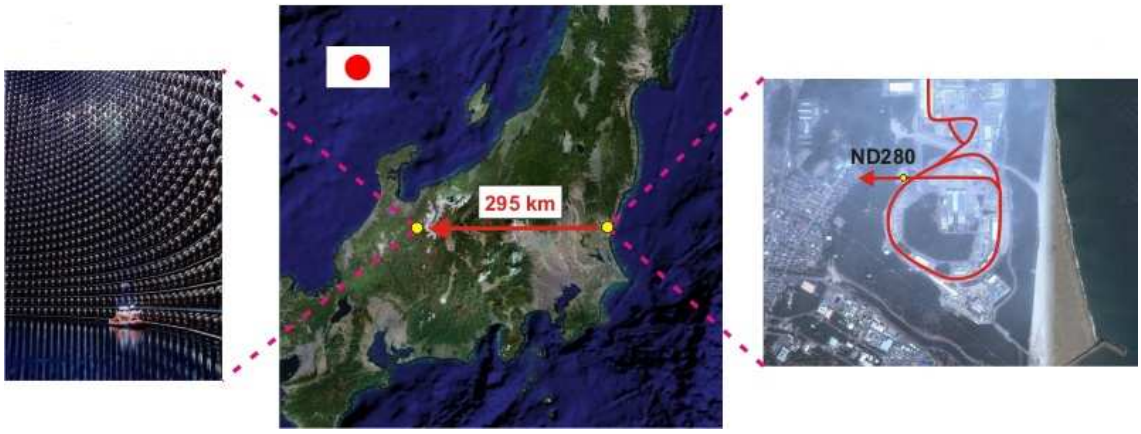

Figure 2.1: A map showing the J-PARC facility (right) and the Super-Kamiokande detector (left).

The two geographical locations of T2K are shown in figure 2.1; of the experiment's major components, only the far detector is ready; the near detector and beam are still being constructed and commissioned. The collaboration intends to use a ν_e appearance measurement to try to determine θ_{13}. T2K will also improve the precision of Δm^2_{23} and θ_{23}, vital for the determination of θ_{13}, with a ν_μ disappearance measurement. It has not yet been shown that θ_{23} is not maximal, and this special case is of almost equal interest to the possibility of a minimal θ_{13}. However, should θ_{13} be found to be non-zero, then this introduces the possibility of a CP violating

phase δ, and a later phase of the experiment could search for δ by running in antineutrino mode.

To achieve its goals, T2K uses a similar strategy to the earlier K2K experiment [25]; to produce a beam of neutrinos, then make sampling measurements of them at both a near detector site and a far detector after oscillation has occurred. The beam and near detectors will be sited at the Japan Proton Accelerator Research Complex (J-PARC) in Tokai, on the East coast of Japan (figure 2.1).

Like K2K before it, T2K will use the Super-Kamiokande (Super-K) detector as its far detector, having the advantages of being a well understood detector with a large fiducial mass. T2K does have several improvements over the K2K model, however, and one of the major ones is the off-axis position of its detectors. As can be seen in figure 2.2, the energy flux of neutrinos produced by the J-PARC beam changes with the direction, for purely kinematic reasons, and this change can be used to T2K's advantage.

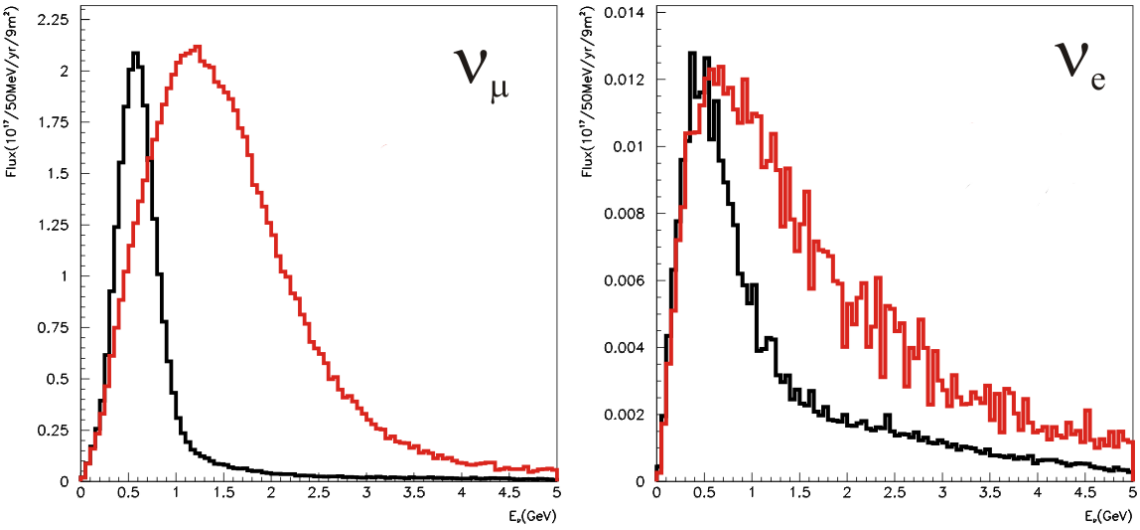

Figure 2.2: The T2K flux for ν_μ and ν_e. The red line is the on-axis flux, the black 2.5° off-axis. The units refer to the black line, and account for the apparent area of the near detector (9 m^2) and an expected 10^{21} protons on target per year. The red line has been renormalised to the same peak value; the total flux is lower for an off-axis detector position, but the peak is much narrower and higher at its centre than for the same energy on-axis.

Any neutrino experiment aims for the largest possible signal to background ratio; in an oscillation experiment this is achieved by placing the far detector at the predicted

point of maximum oscillation. At this distance (which is of course dependent on the energy), the largest proportion of ν_μ's have oscillated to ν_e's. As the baseline of the T2K experiment was set at 295 km, current measurements on the oscillation parameters suggested a neutrino energy of approximately 700 MeV, lower than the peak of the on-axis beam. At 2.5° off-axis the flux at 700 MeV is not only higher, but the peak has narrowed significantly.

Neutrinos in the high energy tail of the flux are more likely to produce background events than signal events useful to the analysis; for example, deep inelastic scattering (DIS) events with one visible lepton, but also multiple pions, which might go unobserved. The increased flux at 700 MeV will provide more events, and whilst these will be both signal and background, it will decrease the statistical error. More importantly, the thinner peak in energy means that systematic errors due to misreconstruction of the neutrino energy will be minimised, improving the quality of the measurement.

2.1 The J-PARC Facility and Neutrino Beam

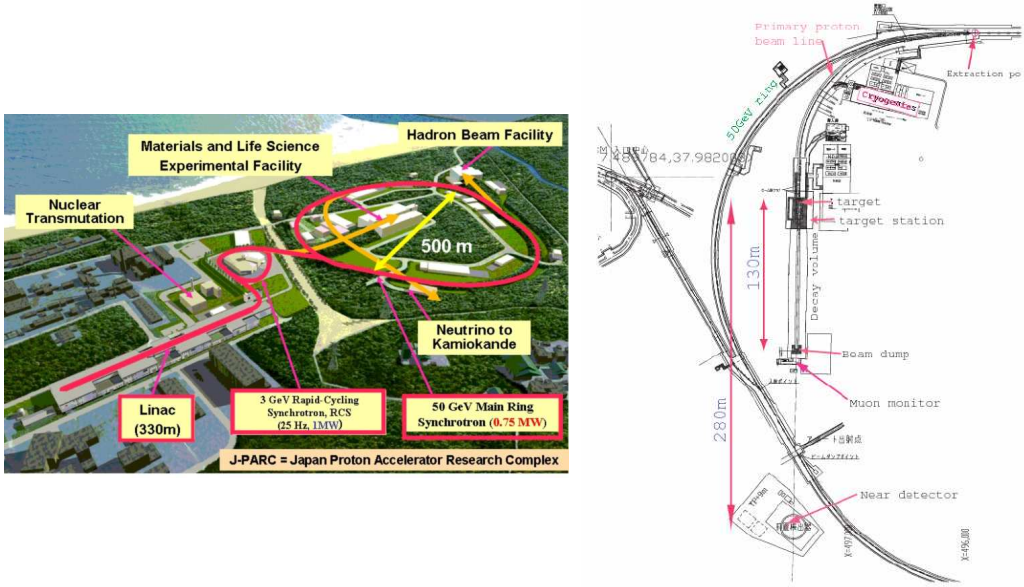

Figure 2.3: Left: Layout of the J-PARC Facility. Right: Map showing the extraction point, target, decay volume and near detector pit.

Situated on the East coast of Japan, at Tokai-mura in the Ibaraki prefecture, J-PARC provides 50 GeV protons for a range of nuclear and particle physics experiments,[1] as well as lower energy (3 GeV) protons for nuclear, particle and condensed matter physics, material sciences and structural biology. The production of these protons requires a series of accelerators [26, 27] which can be seen in figure 2.3:

Linear accelerator (Linac) which starts with negatively ionised hydrogen and accelerates it to 400 MeV at 50 Hz. The H^- then passes through the

Carbon Stripper Foil where electrons are removed from the beam [28]. The resulting proton beam is injected into the

Rapid-cycling Synchrotron (RCS) which increases the energy to 3 GeV with a repetition rate of 25 Hz, before finally entering the

Main Ring Proton Synchrotron (PS) for the final jump to 50 GeV. The protons are then fast-extracted to the T2K target, using five kicker magnets.

The protons will interact with a helium-cooled graphite target, producing a large number of pions (and a smaller kaon contamination). Only the positively charged pions will produce the ν_μ's required for T2K, so as many as possible of the negative pions should be removed. This is achieved by passing the pions through three magnetic 'horns', which will focus the positive pions, whilst simultaneously defocusing the negative pions. Each horn consists of two concentric aluminium cylinders, carrying a large electric current. The magnetic field produced inside is circular, diminishing towards the centre, and will bend any positive particles on the edges back in towards the centre, whilst bending the π^- outwards [29].

After passing through the horns, any remaining mesons will enter the decay volume. This volume is 110 m long, and the cross-section starts at 2.2 m (W) × 2.8 m (H), increasing to 3.0 m × 4.6 m at the far end, filled with inert helium gas held at 1 atm. The walls are constructed from iron plates, as a very large number of particles will

[1] These figures are the design state of J-PARC, but may not be reached for some years after first beam.

be hitting them. The particles carry a lot of energy so water cooling channels are built into the walls, and the whole volume is surrounded by 6 m of concrete.

Inside the decay pipe, any π^+ which is not stopped by the walls will decay to $\nu_\mu + \mu^+$, producing the beam of ν_μ's. As a μ^+ would subsequently decay to $\bar{\nu}_\mu + e^+ + \nu_e$ and contaminate the neutrino beam, the length of the decay volume has been tuned to maximise pion decays whilst limiting muon decays. Any muons which exit out of the back of the decay volume will rapidly lose energy to the earth, limiting the energy of the produced ν_e.

At the end of the decay volume is a beam dump, constructed of cooled graphite and copper blocks. This region absorbs the energy of any remaining pions, and ensures that this energy is not deposited into the surrounding earth. If this were to happen, the region would be highly irradiated and the local ground water would be contaminated, with potentially disastrous effects on the environment.

The large width and height of the beam pipe allows for the possibility of varying the beam direction, such that the detectors could have an off-axis angle between 2° and 3°. Also, the polarity of the current in the horns can be reversed, which would focus π^- and remove π^+. This ensures that later stages of the T2K experiment can switch between ν_μ and $\bar{\nu_\mu}$, if the physics measurements require it.

2.2 The Super-Kamiokande Detector (Super-K)

Situated under Mt. Ikenoyama in the Gifu prefecture, Japan, Super-Kamiokande is the world's largest contained water Čerenkov detector [30]. Constructed in the mid-90s, data taking commenced in April 1996, and the collaboration announced their first evidence of neutrino oscillation in 1998 [31]. The detector ran until July 2001, when it was shut down for maintenance and upgrade work. During the refilling process after this work, a single photomultiplier tube (PMT) imploded, starting a cascade which destroyed well over half the PMTs in the detector [32, 33]. The remaining PMTs and any spares were redistributed about the detector volume, totalling 47% of the original number, giving 19% surface coverage. It was run this

way until July 2005, when enough replacement PMTs had been produced for a full reconstruction. Reconstruction was completed in July 2006, and the detector is now back at full efficiency, with fibre-reinforced covers and acrylic windows around each PMT, to prevent a repeat of the accident.

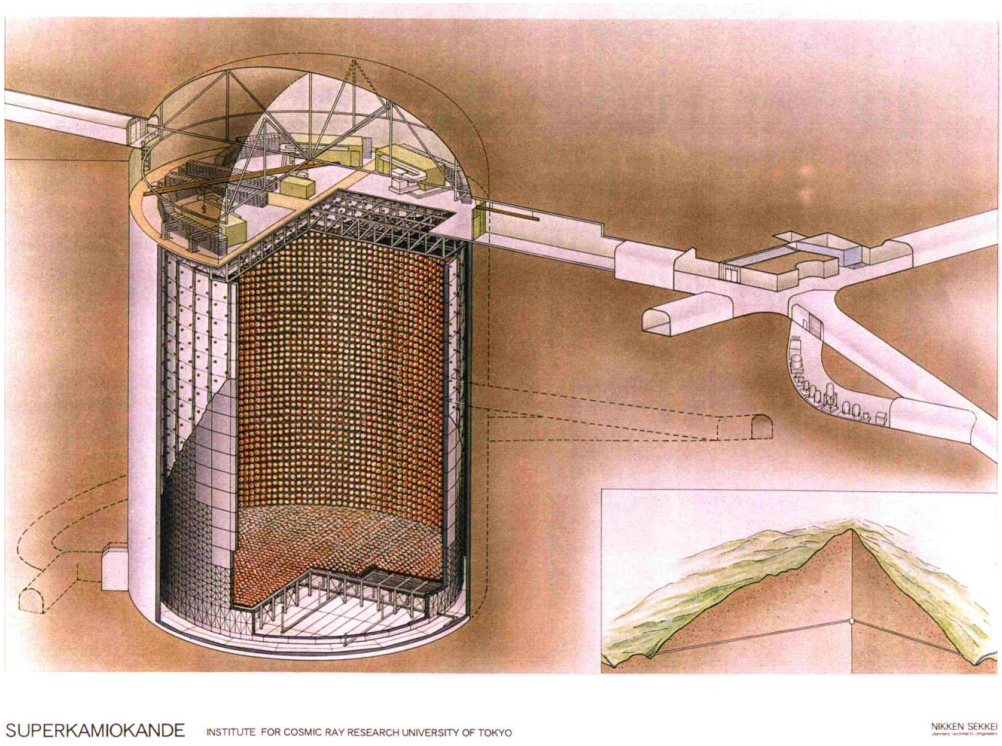

Figure 2.4: A drawing of the Super-Kamiokande detector, showing the tank, the electronics huts and water purification systems at the top of the tank, and the detector's position in Mt. Ikenoyama. ©Kamioka Observatory, ICRR (Institute for Cosmic Ray Research), The University of Tokyo.

Under 1000 m of rock (2,700 m.w.e or metre water equivalent), Super-K is shielded from all but the highest energy cosmic ray muons (1.3 TeV minimum for penetration). As seen in figure 2.4, the detector is a cylindrical, vertically orientated, stainless steel tank, 39 m in diameter and 42 m tall, holding 50 kt of water. Internally, the detector is divided into the inner detector (ID) and the outer detector (OD), by a second cylinder. The OD acts as a veto, tagging events where the initial reaction is in the surrounding rock, instead of Super-K's fiducial volume. The second cylinder is a 55 cm thick framework, again of stainless steel, which starts approximately 2 m from the outside wall and supports two arrays of PMTs, one facing inwards, the other outwards.

PMTs are very sensitive photosensors, based around a large potential difference within a vacuum tube. A photon falling on the front face of the tube will interact with the photocathode, producing an electron. The electron is accelerated towards a series of dynodes, each held at a higher voltage than the last, which causes a cascade, producing more electrons at each dynode. The cascade reaches an anode at the rear of the tube, producing a pulse of current. This design gives each PMT a very high gain of around 10^8 and a low noise rate, which allows them to detect single photon signals.

The ID is instrumented with 11,146 Hamamatsu R3600 hemispherical PMTs, with a diameter of 20 in, giving approximately 40% surface coverage, with the rest of the surface covered in a black, light tight material, to prevent light leaks from the OD and to minimise reflection. Conversely, the OD is instrumented with 1,885 Hamamatsu R1408 8 in diameter hemispherical PMTs, placed in the centre of a $60 \times 60\,\mathrm{cm}^2$ acrylic wavelength-shifting plate, which increases the light detection efficiency by 60% [34]. Even with the acrylic sheet, the coverage of the OD is significantly less than the ID (there are two outer PMTs for every 12 inner ones), so the OD is lined with reflective Tyvek® material manufactured by DuPont. These measures help to compensate for the low coverage of the OD by ensuring light detection.

Čerenkov radiation [35] is emitted by charged particles travelling faster than the speed of light in the water ($0.75\,c$). Electrons in the water are displaced by the passage of the charged particle and emit radiation when they return to their original positions. Under normal circumstances this light would be isotropic and would be lost through destructive interference; however, as the source particle is travelling faster than the light, a constructive wavefront is formed in a cone (figure 2.5), with an angle directly related to the speed of the charged particle and the refractive index of the water:

$$\cos\theta = \frac{c}{vn(\lambda)} = \frac{1}{\beta n(\lambda)} \tag{2.1}$$

where v is the speed of the particle and $n = 1.33$ is the refractive index of water [8].

In Super-K, this cone of light will appear as a ring of PMT hits, and some examples can be seen in figure 2.6. (This is only true for particles stopping in the ID, as a

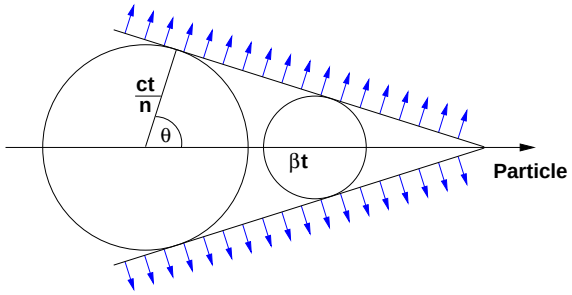

Figure 2.5: A cartoon showing the production of Čerenkov radiation. The particle travels horizontally, covering distance βt in the time period. In the same time period, the light from the start point has travelled $\frac{ct}{n}$ in all directions, and for the angle θ this creates a wavefront. The overall effect is to have a cone of light, centred on the charged particle's direction of travel.

particle which leaves the ID will produce a full circle of hits, with varying time). The muon ring is seen to be very sharp; this is because the muon passes through the water with only minimal interaction, following its original path almost until it stops. In contrast, the electron causes an electromagnetic shower, a number of electrons, positrons and photons travelling in roughly the same direction as the initial electron. The charged particles in this shower still produce Čerenkov radiation, but because of the variation in direction (increased by scattering with the water) the ring is not as well defined, with many PMT hits away from the fitted circle. The fitting of the PMT hits to this ring is the main particle identification method used by Super-K, and the next section covers an important background introduced by this procedure.

2.2.1 The π^0 Background in Super-K

The requirement that a particle is travelling faster than the local speed of light provides a simple minimum energy for particles to produce Čerenkov radiation. However, the number of photons (dN) emitted per unit wavelength (λ) per unit distance (dx) travelled by the particle is given by:

$$\frac{d^2N}{dxd\lambda} = \frac{2\pi\alpha}{\lambda^2}\left(1 - \frac{1}{(n(\lambda)\beta)^2}\right) = \frac{2\pi\alpha}{\lambda^2}\sin^2\theta \tag{2.2}$$

where α is the fine structure constant. Therefore, the actual condition for a particle to be detected is that it must travel a long enough distance with $\beta \approx 1$ to produce enough photons for the Super-K PMTs to pick a ring out of the noise.

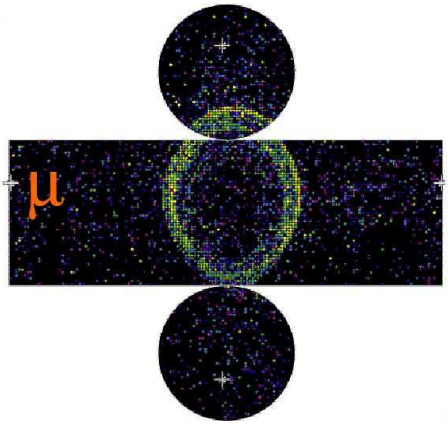

(a) Muon event

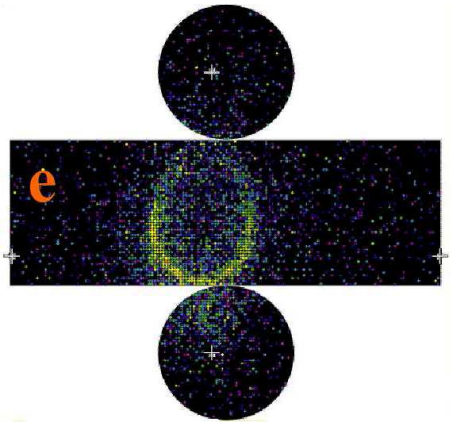

(b) Electron event

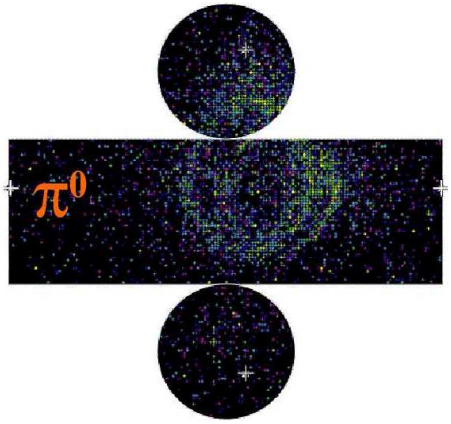

(c) Neutral Pion event

Figure 2.6: Some example Super-K events, showing three signatures. (a) shows the sharp ring of a muon event, with relatively few hits outside the ring. In contrast, the electron (b) produces a 'fuzzy' ring, as all the particles in the shower are travelling in slightly different directions. A photon produces an identical signal, so the π^0 event (c) shows two electron-like rings.

This minimum is not a problem for directly measuring the ν_e appearance signal at Super-K – the threshold for electron detection is 5 MeV [36] and the neutrinos have a considerably higher energy – but it does introduce a significant background to the measurement, namely coherent neutral current π^0 (NCπ^0) production,

$$\nu(k) + A \rightarrow \nu(k') + \pi^0 + A \tag{2.3}$$

where A is the nucleus. In Super-K, this nucleus is assumed to be oxygen, as this contributes the majority of the H_2O target's mass.

The π^0 will decay to two photons 98.8% of the time, and both of these photons will create electromagnetic showers. In some situations, the photons will be of sufficient energy and angular separation that two distinct rings can be reconstructed (figure 2.6(c)), and if this is the case the energy and direction of the two showers can be used to reconstruct the invariant mass of the parent particle and identify the π^0.

However, an event can be misreconstructed as a single-ring, electron-like event. Asymmetric splitting of the energy between the two photons can lead to the lower energy photon being missed, or approximate alignment of the photon directions can produce two overlapping rings, which the reconstruction cannot distinguish from a single ring. One of these misreconstructions is expected in approximately 25% of NCπ^0 events [37]. This becomes a major background to the ν_e appearance measurement, with the added problem that the neutrino energy would be incorrectly calculated, changing the energy spectrum.

In T2K, the off-axis near detector will measure the π^0 production cross-sections on a water target, so that the production rate at Super-K can be estimated and subtracted from the sample. The full π^0 analysis is still being developed by the ND280 software group, but this requirement is the main driving force behind the photon reconstruction work detailed in chapter 4.

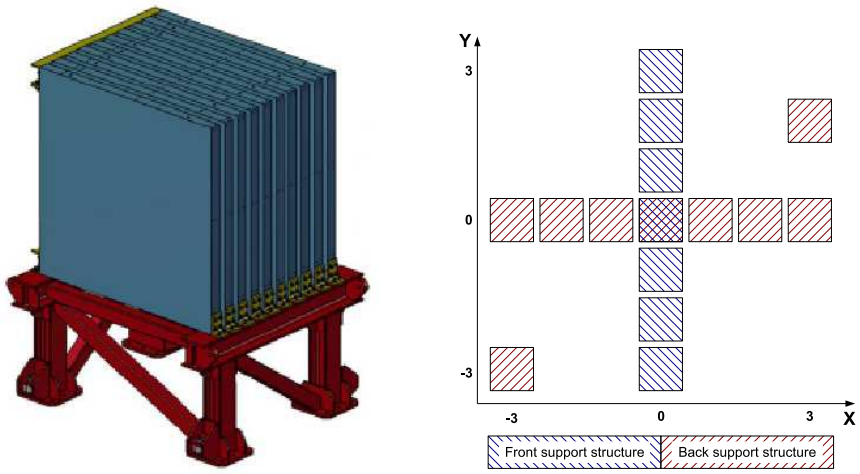

(a) A single INGRID module (b) The INGRID detector layout

Figure 2.7: Left: A single module, showing the layered design in close-up. Right: The arrangement of the 16 INGRID modules showing the crossed design, including overlapping central modules, and the two additional modules in the top right (3,2) and bottom left (-3,-3).

2.3 The INGRID Detector

The near detector suite at 280 metres is split into two parts; the on-axis INGRID detector and the main off-axis detector ND280, covered in the next section. The INGRID detector is to be used to directly measure the neutrino beam's flux and profile, looking for any shifts in the beam direction or asymmetries. There will be 16 identical modules (see figure 2.7), each having 11 scintillator tracking layers and nine iron planes of depth 6.4 cm and 120×120 cm^2 in size. A module is surrounded by four veto planes on the sides. A tracking plane consists of a horizontal and a vertical layer of scintillator strips ($5 \times 1 \times 100$ cm^3), with silicon-based photosensors for readout (as described in section 2.4.8).

The modules will be positioned to measure the beam shape, with 14 modules forming a cross. This will consist of a tower of seven modules in front and a row of seven modules behind, aligned so that the central modules overlap at the expected centre of the beam. The two remaining modules will be used as cross-checks to ensure the shape of the beam, with one in the (-3,-3) position and the other in the (3,2) position. As a whole, they should be able to measure the direction to an accuracy of 1 mrad and observe a 1 mm shift at the target.

2.4 The Off-Axis 280m Near Detector (ND280)

The 280m off-axis near detector is the most complicated of the near detectors, as it contains two main regions, five sub-detector types, and two separate detector technologies: plastic scintillator and time projection chambers (TPCs). All of these are contained in the UA1 or NOMAD magnet [38, 39], donated to T2K by CERN.

The magnet provides a horizontal, uniform 0.2 T magnetic field, perpendicular to the neutrino beam. This field is vital for charge determination and, combined with a radius of curvature from the TPC, can provide a precise momentum measurement [40].

The magnet also sets a number of constraints on the detector design. The internal volume is $7.5 \times 3.5 \times 3.5\ \mathrm{m}^3$, which determines the available size for the detector components. There are gaps in the magnet yoke, through which the requisite cables and pipes will be routed, but there is insufficient space for each channel of the detector. Therefore, each sub-detector within the yoke will have its electronics mounted adjacent to the active volume, and the data will be carried out by optical Ethernet cables.

Also, the standard photosensor technology used for plastic scintillator detectors, the multi-anode photomultiplier tube (MAPMT, as used in SciBooNE and explained in chapter 5), is sensitive to magnetic fields and was deemed unsuitable. This led to a search for alternative photosensors and the solution is described in section 2.4.8.

An understanding of each sub-detector is required to fully understand the work described in this thesis. As mentioned in section 1.4, ND280 has two main detector regions, the tracker and the π^0 detector (P0D), which can be seen in figure 2.8. The tracker region is at the downstream end of the magnet, and has three sub-detector types. The target mass is provided by two fine grained detector (FGD) regions, which are sandwiched between the three TPCs. This region is then surrounded on five sides by electromagnetic calorimeters (ECals), which are designated as the downstream ECal and four barrel ECals (DsECal and BrECals).

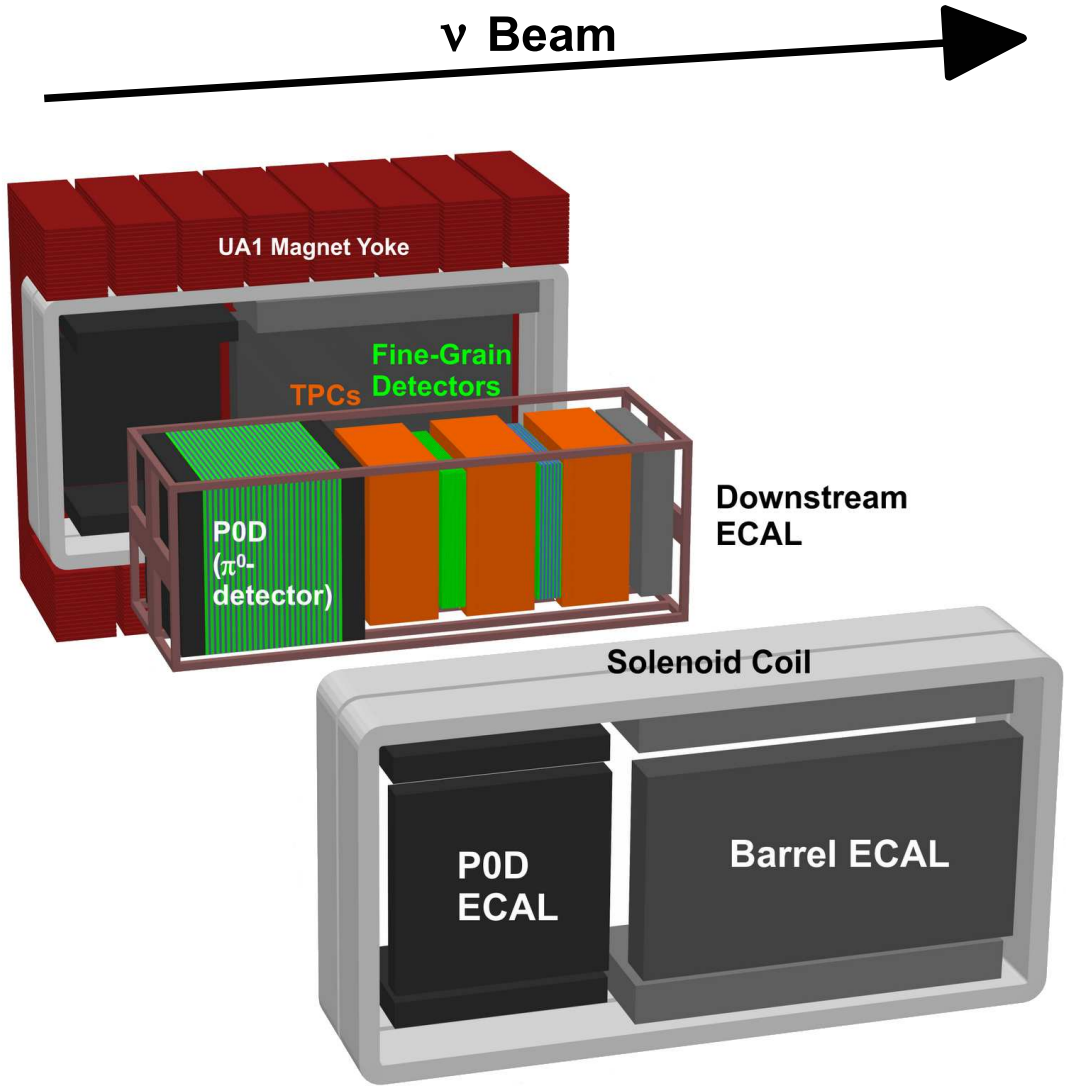

Figure 2.8: The 280m near detector. The magnet is shown in its open position, with the closest magnet yoke removed for clarity. All the sub-detector regions are marked, as well as the magnet yoke and coils. The acronym TPC refers to time projection chambers (section 2.4.3) and ECAL refers to electromagnetic calorimeter (section 2.4.4). Figure provided by Y. Uchida.

The upstream region, the P0D region, is predominantly a single sub-detector, also referred to as the P0D. It acts simultaneously as target and active detector, with a repeating XY layer design of water target, scintillating layers and brass absorber. On the upstream and downstream ends of the P0D, outside of the fiducial volume, the water target is no longer required and the brass is substituted with lead, to increase the containment of the sub-detector. The P0DECal is placed on the four sides of the P0D; it will detect particles leaving the side which may have passed between scintillator layers and produced no clear signal in the P0D.

The P0D, FGDs, TPCs and DsECal are held inside a stainless steel frame, called the 'basket', approximately $6.5 \times 2.6 \times 2.5$ m^3 held by an external support structure. The BrECal and P0DECal sections are attached directly to the magnet's yoke and coils. The final sub-detector, the side muon range detector (SMRD), is installed directly into gaps in the magnet, and uses the magnet mass to determine the energy of muons, based on the distance they travel.

2.4.1 The Tracker Region

The first main region is the tracker, which is in the downstream position and primarily designed for CCQE measurements of both ν_μ and ν_e. As discussed in section 1.2, both of these measurements are characterised by a single charged lepton and a recoil proton:

$$\nu_{\mu/e} + n \rightarrow \mu/e^- + p \tag{2.4}$$

These measurements are two of the most important for the ND280 as they provide the flux of ν_μ's and ν_e's in the beam before any oscillation can occur. Since the target nucleus is essentially stationary before the interaction, the energy and direction of the lepton are sufficient to reconstruct the energy of the incoming neutrino, once its direction has been assumed. If the direction and energy of the proton can also be measured, then it is possible to fully reconstruct the incoming neutrino. The neutrino beam may be a point source when the neutrinos have reached Super-K, but at the ND280 the decay volume can still be seen as an extended volume with

only a subset of the neutrinos heading towards Super-K, so this full reconstruction is very useful.

To make these measurements possible, the tracker region was designed with an active target region, the FGDs (section 2.4.2), with a fine enough segmentation to record short tracks from low energy protons. The FGD must have sufficient mass to produce a large number of interactions, but it is important that charged leptons are not stopped in the FGD. Instead, they must be allowed to reach the TPCs (section 2.4.3). This is where the 0.2 T field of the magnet is used to the best effect; a TPC is a low density active region, providing excellent spatial resolution with a low probability of scattering. As the lepton travels through the field, its path is bent and the radius of curvature gives the momentum.

Having the interaction point, initial direction and momentum, the only remaining requirement is to determine the particle type. Whilst both the FGD and TPC have some capabilities for this task, an electromagnetic calorimeter (ECal, section 2.4.4) will surround the tracker region on five sides (the sixth is the upstream end, covered by the P0D, discussed in section 2.4.5). The ECal has layers of lead, which provide sufficient mass to trigger a shower for an electron. Distinguishing showers from tracks in the ECal will be covered in detail in section 3.4.5, but in general it is possible for all but the lowest energy particles.

The tracker region will be used for many other measurements as well, including providing a cross-check of the π^0 production channels. The FGD will again provide the target mass for the interaction, the ECal will reconstruct the photons created by the π^0 decay and the TPC will be used to veto any showers associated with a track, as only charged particles will create a track in a TPC.

2.4.2 The Fine Grain Detectors (FGDs)

The two FGDs act as the target mass for neutrino interactions in the tracker region. They are constructed from $0.96 \times 0.96 \times 184.3\,\mathrm{cm}^3$ bars of extruded polystyrene

scintillator, with a central wavelength-shifting fibre. Each fibre is mirrored with aluminium at one end, with the other end leading to a silicon photosensor and electronics (sections 2.4.8 and 2.4.9). The two FGDs are of the same external dimensions, 230 (W) $\times$ 240 (H) $\times$ 36.5 (D) cm^3, but with different internal structures. The upstream FGD contains 5,760 bars, 30 layers of 192 bars each. Each layer will be orientated in either the X or Y direction, perpendicular to the neutrino beam, and this orientation will alternate between layers, so as to give as close to 3D positioning as possible with the technology.

The downstream FGD has an identical XY design, but with fewer layers as space is assigned to a water target mass. It has seven XY pairs alternating with six 2.5 cm thick water modules, segmented polycarbonate panels filled with water and sealed at the ends with glue. This difference in design allows for a subtraction measurement, determining both the carbon and water cross-sections. The efficiency of reconstructing events from each FGD will depend on location in the detector, so the two FGDs will be interchangeable.

The main requirement for the FGD is to reconstruct particle tracks and determine if they are from the same neutrino interaction vertex. In a standard CCQE event, two significant particles would be expected to leave the vertex, a charged lepton (e^- or μ^-) and a proton. In most cases, the lepton will leave the FGD and be detected in the TPCs and/or ECals, but the proton will not have as much momentum, so will normally deposit a large amount of energy in only a few bars of the FGD. Sometimes this will be enough to reconstruct into a short track, otherwise it will be a large deposit in the same area as the start of a lepton track; but either way this defines the vertex.

When matching hits between FGD and TPC regions, the time of the track becomes important (the cause of which is explained in the next section). The TPC drift speed is expected to be 6.5 cm/µs, which defines the reliance of the spatial resolution on the time resolution, so the FGD group opted to use a continuously sampling ASIC, instead of the ADC and TDC (analog- and time-to-digital converters respectively) combination used by the other scintillator-based detectors. This allows the

reconstruction software to separate tracks from multiple interactions, and to tightly define the start time of TPC tracks.

2.4.3 The Time Projection Chambers (TPCs)

Designed to reconstruct the path of a charged particle in 3D without interfering with the path, each $1 \times 2.5 \times 2.5$ m^3 TPC will have a central active volume, filled with Ar:CF_4:iC_4H_{10} (95:3:2) gas [41]. The volume is split in half in the X direction by a central cathode plane in YZ (figure 2.9(a)). The two ends parallel to this plane are tiled in MICROMEGAS modules [42], as can be seen in figure 2.9(b).

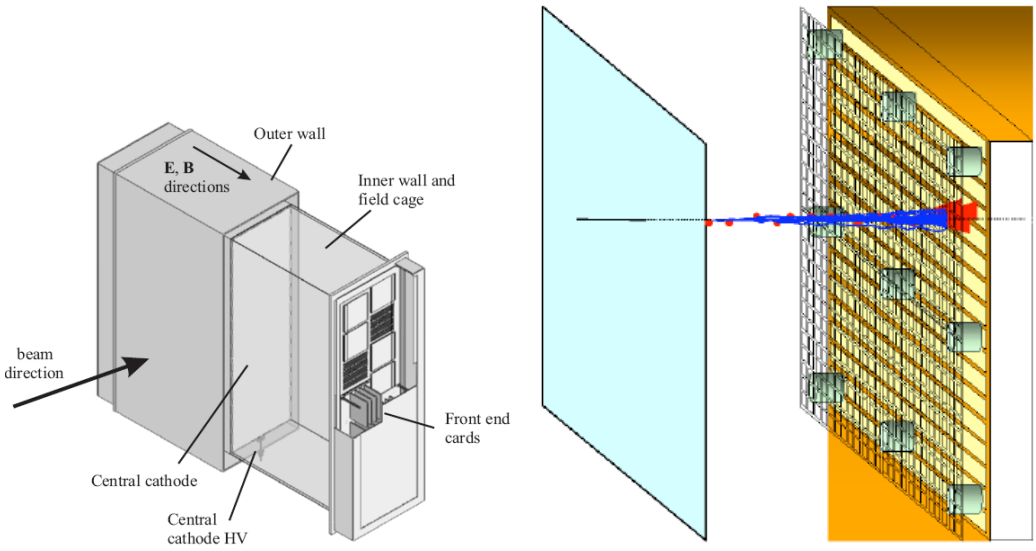

(a) A TPC module. (b) A single MICROMEGAS module.

Figure 2.9: The TPC sub-detector, figures taken from [42]. Figure (a) shows the full TPC module, with a cutaway to show the central cathode, the MICROMEGAS modules on the end and the inner wall and field cage. (b) shows a schematic view of a single MICROMEGAS module, with the free electrons in blue and showing the micro-mesh and pads.

Each MICROMEGAS has an array of 6.8×9.7 mm^2 pads, 48 columns by 36 lines, each of which is read out by a front-end electronic card (FEC). The pads are interspersed by a single anode, so when charges are produced in the gas by an ionising particle, they drift towards the cathode or anode. A micro-mesh is held just 50 – 100 µm above the anode plane, and after passing this the electrons trigger an avalanche, producing a signal in the pads.

This provides an accurate position for the track in YZ, but the X position is still unknown. Relative X positions along the track can be calculated from the timing of the signals received, by accounting for the drift speed of the charges in the gas, but to fully define the X position a ΔX must be provided, either by the track crossing the central cathode or by matching the track to objects in the FGD or ECal and getting a t_0 measurement.

2.4.4 The Downstream and Barrel ECals (DsECal and BrECal)

The ND280 ECals will be used to measure the energy of particles produced in the FGDs, with a resolution of $\sim 10\%/\sqrt{E}$. Whilst the TPC will already have measured the momentum of many particles, the ECals have a greater coverage of the area. Also, neutral particles like photons will not be observed in the TPC, but the ECal will have sufficient mass to trigger a shower.

Therefore, a sampling calorimeter with good tracking capabilities was designed, using alternating layers of plastic scintillator and lead. The layers run in local XY planes, so that a particle travelling along Z would repeatedly pass through scintillator and lead. For each module, this local Z is orientated to point back into the tracker region, so that all particles of interest will cross lead layers, instead of running parallel to them. The lead is especially important for detecting photons, which will not produce a signal in the detector until they have been made to shower, creating a cascade of electrons and positrons.

An early version of the analysis in chapter 4 was used to specify the ECal, determining the optimum lead thickness and bar size for a detector to be able to reconstruct, with good positional and directional resolution, muons, electrons and photons. This work was included in the T2K UK proposal [43], contributing to large parts of chapters 4 and 5. The effect of bar widths, bar orientations and lead thicknesses were considered on the efficiency of the π^0 measurement and the energy reconstruction (figures 4.8 – 4.10). Figure 5.1 also addressed the containment of the ECals, studying the fraction of photons that were likely to lose 10% or more of their energy out of the back.

The ECal is considered in three separate sections, the downstream ECal, the barrel ECal and the P0D ECal. The P0DECal will be discussed in detail in the next section, but is essentially a descoped version of the other two ECals, with fewer layers and only one bar orientation. The DsECal is a single module, which will sit in the basket at the downstream end.

The BrECal surrounds the tracker region on four sides and is split into a number of modules, for ease of construction and installation. As the BrECal is attached to the magnet and coils, there are six regions: top, bottom and side on both left and right clams. The full sizes and arrangements of each region can be seen in table 2.1.

Region	Size W × L × D (m^3)	# of Layers	Bars per Layer	Lead per Layer (mm)
Downstream[a]	2.0 × 2.0 × 0.5	34	50	1.75
Barrel[b]				
Top/Bottom	4.2 × 1.5 × 0.5	31	105 / 37	1.75
Side	4.2 × 2.3 × 0.5	31	105 / 57	1.75
P0D[c]				
Top/Bottom	1.4 × 2.3 × 0.5	6	35	4.0
Side	2.6 × 2.3 × 0.5	6	58	4.0

[a]All bars have double-ended readout
[b]Long bars have double-ended readout
[c]No double-ended readout, only 1 orientation

Table 2.1: Details of each ECal region, including the size, lead thickness, number of layers and bars and whether the bars have double- or single-ended readout.

Each ECal module is a layered scintillator detector, with a thin sheet of lead foil separating the layers. A scintillator layer is constructed from extruded scintillator bars, 4 cm wide and 1 cm high, with a Kuraray Y11 WLS fibre running through a hole in the centre of each bar. The length of the bar varies depending on the size of the individual ECal module, with the shortest bars (1.5 m) in the top and bottom barrel sections and the longest (4.2 m) also in the barrel, running the full length of the tracker.

For the tracker ECals, each layer has bars orientated perpendicular to the previous layer, so that the side BrECal, for example, has bars measuring YX or ZX. For reconstruction purposes, each ECal is initially treated as two 2D detectors, and

then reconstructed 2D track and shower objects can be matched to form a full 3D object.

The bars are read out using MPPC photosensors, attached directly to the end of the fibres and described in section 2.4.8. The attenuation length of the Y11 fibre is ∼350 cm, so the effect is minimal for the shorter bars. For the longer bars however, a hit at one end might not be detected by a photosensor at the other end, so both ends are instrumented. As the DsECal is expected to have the highest multiplicity and be the most important for measuring high energy leptons from CC events, it was decided that it should also have double-ended readout, to maximise the information available. In bars with only one photosensor, the other end of the bar will be mirrored, by depositing a reflective aluminium layer on the polished fibre end.

The signals from the photosensors are sent to a TRIP-T front-end board [44], which uses the TRIP-T chip to record two ADC values (high and low gain channels) and a TDC value for each photosensor. The integration period will be set to 241.0 ns, triggered by the beam spill, and has a reset time of 50.0 ns. Because of this, the software treats each spill as a separate event; the only signal expected later than the specific integration window would be electrons produced in the decay of stopped muons, called Michel electrons after physicist Louis Michel [45].

2.4.5 The π^0 Detector (P0D)

The P0D is the central sub-detector of the other main region, which is also usually referred to as the P0D. This region has been specifically designed for NC and CC π^0 measurements, characterised by a di-photon signal. Unlike the tracker region, which has specific target regions sandwiched between high resolution tracking detectors, the P0D is a single unit which attempts to contain as much of a photon's energy as possible.

Like the FGD and ECal, the P0D uses a layered design, with plastic scintillator, WLS fibres and MPPCs used for the active regions. These active layers are constructed

as P0Dules, with one X and one Y layer between two thin sheets of PVC to keep it light tight.

Because spatial resolution and pointing of the showers is so important, the P0D uses triangular bars, arranged as in figure 2.10. As a particle passes through a layer, it will normally create scintillation light in at least two channels, and the ratios will allow the reconstruction to measure the position with greater resolution than the width of an individual bar.

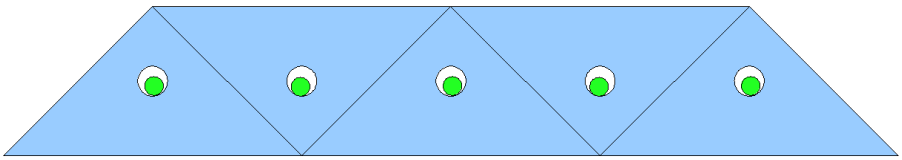

Figure 2.10: A cartoon of the bars in a single P0D layer.

The P0D also includes two types of inactive layer, targets and radiators. The target layers are water cells, semi-flexible pillow bladders of size $0.03 \times 1.8 \times 2.1$ m^3 which hold approx 100 kg of water each. This provides an oxygen target mass, so that the important cross-sections for Super-K can be measured on the correct target.

The radiator layers are included to force photons to convert and shower. The P0D uses two different materials as a radiator, brass and lead. As the radiation length of lead is significantly shorter than brass (6.37 g/cm^2 or 0.56 cm compared to 12.81 g/cm^2 or 1.51 cm [8, 46]), lead will stop particles much more quickly, but will also decrease the available information for reconstruction of the energy and direction. As such, the central target region of the P0D has a repeating structure of P0Dule, 1.6 mm brass radiator, water target, with 25 iterations and a final P0Dule to finish.

The regions on the upstream and downstream ends of the P0D are the upstream ECal (USECal) and the central ECal (CECal) respectively, as they are designed to ensure that as little as possible of a photon's energy escapes the P0D. They are similar in design to the target P0D region, but the water regions are removed (these are only of use in the fiducial region) and the brass sheets are replaced with lead,

4.0 mm (USECal) or 4.4 mm (CECal). As both are seven layers thick, the CECal represents 5.5 X_0 of lead.

One disadvantage of the design is that all the lead and brass is in XY planes. The majority of the photons will be travelling in the downstream direction, due to the momentum of the incoming neutrino, but a proportion will travel perpendicular to the beam, and will encounter no radiator to trigger a shower. Therefore, the P0DECal is placed on four sides of the P0D, to record any particles leaving the sides. Using the same scintillator bars as the tracker ECals, the P0DECal is not intended to fully reconstruct objects, but only to note their passing and give an indication of the energy and particle type. It will have only six layers of scintillator, all arranged in the same orientation, and five layers of lead 4.0 mm thick.

2.4.6 The Side Muon Ranging Detector (SMRD)

The final sub-detector of ND280 is the SMRD, which will be used to measure the energy and direction of muons from CCQE interactions and also provide a trigger for through-going cosmic ray muons which the other sub-detectors use for calibration. Whereas the other sub-detectors are all placed in the inner volume surrounded by the magnet and coils, the SMRD is placed inside the magnet yokes, using the iron to range out muons.

Each clam of the UA1 magnet yoke is made of eight segments, referred to as Cs because of their shape (figure 2.11). A single C consists of 18 layers of iron, expanding radially outwards. The layers are constructed from 48 mm thick iron plate, and have 17 mm air gaps between them. The spacers are separated evenly, splitting the gap into 12 azimuthal sections. Four of these sections are in the corners, meaning the size varies with the layers, but the eight remaining sections are all of constant size, $876 \times 910 \times 17\,\text{mm}^3$ for the horizontal and $876 \times 700 \times 17\,\text{mm}^3$ for the vertical. A selection of the gaps will be filled with plastic scintillator modules.

The decision of which regions to instrument is made based on a compromise between the two goals of the SMRD. For the detection of outgoing CCQE muons, the side

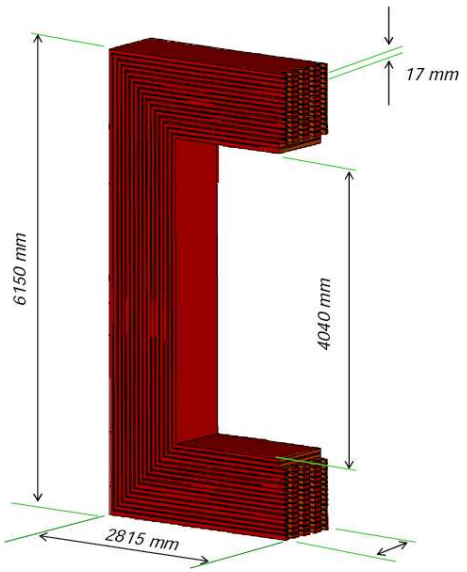

(a) A single yoke C

(b) The gaps in the C

Figure 2.11: Left: A single C from the UA1 magnet yoke. Right: A close-up of the gaps in the magnet.

regions are favoured, with an emphasis on the downstream end. The muons are more likely to be travelling in a downstream direction, and the added mass of the magnet coils in front of the top and bottom regions decreases the number of muons, as well as deteriorating energy resolution.

However, for the detection of cosmic ray muons, the top and bottom regions are most important and should be instrumented evenly so that all sub-detectors will receive useful cosmic triggers. As such, all Cs will have three layers in both the top and bottom regions, and the side regions will vary from two layers for the three most upstream Cs up to six layers for the two downstream ones.

To instrument the sections, a number of extruded scintillator slabs are used side by side in each gap. For horizontal gaps there are four slabs of size $876 \times 175 \times 7$ mm^3, while the vertical gaps have five slabs at $876 \times 167 \times 7$ mm^3. A single slab can be seen in figure 2.12, where the S-shaped WLS fibre is visible. A straight fibre would not have received enough light from particles passing through the edges. The fibre is then read out at each end by MPPCs, to ensure the maximum light yield. Photosensors from each azimuthal section of a C will go to the same TFB, so that towers are created which can be used to produce cosmic triggers (see section 2.4.9).

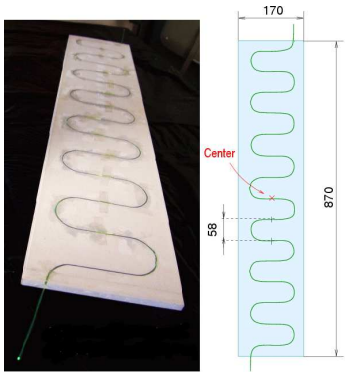

Figure 2.12: A prototype SMRD scintillator slab, with a WLS fibre inserted into a machined S-shape groove.

2.4.7 Plastic Scintillator and Wavelength-shifting Fibres

The majority of the ND280 detector uses plastic scintillator as an active medium. For decades, all plastic scintillator was created using an expensive casting procedure, but recent improvements have lead to extruded scintillator, which can be produced more cheaply and with complex cross-sections [47]. The extrusion method starts with pellets of polystyrene and the two dopants, PPO and POPOP, which are heated and forced through an extrusion die.

The die is varied for each sub-detector, but as an example, the ECal bars produced at Fermilab will have a die that produces a 4×1 cm^2 rectangular bar, with a central 1 mm hole for the WLS fibre. As the extrusion is a continuous process, the length of the bars is easily varied.

Polystyrene does not naturally scintillate, so two different dopants are added during extrusions. The first substance, Poly(p-phenylene oxide) or PPO, is an organic scintillator and a 1% dopant. It absorbs the ionising energy of the passing particles which excite a π-orbital electron into a higher energy state. When the electron de-excites it releases light, which becomes the signal for the ND280 detector.

The second, 1,4-bis(5-phenyloxazol-2-yl) benzene or POPOP, is a secondary or wavelength-shifting scintillator and is included as a 0.03% dopant. This is included because the light produced by PPO is at a wavelength quickly attenuated in the

scintillator. POPOP will absorb the first scintillated light, and then emit it as a higher wavelength (the spectrum peaks at 410 nm).

A quenching effect has been observed in scintillators, due to the fact that energy produced from ionisation must interact with a dopant molecule that is not currently in an excited state. As the energy deposited increases so will the light produced, but then the availability of such molecules decreases, limiting the growth. This has lead to a semi-empirical formula by Birks [48]:

$$L(E) \propto \int_{E_{min}}^{E_{max}} \frac{1}{1 + k_B \cdot \frac{dE}{dx}} \cdot dE \tag{2.5}$$

where k_B is a material-specific parameter and $\frac{dE}{dx}$ is the energy loss. This effect has been studied in detail for plastic scintillators [49], and is especially important for protons which can deposit a large amount of energy in a short track.

The attenuation length of the plastic scintillator is of the order of 40 cm [50], much shorter than the length of even the shortest ND280 bars. This necessitates the use of wavelength-shifting (WLS) fibres, running down the centre of the bars. The scintillation light that enters the fibre is absorbed by a scintillating dopant in the fibre. The emitted light comes out at higher wavelengths, predominantly above the absorption range of the fibre's dopant. For this light, the fibre acts like a normal optical fibre, and the light will propagate to the end via total internal reflection (this applies only to light produced below the limiting angle – the other light will leave the fibre and be lost). The fibre selected is Kuraray Y11(200), which has an attenuation length of 350 cm, much longer than the extruded scintillator.

2.4.8 Multi-Pixel Photon Counters (MPPC)

As mentioned earlier, the use of the NOMAD magnet for ND280 applied a lot of constraints on the detector, and many of these were on the photosensors selected. The devices had to be small enough that they would fit inside the magnet, otherwise each channel would require its own fibre optic to be fed out through the limited gaps in the magnet. This decision then imposed a requirement that the device work in a 0.2 T field.

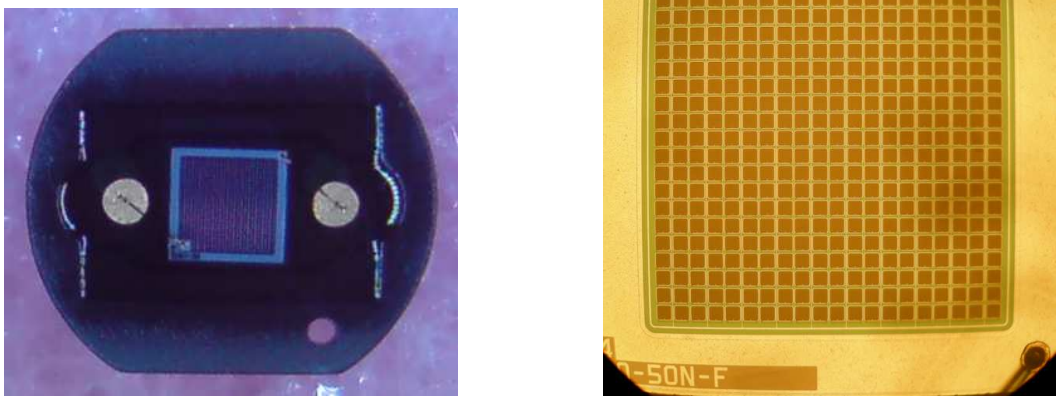

(a) The MPPC photosensor (b) Close-up of a MPPC's active area

Figure 2.13: The MPPC is a pixelated silicon device, with each pixel acting as an Avalanche Photo-Diode in Geiger mode. Images courtesy of A. Vacheret and J.F. van Schalkwyk.

The photosensors selected by the ND280 were Hamamatsu S10362-13-050C (figure 2.13(a)), as they have a small size and are insensitive to magnetic fields, as well as being low cost. The active area of the device, shown in figure 2.13(b), is a square, area 1.69 mm^2, which is separated into 667 50 $\times$ 50 μm^2 pixels (a 3 $\times$ 3 pixel block is removed from one corner for connections). Each pixel is an avalanche photo-diode (APD) running in Geiger mode, where a reverse bias voltage V_{OP} greater than the breakdown voltage V_{BD} has been applied.

In this state, a photon incident on the pixel surface can create a carrier, which is accelerated by the electrical field and triggers a Geiger discharge. Each pixel fired will then contribute

$$Q_{PIX} = C_{PIX}(V_{OP} - V_{BD}) \tag{2.6}$$

to the signal, where C_{PIX} is the pixel's capacitance.

As a stable difference in voltages is usually about 1V (compared to a V_{BD} of $\sim$70 V) and the capacitance can be from 50 to 150 fF, then (2.6) gives a gain of the order of 10^6 electrons/photon. A resistor R_{PIX} is integrated into each pixel, so after the avalanche it will recover with a time constant $R_{PIX}C_{PIX}$, which is set to $\sim$10 ns.

As the charge produced by each pixel is a set value, with low light levels it is possible to observe peaks corresponding to different numbers of photons, as can be

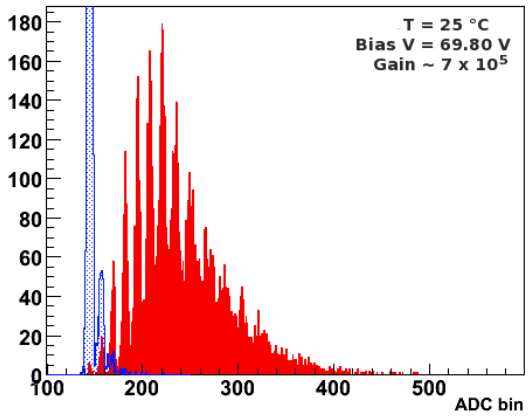

Figure 2.14: An example of the response of the MPPC photosensor, when connected to the high gain channel of the TFB [44]. The blue distribution is with no light falling on the MPPC; the pedestal can be seen, with two higher peaks caused by dark noise. The red distribution is with light, and approx separated 10 p.e. peaks can be seen.

seen in figure 2.14 (hence the devices are called photon counters). At higher levels of incident light, the linearity of the device suffers due to the pixelated design; as each successive photon falls on the sensor, there is a increasing probability it will fall on a pixel which has already fired and no further signal will be produced. However, the majority of the important signals will be at the lower light levels; low energy photon showers may only produce enough scintillation light in a bar for a handful of photons to reach the photosensor. As such, the large dynamic range is seen as more important than the linearity at high light levels.

Noise in the MPPCs is observed in two forms, dark count and cross-talk. The latter refers to charge from one discharging pixel leaking into a neighbour, causing it too to discharge. This affects the linearity of the device, but has no other effects on the signal.

In contrast, dark count is the situation in which a pixel discharges without any photons incident on the surface, normally due to thermal excitation. This noise is therefore not associated with a real hit, and as an MPPC typically has a dark count rate in the rage 300 – 800 kHz/mm^2 at the single p.e. level, it is important to consider this at the reconstruction stage.

The double p.e. dark count rate tends to be an order of magnitude lower, but this still

represents a large number of noise hits in a detector with so many channels. As an example, the DsECal has 3,400 channels, so with an integration window of 241.0 ns and a 1.69 mm^2 device, there are expected to be 40 – 110 double p.e. noise signals per bunch. Therefore, when a full analysis of the noise rate has been completed, the threshold for a hit will be adjusted, so that the rate is considerably lower than the present double p.e. estimate.

2.4.9 ND280 Electronics

The signals from the photosensors are sent to one of two different front-end boards. The ECals, P0D, SMRD and INGRID all use the Trip-T (Trigger Pipeline + Timing) chip [51], which was developed for the D0 experiment, whilst the FGD uses the AFTER chip [52]. This chip was developed for the TPC (AFTER stands for ASIC For TPC Electronics Readout [41, 53]) and has time resolution characteristics optimised for the FGD.

Trip-T Front-end Board (TFB) for ECal, P0D, SMRD and INGRID channels

Each TFB will read out 64 MPPCs, and 48 TFBs will feed into a single readout merger module (RMM) for data to be collated and sent to the data acquisition system (DAQ). A Trip-T chip has 32 input channels, each of which consists of an integrating preamplifier and a second adjustable amplifier, feeding into an analog pipeline. The pipeline is 48 cells deep, so in normal running the preamplifier integration will be triggered by each bunch, with a minimum 50 ns reset time between bunches. After the full spill, the pipeline will be read out and digitised by an ADC, before being transmitted off the board.

The electronics must be capable of handling the full dynamic range of the MPPC and still be capable of separating a single p.e. signal from the electronics noise. However, the Trip-T is not capable of providing the full dynamic range desired, so the signal from each MPPC is split between two channels. Figure 2.15 shows the

MPPC to Trip-T interface, with the signal being split between three capacitors, C_G, C_{HI} and C_{LO}. The high to low gain ratio is determined by the ratio of C_{HI} to C_{LO}, with an intended value of 10 to 1. The overall gain is determined by the value of C_G and this is tuned to ensure that the full range of the MPPC is covered by the low gain channel.

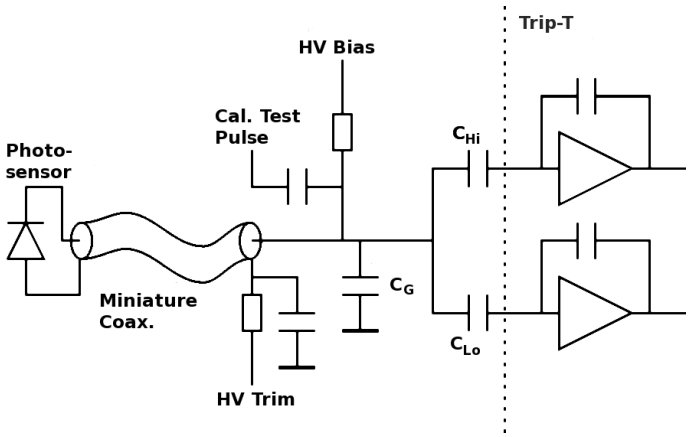

Figure 2.15: A schematic of the MPPC connection to the Trip-T chip, showing the three capacitors for controlling the gain and the voltage trim.

Figure 2.15 also shows the high voltage (HV) trim voltage applied by a digital to analogue converter, a chip which provides a tunable voltage. This is unique to each MPPC and can be set from 0 to 5 V, so that the gain of each individual photosensor can be adjusted to keep the signal in the correct ranges.

The final requirement of the Trip-T is to timestamp the signals recorded. This is done by extracting the signal before the adjustable amplifier, and passing it through a set $\times 10$ amplifier and into a discriminator with an adjustable threshold. The Trip-T chip offers the choice of using the high or low gain channel for this, but as the desired threshold will be around 3 to 5 p.e. the high gain is the obvious choice. The output from this discriminator is then passed to the field programmable gate array (FPGA), a chip which handles not only the timestamping but also all the control requirements and slow controls of the TFB.

Therefore, for each MPPC in the ECal we would expect to receive three values per bunch; ADC values from the high gain and low gain channels and a timestamp. If the charge in an MPPC signal does not go above the discriminator threshold, then

the timestamp will essentially be void, and information useful to the reconstruction will have been lost. However, if the threshold is lowered instead, then noise in the MPPC occurring before a true deposit might trigger the discriminator. In this situation, you have a large charge deposit and a time value significantly before the real time. As the reconstruction will rely on timing information to associate the correct objects, this incorrect timestamp will have a more significant effect than the missing timestamps for low charge signals.

Studies have shown that for a 1.5 p.e. threshold, a 2.5 p.e. signal will have a time resolution near 1 ns, but the timestamp of a 1.5 p.e. signal will vary over 100 ns. The 1.5 p.e. threshold would allow double p.e. dark count to trigger the TDC, which will occur in approximately 1% of channels within a bunch.

Front-End Card (FEC) for TPC and FGD channels

The central component of the FEC is the AFTER chip, a 72 channel ASIC specifically designed for T2K. For the TPC, each MICROMEGAS pad will connect to a channel and then be continuously sampled into analog memory. The chip allows for 511 samples, with a frequency of 1 – 50 MHz, and when triggered these are fed into an external ADC.

As mentioned earlier, the X position of a TPC track is reconstructed by accounting for the drift speed of the free carriers and matching with scintillator-based subdetectors. The resulting output of the electronics is a waveform of charge vs time for each pad. Each peak in the waveform is fitted to a Gaussian and made into a hit in Y, Z and T, which are then passed to the reconstruction software.

The FGD group opted to use the AFTER chip also, so that the time of a neutrino interaction can be known to a higher degree of accuracy than a single timestamp would allow. The continuous sampling at 50 MHz allows for the separation of noise from genuine signals, and the timing resolution for a muon or proton signal is about 3.5 ns. This is especially important when matching tracks between the FGD and TPC.

Another advantage of the better time resolution is the ability to identify a charged pion stopping in an FGD bar. The pion will decay to an almost stationary $\mu^{\pm}$, which will itself produce a Michel $e^{\pm}$, detected by the photosensor significantly later than the initial signal. As the muon decay constant is 2.2 µs long and the beam spill is 5 µs, then a 10 µs alive period for the electronics covers the spill width and two muon lifetimes for all particles. The AFTER chip has a maximum sampling frequency of 50 MHz and 511 time slots, which gives 10.220 µs and matches nicely.

Like the Trip-T, the AFTER cannot provide the full dynamic range needed by the MPPC. The maximum input charge of the AFTER chip is 600 fC, but the maximum output of the MPPC, approx 100 pC (667 pixels and a gain of 10^6), is significantly higher. Therefore the signal must be attenuated before being passed into the AFTER chip. However, applying the constraint that the electronics noise must be lower than 0.2 times the single p.e. signal, and taking the noise at 0.3 – 0.5 fC, then the signal can only be attenuated by 30 – 50. To satisfy the conflict, each MPPC is fed into two channels, with two different attenuation factors. As the gain and noise levels are still being precisely determined, the exact factors are not yet known, but the FGD group would hope to achieve 0.1 to 100 p.e. for the low attenuation channel and 15 to 667 for the high [54].

Chapter 3

The ND280 Software

The ND280 offline software group is responsible for a large range of work, from the initial Monte Carlo simulations of the detector through to the final reconstruction algorithms for all the 280m near detectors, both on-axis and off-axis. The majority of the work has been concentrated on the off-axis sub-detectors, as the INGRID detector is comparatively simple and only recently became part of the ND280 software group.

All ND280 code is written in object-orientated C++, with heavy usage of ROOT [55]; with only a few external packages still using FORTRAN. The software has a number of different functions, and each of those is explained in the following sections (3.1 – 3.5). As the work covered in this thesis was centred on the clustering algorithms of the ECal and the effect these have on several important reconstructions, the ecalRecon package will be covered in section 3.4.5, in much greater detail than the other packages.

The code is maintained as a group of inter-relating packages, each with its own remit. The packages are combined and managed using Configuration Management Tool (CMT [56]), which ensures that each package's dependencies are clearly defined, and Concurrent Versioning System (CVS), an open-source package which provides a version control system, designed to track and archive a software project worked on by a number of developers.

Figure 3.1 shows all the ND280 packages, including those externally maintained, and their dependencies. As the code is constantly being improved, a set state of the code has been selected for this thesis. The first general user release of the ND280 code to the whole T2K collaboration was on 14^{th} Feb 2008, corresponding to v4r1 of nd280, the top level package. Since then, there have been two more release freezes, v4r3 and v4r5.

As significant improvements to the Monte Carlo, electronics simulation and reconstruction had been included at each stage, the v4r5 code was used. Some planned improvements to the ECal reconstruction package were not ready for v4r5, but would have an effect on the results in this thesis, so the current or 'head' version of the ecalRecon package was used, including the addition of ecalCalib, a separate package responsible for the calibration of ECal hits.

3.1 oaEvent, the ND280 Framework

The oaEvent package defines the ND280 data format and event structure. All objects inherit from the TObject ROOT class, and all data, be they Monte Carlo simulations, genuine run time data or reconstruction elements, are stored in .root files.

The ND280 data are stored in an 'event' structure, where 'event' has no set definition beyond being an interesting set of interactions. Each event is considered to be a self-contained unit, unaffected by other events. As such, an individual event can range from a single particle produced with set energy and direction to a full beam spill, with numerous neutrino interactions throughout the ND280 basket, magnet or hall. By introducing a single signal event into one of the FGDs and adding a selection of other beam interactions, it is possible to estimate the effect of the extra interactions on the reconstruction. However, for simplicity's sake, many of the early measurements in chapter 4 are made with single interaction or single particle events.

As can be seen in figure 3.1, oaEvent has a limited number of dependencies, and these packages are the only ones required to read any data file. This was deliberately arranged, so that a correctly configured laptop with only a minimum software

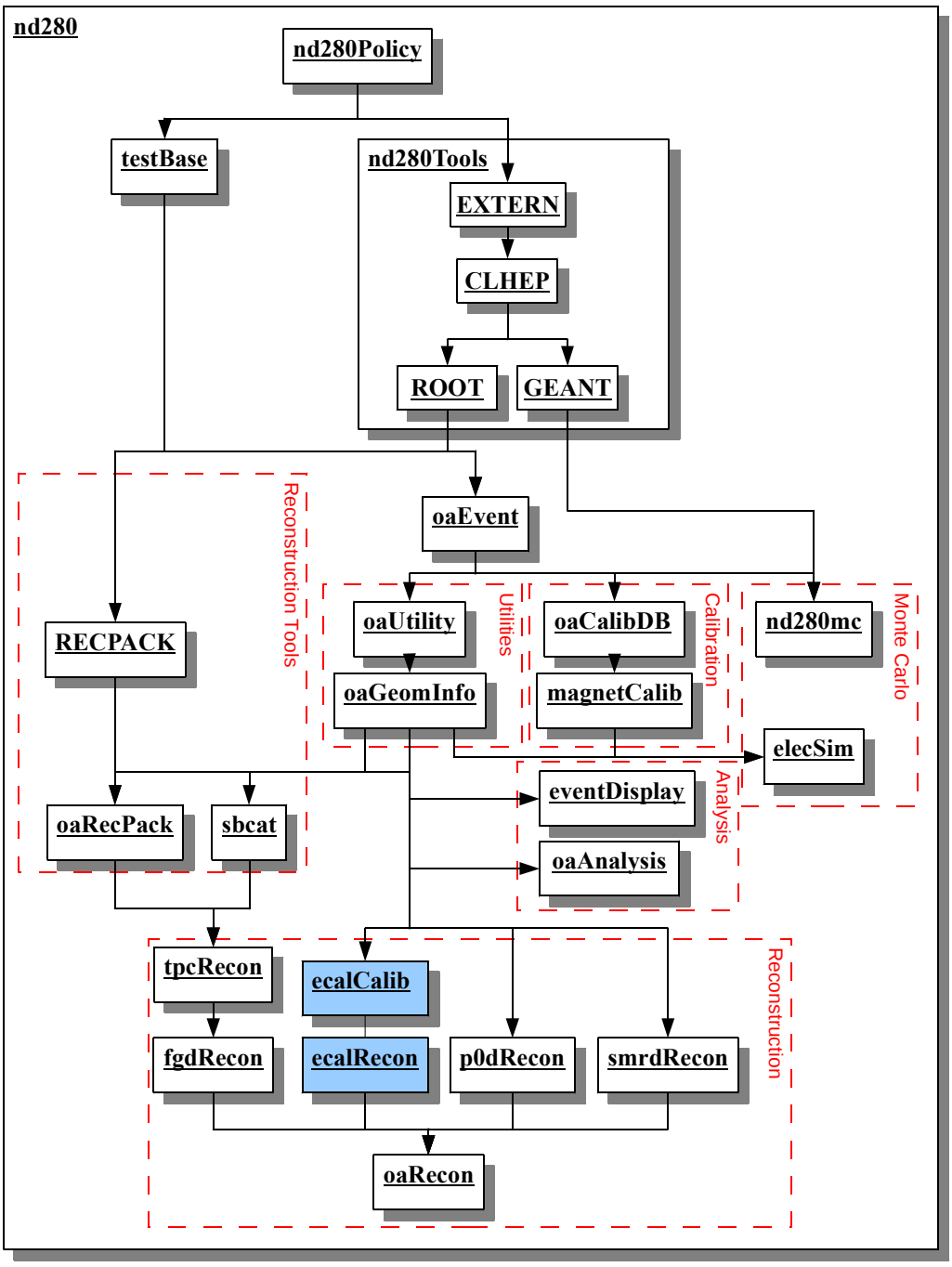

Figure 3.1: Schematic listing showing the dependencies of the packages in version v4r5 of the nd280 software package, released to the collaboration in July 2008. Packages in capitals are externally maintained, with EXTERN providing the tools to include them in nd280 with CMT [55, 57, 58]. Packages where the 'head' version have been used, because of improvements necessary for the work, have been shaded blue.

installation would be sufficient to view and analyse data, more information on which can be found in section 3.5.

3.2 Monte Carlo Production

For a long time, Monte Carlo (MC) has been an important part of particle physics, with increasingly complicated and sensitive detectors requiring more and more detailed MC simulations. The GEANT4 [58, 59] package is a dedicated MC package, maintained at CERN. It provides tools for simulating detector designs and propagating particles through them.

The nd280mc package uses the GEANT4 toolkit to define the ND280 detector and the INGRID, and provides a number of methods for introducing particles to the simulation. The simplest manner is a particle gun approach (as used in section 4.1.1), where single particles are introduced into the detector volume, with a position, direction and energy defined by the user.

The other common method for creating events is to use a dedicated neutrino interaction generator. There are a number of these generators available and the ND280 software group has decided that nd280mc should be generator 'agnostic', working with any generator collaboration that wishes to be involved. At the moment, three generators are in use, NEUT, NUANCE and GENIE. There are many differences between them, both in the internal models used to generate interactions and in their interfaces with the ND280. The differences in the models will not be discussed here, but the use of each generator within ND280 will be commented on.

Written for Kamiokande, NEUT [10, 11] has been continually used for Super-K, K2K and SciBooNE, with regular updates to the models used. Originally written for interactions with the oxygen nuclei of a Čerenkov detector, it has since been adapted for an iron target, but still only generates events against a single target. These events are passed to nd280mc as a list and nd280mc selects a location within the detector based on a density weighting, but the interaction is otherwise unchanged.

The NUANCE [60] generator follows a similar method, with interactions on a single nucleus. Written for the IMB detector [34], it was rewritten for Super-K but not adopted as the official MC. Since then, it has been used by a number of other experiments, such as MiniBooNE [61].

In contrast, GENIE [62] has been deliberately designed for more complicated detector environments. It uses a ROOT geometry of the detector (provided by nd280mc) and a detailed description of the beam flux to more accurately estimate the location of neutrino interactions. An initial expenditure of CPU time allows the generator to calculate splines of the cross-sections for different materials, neutrino energies and interaction types, which speeds up the later stages of production.

This is taken one step further, to calculate the maximum possible cross-section that a neutrino in the energy range could possibly experience whilst passing through the detector. Monte Carlo neutrinos are then propagated through the detector, with a possibility of interaction based on its individual path, re-weighted by the maximum cross-section. The interaction is then generated on a specific nucleus, and that position and nucleus is passed to nd280mc.

Once the final state particles of a neutrino interaction have been selected, they are propagated through the detector by nd280mc. Whenever a particle passes through a sensitive detector region, either the gas envelope of the TPC or scintillator in any other region, this is logged and information about the particle and its energy deposit is stored. The last stage of the MC simulation is then to convert these signals from truth information into a form similar to the output of the detector electronics, all of which is handled by the elecSim package.

The two different detection methods, TPC and scintillator, require different types of simulation. Along the TPC tracks, electron clouds are simulated at rest, based on the ionisation energy lost by the particle. The effect of the electric and magnetic fields is then calculated, making the electrons drift to the MICROMEGAS on the edges of the volume. The charge and arrival time (in 20 time bins of 100ns) is then stored for each pad, as an approximation to the waveform analysis of the AFTER chip (section 2.4.9).

The methods for the scintillator-based detectors vary only slightly, with adjustments for bar size, attenuation length and analysing chip (ASIC for the FGD, Trip-T for the others). The truth hits created by GEANT4 are used to find the location of the hit in the bar and the energy which would have been deposited in the bar. The energy is converted into a number of photons produced by the WLS fibre, after accounting for Birks's quenching effect as described in equation 2.5. An attenuation effect is applied to the photons, based on the distance the G4 hit was from the photosensor and attenuation splines.

These splines are either based on a single attenuation length or calculated from LTRI, a simple MC to estimate the light yield from minimally ionising particles (MIP) at different positions along the bar. A MIP is generally a muon or charged pion, which deposits only a small proportion of its energy in the detector. Electromagnetically showering particles, such as photons and electrons, give a much less even energy deposit; hence the MIP is used as the standard candle for bar response, especially as cosmic muon events will be used for calibration.

Each hit is created as a THit, which stores the charge, time and volume (as a ROOT geometry node ID number). A geometry key may also be set, used to separate between photosensors in double-ended bars or to record which pad of a MICROMEGAS has been hit. These THits are then stored by sub-detector and this information is passed to the reconstruction, exactly as it would be for a real event. All the truth information, particles created, their paths and the hits they contributed to, is still stored, but it is hidden and only used for cross-checks or analysis.

3.3 The ND280 Event Display

Possibly the most useful tool when planning a reconstruction or analysis is the event display. An example of the display can be seen in figure 3.2, which shows a charged current event, originating in the upstream FGD. The information shown is configurable, and this example is only showing one 2D view of the event, but in general the main window is split into four sections. Three are used to show different

orientations of the detector, whilst the fourth shows some information about the vertex, listing the location, incoming and outgoing particles, etc.

The truth tracks of all the particles are visible, a curved green track for the muon, a neutron contained within the FGD and a photon, which has passed from the first FGD to the second. Markers for the hits are seen; the muon leaves a signal in both FGDs, two TPCs and the DsECal. In comparison, the photon leaves no signal in the TPC, and only a small deposit in the second FGD.

The size of the marker matches the physical size of the bar, and the colour of the line represents the charge deposit (ranging from a low energy blue to a high energy red). The time information is not displayed for each hit, but a slider on the control panel allows the selection of a time segment, for example a single integration window of the Trip-T electronics. The truth information overlay can be withdrawn, so that only the information available to a reconstruction is visible, which is useful for hand scanning events.

3.4 Event Reconstruction

The ND280 reconstruction has a modular approach, with each sub-detector doing an initial reconstruction. The results of these independent methods are then combined across sub-detector boundaries using the methods provided by the RECPACK package.

3.4.1 oaRecon, the Global Reconstruction Package

The oaRecon package provides the global reconstruction for the ND280. It provides a single executable to be run, but at this point the majority of the work is done by the other sub-detector packages. Each package provides methods for standalone reconstructions, and oaRecon starts by running these methods. The methods used are explained in the rest of this chapter, but each returns a number of TReconObjects, the most generic form of reconstructed groupings of hits. The specific forms

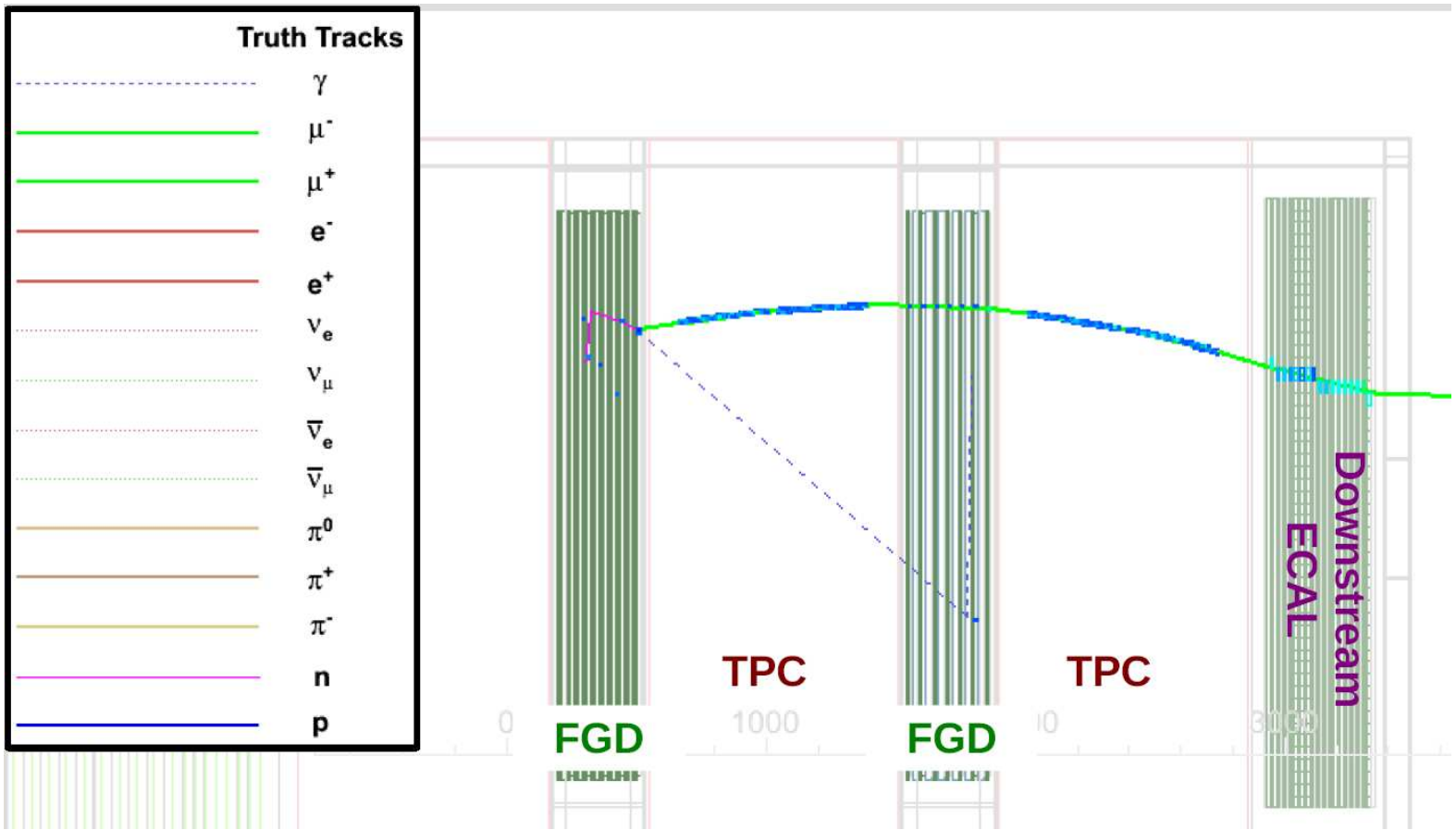

Figure 3.2: An example of the ND280 event display, showing a zoomed-in view of the tracker region. Detector titles have been overlain, and the standard legend is appended, providing the key to the truth tracks. The view shown is from the side, hence the green muon track bending on its path from the FGD to the DsECal. Truth information can be removed, for the purpose of eye scanning events.

of TReconObjects are listed in table 3.1, along with their usage and the ECal reconstruction algorithm in which they are first used.

oaRecon is then responsible for the connection or matching of reconstructed objects from different sub-detectors. At the time of writing, the connection of FGD and TPC objects is working, allowing an early attempt at reconstructing CCQE events. However, this is the easiest possible connection, as both detectors have good resolution and there is only a small probability of a particle being deflected when it crosses a TPC/FGD boundary. In contrast, there is often dead material between an ECal and the inner tracker region, and the change of detector orientation from tracker to ECal adds complications. The work for TPC-ECal and FGD-ECal matching is progressing, and when they are ready a more complete CCQE analysis will be possible, using the ECal to confirm a particle's identification and energy.

3.4.2 p0dRecon

The P0D often acts as a self-contained detector, not requiring as much input from other sub-detectors as the tracker elements. As such, at present p0dRecon is a fully contained process designed for π^0 inclusive measurements, normally CC and NC $1\pi^0$. Still, the methods for connecting P0D tracks to objects in the upstream TPC or P0DECal are being prepared.

The P0D reconstruction has been predominantly written by Trung Le Phouc, a T2K graduate student, and uses a two-step process [64]. Firstly, MIP-like tracks are identified, and the associated hits are removed from the hit sample and the remaining hits are passed to the π^0 reconstruction. To find the MIP tracks, a Hough transform is used [65], which converts all points in an XZ space into curves in $r\theta$ space. When all the curves of a set of co-linear points have been plotted, then there will be a common point for all curves, corresponding to the r and θ of the line.

A weakness in this system is that the location of the hits included in a track is ignored, so the Hough transform is followed by a clustering method, which sets a maximum separation of hits, but also accounts for the structure of the P0D by

Recon Class	Variables	Brief Description	First Used in ecalRecon
TReconCluster	Position, energy, time.	A basic group of hits, which makes no assumptions about object type or direction.	TECALBasicClustering
TReconShower	Start position, energy, time, direction, cone opening angle.	A representation of an energy deposit, starting at a single point and falling inside a cone.	TECALCreateOutputObjects
TReconTrack	Initial position, dE/dx, time, direction, curvature, path width. List of TReconNodes.	A representation of a curvilinear energy deposit, with start and end positions, the path between defined with nodes.	TECALCreateOutputObjects
TReconNode	Position, dE/dx, direction, curvature.	A point along a TReconTrack. In ecalRecon, there is single node per layer.	TECALCreateOutputObjects
TReconPID	Particle Identification (PID) likelihoods.	A TReconCluster, TReconShower or TReconTrack with additional PID information.	TECALCreateOutputObjects
TReconVertex	List of TReconObjects.	A reconstructed vertex, based on a specific reconstruction hypothesis (e.g. CC1π).	Not used in ecalRecon.

Table 3.1: The reconstruction objects included in oaEvent, listed in increasing order of complexity. Descriptions adapted from code documentation [63].

weighting this by the angle against the Z axis. These clusters are then used as the seed for a tracking algorithm, looking in layers in front of and behind the cluster for hits to extend it. The whole process is then repeated, with the first set of tracks removed.

The first step of the π^0 reconstruction is then to find the π^0 vertex. When a charged particle track has been reconstructed, the vertex is simply defined as the beginning of that track or a vertex of multiple charged tracks. In the cases where no charged particle track is found, the vertex is determined by a grid search. The search scans through the whole P0D to find the point which minimises the likelihood function of several likelihood variables:

- The ratio of charge in showers to the total charge.
- The number of showers.
- The angular width of the shower.
- The distance from the vertex to the closest shower.

After the vertex is found, the momentum of the π^0 is approximately reconstructed from

$$\vec{p}_{\pi^0} = k \sum_{hits} \hat{r}_i Q_i \tag{3.1}$$

where k is a calibration constant, $\hat{r}_i$ is the direction vector from the reconstructed vertex and Q_i the individual hit charges. The energy is the total charge, with the same calibration constant k

$$E_{\pi^0} = k \sum_{hits} Q_i \tag{3.2}$$

The invariant mass is then calculated.

$$m_{\pi^0} = \sqrt{E^2 - p^2} \tag{3.3}$$

This reconstruction has been tested on an MC sample of 100k neutrino interactions in the P0D. The π^0 sample was selected based on the following criteria:

- No muon-like tracks or muon decays are recorded, e.g. a 3D track with muon-like particle ID or an unmatched track longer than 40cm.

- 3, 4 or 5 reconstructed 2D showers, allowing for some misreconstruction.
- $80 < m_{\pi^0} < 190$ MeV.
- The reconstructed vertex is within the fiducial volume.

This π^0 reconstruction is found to have an efficiency of about 20%, with the purity at about 45%. The major contaminant to the final π^0 sample comes from CC interactions (about 70%) where the muon track is too short to be detected or hits from muon decay/capture have not been found. Contamination from NC interactions accounts for the remainder, and most are events with at least one π^0, but also other particles which had not been correctly reconstructed (e.g. an extra π^0 or a charged pion).

3.4.3 tpcRecon

Unlike the P0D, the tracker sub-detectors are designed to work together. Each sub-detector does an initial internal reconstruction, producing output objects which range from simple clusters to tracks or showers with advanced particle identification (PID) likelihoods.

As explained in section 2.4.3, the TPC has the best YZ resolution of all the sub-detectors and a low probability of reconstructing a false track from noise. The TPC reconstruction uses the time, t, of a charge deposit as a substitute for the x position, as the two are related by $x = v(t - \Delta t)$, with the drift velocity, v, and an unknown offset, Δt.

The reconstruction starts by clustering hits in XY planes, selecting only hits which are close in time and on adjacent MICROMEGAS pads. The decision to consider XY planes is due to the majority of the interesting particles travelling in the Z direction, but XZ methods are completely equivalent and can also be used.

The tracking algorithm then works on these clusters, creating segments between any two clusters which are within a maximum couple of rows. The cellular automaton then works to connect track segments which share an edge and also pass a cut

criterion, namely that the clusters overlap in space and time. Once a tree of segments has been constructed, the longest possible path is selected and stored as a track. Sometimes a track will branch in the TPC, normally from a hard δ ray, and if this leaves a number of independent segments another small track will be created.

The particle identification methods are based on the dE/dx of the track, the energy lost as a function of distance travelled. The energy lost can be determined from the change in the radius of curvature, and compared against well known values for each particle. The dE/dx is dependent on the momentum, p, as shown in figure 3.3.

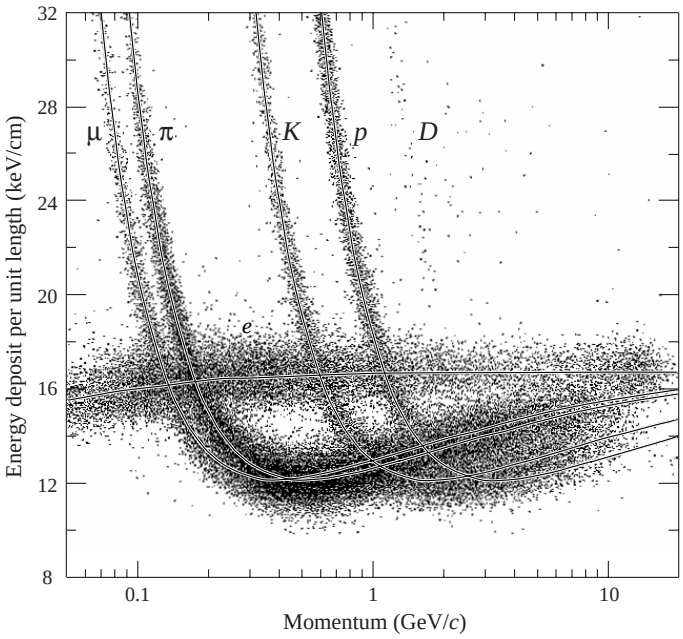

Figure 3.3: The dE/dx of different particles passing through a TPC. The plot covers a large momentum range, and the dependence is similar for most particles (except electrons), but shifted in momentum. This can be a useful identification tool, although some areas of the phase space have significant ambiguity [8].

3.4.4 fgdRecon

The FGD reconstruction follows on directly from tpcRecon, using a Kalman Filter provided by RECPACK to match TPC tracks to FGD hits. The TReconTrack from the TPC stores a series of states as the track progresses. Each state defines the position, direction and curvature of the track, and the state closest to the FGD is

selected, which is then projected into the FGD. The algorithm calculates a χ^2 for each hit, and the track and a simple cut is then applied for the hit to be included in the track. Within each FGD module, at least one hit in each view must be found for the track to be extended.

Once the track hits have been found, RECPACK is used to create an FGD track, which is then connected to the TPC track. It is possible for a particle to pass through multiple sub-detectors, so a high energy muon starting in the upstream FGD may well have a track FGD1 - TPC2 - FGD2 - TPC3.

fgdRecon also has an FGD-only method, called Iso-Recon, which is applied to any hits not clustered by the first method. This is required to find short tracks which do not leave the FGD or tracks which travel roughly perpendicular to the beam and do not pass through the TPC. The first stage is a clustering method, based either on the TPC's cellular automaton method or the P0D's Hough transform. The candidate tracks are then passed through a series of cuts, testing that they are relatively straight, that there is never more than one empty layer between hits and that tracks have not been repeated (ghost tracks). The remaining 2D tracks are matched between the XZ and YZ views, and the resulting XYZ track is stored.

3.4.5 ecalRecon, the ECal Reconstruction Package

The ecalRecon package is designed to work in conjunction with reconstructed objects from fgdRecon and tpcRecon, overseen by the oaRecon package. The connection of objects is handled by RECPACK, so the oaEvent Recon objects have been written to correspond to RECPACK types and have sufficient variables to allow the connection. The long-term plan is for ecalRecon to be a multistage process, with an initial pass doing the majority of the work but allowing the algorithms to be rerun later as part of the global reconstruction, when more information about inputs may be available.

As an example, most EM showers from photons and electrons look identical in the DsECal. They can only be distinguished if the photon is late to convert and leaves no signal in the first couple of layers. However, by looking at tracks coming from the

TPC and matching these to showers in the DsECal, it is possible to see with high efficiency that a shower with a track is an electron and one without is a photon.

However, these later stages of the reconstruction are still being designed by the software group, and are not yet an official part of the code. At the present time, ecalRecon is a single string of steps (see figure 3.4), starting with the THit selection from an event and ending with Track or Shower objects. These categories are normally sufficient for the electrons, muons and photons, and the methods have shown good efficiencies, but charged pions have been seen to be a problem.

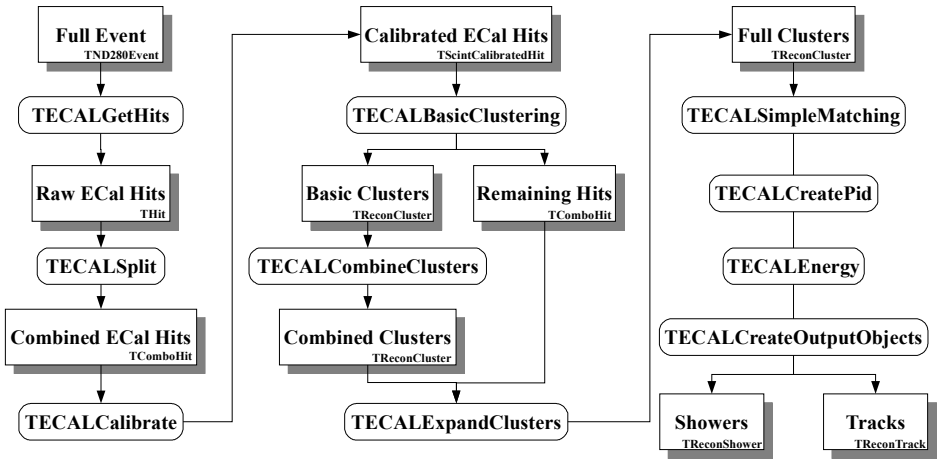

Figure 3.4: The ecalRecon algorithms.

A pion entering the ECal will initially act as a MIP, leaving a simple track, but will eventually form a hadronic shower, similar to the EM shower of an electron or photon. Stylised examples of these interactions are shown in figure 3.5, based on observation of a large number of events in the event display. As can be seen, the standard response for a $\pi^{\pm}$ is to produce a showering track or 'lollipop'.

TECALSplit Due to the possibility of interactions between beam bunches and the relatively slow time response of the TPC, the plan is to start with a full spill as a single 'event' in the software. However, as the ECal has a reset period between each bunch, it is clear which bunch each hit belongs to. Also, the clustering part of the reconstruction works purely in a 2D view and only later are clusters matched between the views.

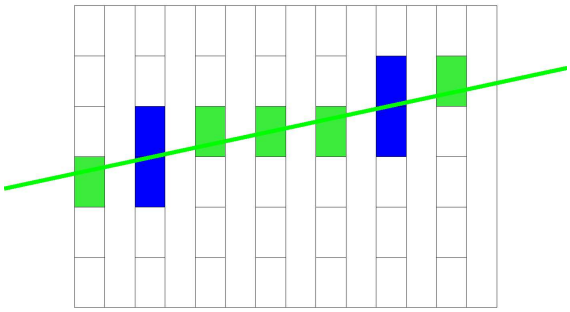

(a) Muon Track

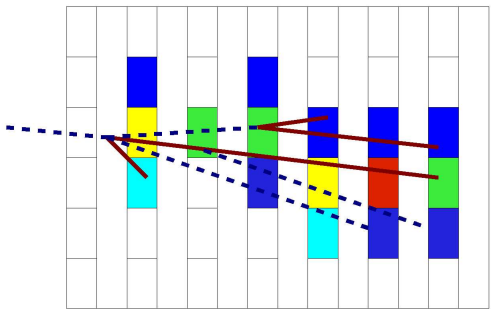

(b) Electromagnetic Shower

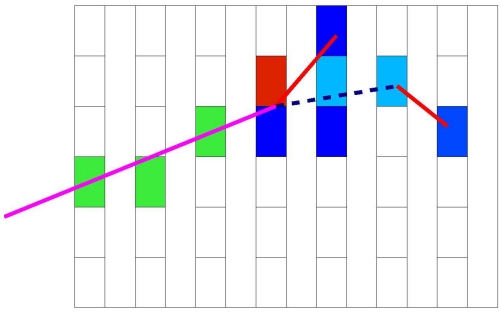

(c) Charged Pion 'Lollipop'

Figure 3.5: Stylised examples of muons, photons and charged pions interacting in the ECal. The figures are based on the eventDisplay style, where the hit colour determines the energy deposited, running from low energy blue through green and yellow to high energy red. The muon in figure (a) leaves a reasonably straight track, and will pass through the whole ECal if it has sufficient energy. The photon in (b) (which leaves the same deposit as an electron) showers almost immediately, producing a cone of hits. The charged pion, (c), leaves a track-like signal to start with, but often finishes as a hadronic shower, which looks similar to a photon shower but has a different energy response.

Therefore, the first stage of the reconstruction is to split the hits into the different time bunches and between individual ECal sections and views. At the same time, a single TComboHit is associated with each bar. For bars with only a single photosensor, the TComboHit is identical to the original THit, but for double-ended bars the information from both ends is combined, with a summed charge and a charge-weighted mean for the time. The clustering algorithms then work on hit bars instead of fired photosensors, which is a more natural approach to reconstruction.

TECALCalibrate The charge of a hit is initially given in photo-electrons: the number of pixels fired on the photosensor by a photon-induced discharge. Just as the elecSim (3.2) package will have produced this number of photo-electrons by taking the initial energy deposit in the bar and simulating each step along the way, TECALCalibrate will work to reverse these effects, providing a charge in terms of MIPs.

A MIP unit is defined as the number of scintillation photons created by a minimum ionising particle, such as a muon, travelling a distance of 1 cm through scintillator. When the detector has been installed, muons from cosmic rays or the beam will be plentiful enough to allow constant calibration of the detector. The attenuation parameters and photosensor response for each bar will be continually monitored and stored, and these variables will be used to calibrate real hits.

The first stage of the algorithm is to create a new object from the TComboHit. A TScintCalibratedHit inherits from the TComboHit class, but stores additional variables necessary to create a calibration hypothesis, such as a second position vector to contain the hypothesised position along the bar, the estimated number of photons incident on the photosensors, the corresponding number of MIPs and a bitwise status integer for recording the progression of the calibration.

The first stage of the calibration is within the photosensors, converting back from photo-electrons to photons incident upon the sensor. This depends on the

photon detection efficiency (PDE) of the device and the statistical probability of multiple photons falling on the same pixel and producing no extra signal. The statistical effect introduces an error into the calibration, but the effect is minimal for a small number of photons.

The attenuation can have a more drastic effect, as the distance travelled by the light is initially unknown. For a bar with double-ended readout, the position along the bar is estimated based on the relative strengths of the two signals, but for a single-ended bar the initial assumption must be that the deposit was in the centre of the bar. For a MIP passing through the hypothesised position, a number of photons reaching the photosensors is estimated, allowing a conversion from $N_{Photons}$ to MIPs (figure 3.6).

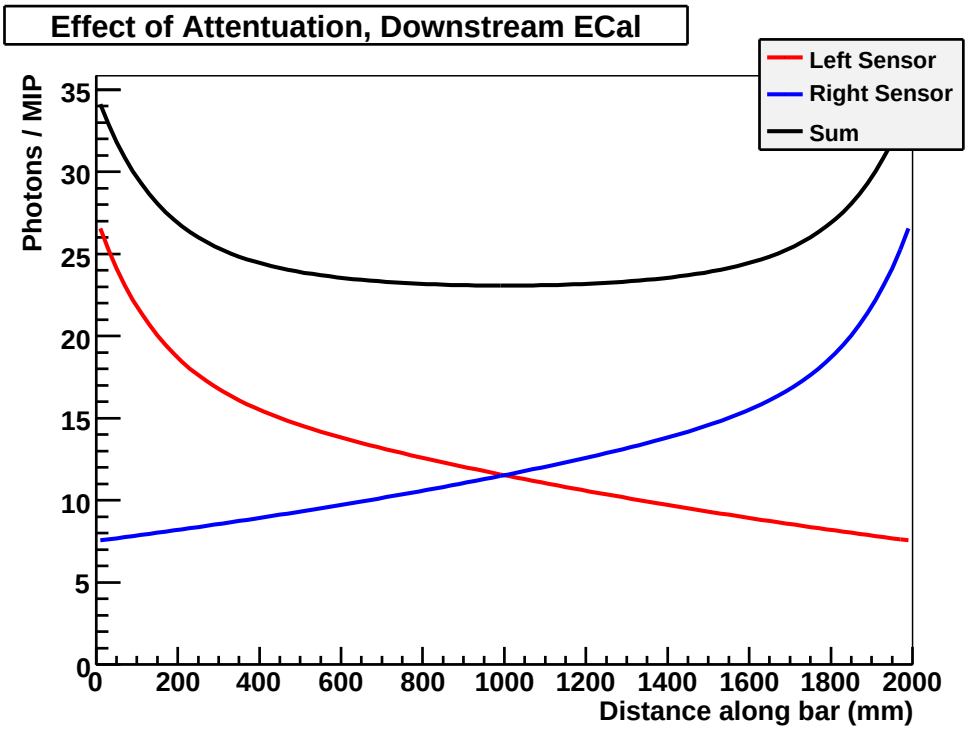

Figure 3.6: The attenuation in the DsECal. As each bar has a photosensor at both ends, the response is good for the full length of the bar. The response of the barrel ECals will be worse, due to some bars being longer and others having only a single photosensor.

TECALBasicClustering Once a group of TScintCalibratedHits has been prepared, the clustering can begin, with a simple aggregation clustering algorithm as the first process. The algorithm takes the nearest neighbour in the 'width'

or X direction and next-to-nearest neighbour in the 'depth' or Z direction, with a 3 hit minimum.

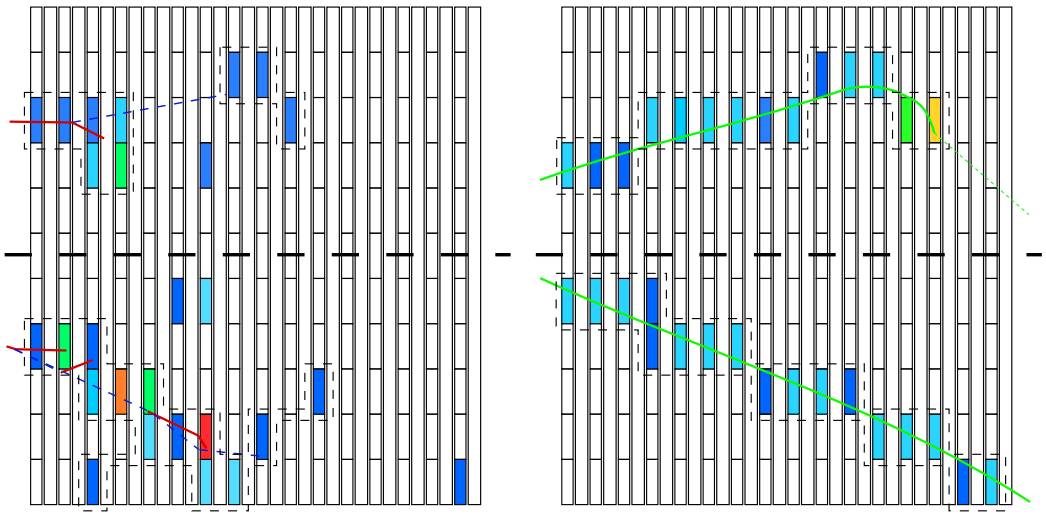

(a) Shower events (b) Track events

Figure 3.7: A cartoon of basic clustering applied to some generalised events. Four events are shown: (a) shows two EM showers while (b) shows two muons. In each, the top particle is an example of 150 - 200 MeV and almost direct incidence on the ECal front face. The lower particles are at higher energies (300 - 400 MeV) and angles. Truth tracks for electrons, photons and muons are also shown, using the event display scheme shown in figure 3.2.

The 4 cm width of the ECal bars was decided based on the Molière radius of an electromagnetic shower in scintillator and lead, so the main body does not tend to have horizontal gaps. Once the photosensor and bar response is better understood, a noise cut will be applied to ECal hits, which may necessitate changes in the clustering algorithm.

However, for single MIPs, the charge deposit depends on the distance of bar travelled through, so in some layers the MIP will only leave small deposits in two adjacent bars. If a nearest-neighbour-only method was applied in the depth direction, then this would lead to a number of separated clusters, some of which would fail the 3 hit minimum. Any hits which are not saved in clusters are individually stored, to be used during a later process.

TECALCombineClusters The problem of a shower or track being split into a number of basic clusters, due to vagaries in the charge deposit of hits, is significant. The rules and cuts of basic clustering have been tuned to minimise

the problem, but cannot be loosened too much, else the purity would drop significantly.

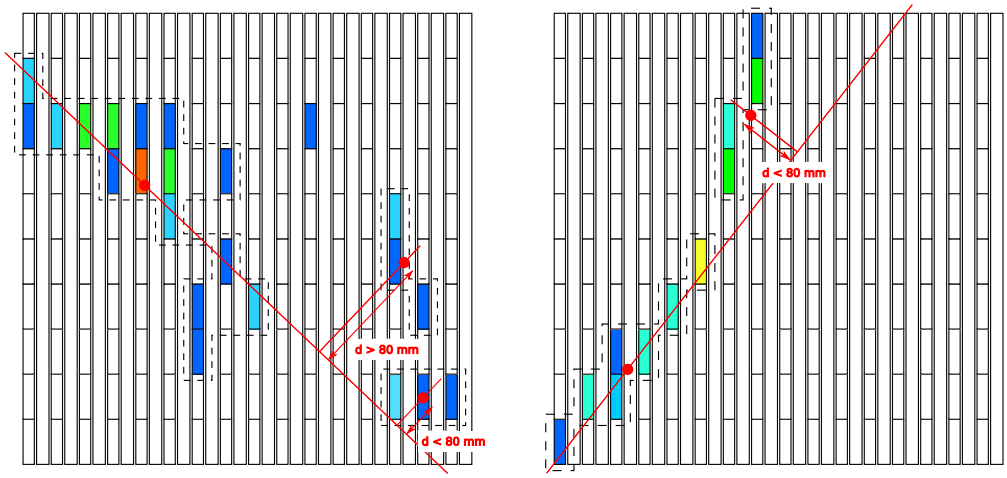

(a) Shower events (b) Track events

Figure 3.8: An example of the combine clusters algorithm, deliberately selected to show the potential problems of the method. The electron event shows that a cone approximation would be an improvement, with one cluster being lost. The muon event was completely successful, but a fitted curved track would obviously be more effective. The effectiveness of the method is discussed in detail in section 4.2.

The next stage is therefore to attempt to connect these clusters, based on assumptions about the direction of the dominant cluster. Specifically, the largest cluster in the group is selected and a direction is calculated based on a principal component analysis (PCA). This direction is then extrapolated both forwards and backwards and checked against other clusters, to determine how closely the position matches and how well they are correlated in time.

It was originally hoped that the direction of the different parts could also be considered, as this is effective for split tracks. However, the PCA pointing method can fail for smaller clusters, especially when they are an offshoot part of a shower. In fact, for a shower it would be better to assume that the cluster is the start of a cone and that any clusters which fall further into the cone and in the correct time bin should be added. However, these initial assumptions (shower vs track, that the forward direction is known or that hits are not caused by another source) can lead to misreconstructions.

As such, this is another example of a situation where the latter stages of a global reconstruction will be able to work with much greater efficiency; e.g. when an incoming track from the TPC has already been attached to the first basic cluster. In a seeded cluster method such as this, the initial shape of the object in the ECal, coupled with PID information from the FGD or TPC, provides sufficient information about the particle type and direction for a more accurate reconstruction to be possible. As previously mentioned, this global reconstruction work is still under development.

TECALExpandClusters Once the clusters have been combined, there is still a list of hits which were not included in clusters by the BasicClustering algorithm. As can be seen in the examples, these hits do not always contribute useful information to the reconstruction. For a muon which produces a hard δ ray that leaves a couple of hits adjacent to the track, the inclusion of these hits would only serve to confuse the algorithm used to fit the direction of the track at each point.

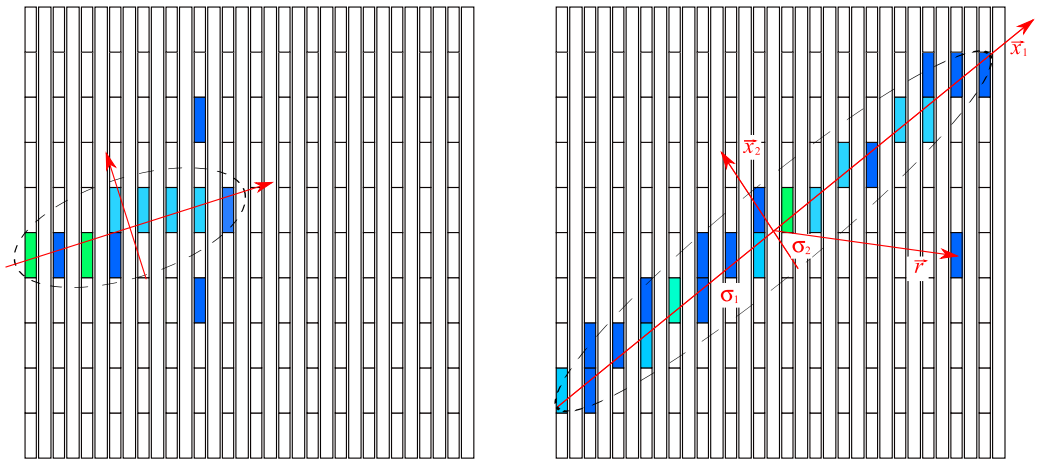

(a) Shower events (b) Track events

Figure 3.9: Two examples of the expand clusters algorithm. Each hit is evaluated using equation 3.4, against all possible parent clusters. Both excess hits in the shower event will pass the weight cut and would be added to the cluster. The extra hit in the track event is caused by the muon, but its inclusion adds no useful information to the reconstruction. Only hits which usefully extend the track are wanted, so the hit shown will not pass the cuts.

However, for electromagnetic showers, the inclusion of these hits can have a drastic effect on the energy reconstruction (the energy fitter is described later

in this section). Therefore, the PCA method is used again, to define tracks or showers as an ellipse in space and time, with the direction and size coming from the eigenvectors and eigenvalues of the PCA method respectively. Each unclustered hit is then evaluated as a possible member of each cluster, using the requirement that the hit must be within 20 ns of another hit in the cluster and then producing a weighting, W, based on the equation

$$W = \sqrt{\left(\frac{\vec{r}\cdot\vec{x}_1}{\sigma_1^2}\right)^2 + \left(\frac{\vec{r}\cdot\vec{x}_2}{\sigma_2^2}\right)^2} \tag{3.4}$$

where $\vec{r}$ is the position of the hit relative to the centre of the cluster and $\vec{x}_{1,2}$ and $\sigma_{1,2}$ are the eigenvector and width for the primary and secondary components. The hit is added to the cluster with which it has the smallest weighting, and a maximum cut-off is applied, to limit the addition of other hits.

The final value for the cut-off will depend heavily on the noise rate of the photosensors and the rate of other interactions in the ECal. Specifically, when a full spill is considered, neutrino interactions in the magnet yokes are plentiful, although most particles will be ranged out by the iron, but neutrons may interact anywhere in the detector, creating small energy deposits.

The output from TECALExpandClusters is a list of 2D clusters, but the attenuation of the bars has an important effect on the charge deposit in the photosensors. This effect can be corrected for by knowing the full 3D location of each hit, so it is important to create 3D clusters before the PID or energy reconstruction stages.

TECALSimpleMatching The matching code has changed a number of times over the last year, and the version that was included with the June release was untuned, erring on the side of inclusiveness so that analysis of low background events would be possible. However, the variables calculated and considered have changed little, only the cut-off values used. The point is to find variables which should be similar for two views of the same particle but would differ for objects caused by two different particles.

Three of the variables used are based on the cluster position with respect to the layers (the axis perpendicular to the ECal layers is referred to as the local Z axis). These variables are the front of the cluster, the back, and the charge-weighted centre.

At this early stage, it is assumed that a particle has entered the ECal from the tracker (as opposed to from outside), therefore in each view the first layer with a hit should be similar. As mentioned earlier, there is a possibility of one layer being missed for a number of reasons, including clustering errors, but this is unlikely to repeat for more than a single layer, except in specific geometrical situations.

The back layer is more likely to differ, especially in showers where small deposits of only one or two hits have been added by the 'expand' algorithm, further back than the main body of the shower. This is a genuine effect caused by photons travelling for a short distance, converting and leaving deposits, but having insufficient energy to cross to another layer. Therefore, the back cut should be weaker for shower-like objects (for MIP tracks, especially muons, it is normal that there be at least 1 hit in each layer of the ECal as the particle passes all the way through).

Finally, the charge-weighted centre of the cluster is used, as for EM showers this will be near to the major deposit. However, this presents a problem; the charge is affected by the attenuation, but this cannot be accounted for until the clusters have been matched, at which point the attenuation is no longer required. As an example, if a shower is roughly perpendicular in one view but heavily slanted in the other, then in the first view the effect of attenuation is constant and the charge-weighted sum is reasonable. In the second view, the attenuation may change significantly from front to back, decreasing the charge deposit at one end and increasing it at the other, shifting the 'middle'.

Another variable effected is the ratio of the charge deposit in the two views. Statistical fluctuations will change how much energy is actually lost in the bars, but the two sums should be similar.

Therefore, the matching code assumes that two clusters are a pair, before calculating the required variables. When the 3D cluster is hypothesised, for each layer in the XZ view, all the hits in adjacent YZ layers are taken, and produce a mean Y position, which is assigned to the XZ hits. Once this position along the bar is given, the TScintCalibratedHit recalculates the photons produced by a MIP at the new position, and reweights the number of measured photons to produce a new charge value, in terms of MIPs.

The advantage of reweighting the charge with respect to the MIP figure is that it will be a physical calibration constant. As the electronics simulation or MC geometry are adapted to better match the reality of the detector, it is possible to recalculate the MIP value. Any step of the reconstruction after the calibration stage should then be unaffected by the changes, and the internal reconstruction variables and distributions would not need to be adjusted or reproduced.

In the real running of the detector, instead of tracking the changes in MC, the electronics will run in cosmic mode outside of beam spills. A constant calibration can be maintained for each bar and photosensor, and this can be applied to the data, again returning hits in terms of MIPs, a known quantity.

The present version of the matching code applies a cut on each variable, and failing a single cut is sufficient to disqualify a pairing. A more advanced version of the matching has been produced, but is also not yet tuned, which aims to provide a weight to each variable, create a likelihood for each pairing and select the combination of pairings with the highest value. The method, called FullMatching, is very similar to that used for the PID.

TECALCreatePid After the cluster matching has been performed, an initial PID can be run on the clusters, using the ten variables listed in table 3.2. Some of the variables used only work in 2D situations, so the algorithm considers the two independent halves, but uses the more accurate MIP units for charge. The aim at this point is to categorise reconstructed objects, not to identify specific particles, as this can be done with greater confidence when information from other sub-detectors is included.

For example, the ECal has little ability to distinguish between electrons and photons, as once the shower has started the signals are identical. The only real distinguishing factor is the distance into the ECal where the first layer occurred – if there are 3 empty layers before a shower then it is impossible for this to be an electron entering from outside the ECal.

However, the detector is not all active material, as each sub-detector needs electronics, cooling, support structures, etc. This dead material will often be encountered by a photon before it reaches the ECal, triggering the shower early and removing the ability to distinguish between the two particle types. In contrast, the signal for the two particles in a TPC could not be more different; an electron will leave a track, curved by the magnetic field, and will give an indication of the momentum of the particle whereas a photon will normally pass through the relatively low density gas without interacting, hence leaving no ionised gas and no track. By comparing the signals between the ECal and TPC, a photon/electron decision can be made.

Instead of doing a full PID, the ECal PID is designed to identify three types of particle interaction: tracks, showers and showering tracks (or 'lollipops'). It is only possible to calculate a likelihood for each object, rather than a definite answer, but in most situations it is done with a high degree of accuracy. For lower energy particles where only a handful of hits are created, it becomes more difficult to distinguish between a small shower or a very short stopping track. Also, the lollipop can be problematic; firstly the dual nature of the object must be identified and then the change-over point must be selected. Getting this correct is important, as it will have a large effect on the energy reconstruction.

When a particle has a reasonable amount of energy (above $\sim$150 MeV), then separating tracks from showers becomes simpler. A MIP track will leave only one or two hits per layer, closely matching a straight or curved line (depending on view and momentum) and PCA will produce a marked difference between the first and second eigenvalues.

Variable	Range (# of Bins)	Description
AMR	0 – 300 (300)	The ratio of the 1st and 2nd eigenvalues of a PCA applied to the cluster.
Length	0.5 – 35.5 (35)	The depth of the cluster in units of layers.
Width	0.5 – 20.5 (20)	The width of the cluster in units of bar width.
NumHits	0.5 – 100.5 (100)	Number of TComboHits in the cluster.
ChargeRatio	0 – 60 (100)	The maximum ratio of charge in the front half and the back half of the ECal.
MeanCharge	0 – 300 (100)	The mean of the hit charge, for the hits between the 10th and 20th percentiles, ordered by charge.
MaxRatio	0 – 500 (100)	The ratio of the layer with the greatest and least charge deposit.
MinWidth	0 – 12 (12)	The minimum width of the cluster in a layer, in units of bar width.
ChargeSD	0 – 80 (40)	The standard deviation of the charge of the TComboHits.
WidthDiff	0 – 12 (12)	The difference between the minimum and maximum widths of the cluster.

Table 3.2: The variables used in the ECal PID. Nine probability functions (angular bins of 10°) are produced for each variable and hypothesis, with the ranges shown. The variables are then calculated for a cluster, and a likelihood is determined for each possible hypothesis. An example distribution can be seen in figure 3.10

The ratio of these numbers, called Axis Max Ratio or AMR, is used frequently in the ECal, as it gives a good indication of the shape of the object in a single number. The charge distribution in a track is also interesting; the charge deposited per layer is relatively constant (although not necessarily exactly 1 MIP, as the angle will affect the light produced), giving a low mean charge per layer and a small standard deviation of the charges. In contrast, a shower gives a shorter, wider object (lower AMR) and a large variation in layer charge, especially when comparing the front and back halves of the ECal.

To calculate the likelihood numbers, a number of probability density functions (PDFs) are produced for each hypothesis. This is done by taking a large MC sample of each cluster type, varying over energy and angle, and calculating each desired variable and storing them in a histogram.

Then, when a cluster must be classified, the same variables are calculated.

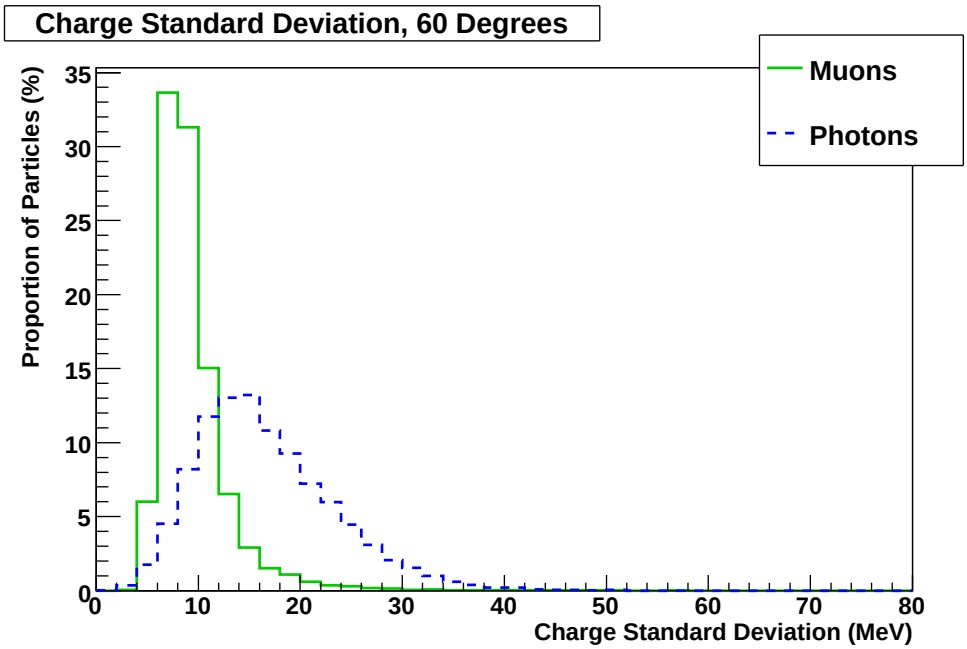

Figure 3.10: An example of a PDF for the PID in the ECal. This specific PDF shows the standard deviation of muon and photon clusters, displaying the relative likelihoods for both particles.

The angle of the cluster is also approximated, as many of the variables vary drastically with angle. These variables are then compared to the histograms of the hypothesis and the relative weight of the selected bin is used to produce the likelihood.

The variables also change drastically with the momentum of the incoming particle, but the ECal cannot determine this without knowing the particle type. However, once an ECal object has been connected to a TPC track, the momentum of the particle will be available from the TPC, and the PID can be revisited to look at more detailed PDFs split by both angle and momentum.

TECALEnergy The clusters have now been classified as showers, tracks or lollipops. The energy reconstruction method is highly dependent on this decision. For the track-like regions, the summed energy deposit is the only information available. The energy of muons can only really be determined by ranging them out with a large number of absorber layers. In the SMRD this will be possible because of the large amount of iron in the magnet, but to include sufficient material in the ECal would be impossible due to size and weight constraints

(the crane used to install each ECal modules is rated to 10 t). Therefore, only the lower energy muons (∼150 – 250 MeV, depending on angle) will be stopped by the ECal; for higher energy particles it will be necessary to use the momentum measurement in the TPC instead.

In contrast, an electromagnetic shower can provide enough information to reconstruct an accurate energy. This is possible due to a number of reasons, the major two being the predictable nature of an EM shower and the design of the ECal, with bar sizes and lead thicknesses tuned to enable EM reconstruction.

Hadronic showers are more difficult to reconstruct, but an attempt can be made. The form of a hadronic shower is dependent on the parent particle and a relatively large amount of the energy is lost as neutrons. In hadronic calorimeters, the design would include a mechanism for capturing neutrons and including their energy in the reconstruction, but attempting to include such items in an ECal would deteriorate the response for EM showers, which are more important to the reconstructions required of the ND280.

Therefore, the PID algorithm is used to determine which algorithms should be applied to which parts of an object; the method for MIPs has been explained above and hadronic showers are reconstructed with a similar method to EM showers (with variables based on charged pions). Lollipops are first separated into the constituent track and hadronic shower, and then the two methods are independently applied.

For an EM shower, a fitting method is used, with variables similar to those used in the PID. The variables used are listed in table 3.3. A large training sample of photons with a range of energies are fired into the ECal using the MC; the variables are calculated for each, then the mean, sigma and skew of each is fitted to a polynomial function.

Photons are used for the training sample because they are less likely to interact before entering the ECal than electrons. Due to the dead material in front of the ECal, a significant fraction of an electron's energy can be lost before the sensitive material is reached.

Fit Variable	Description
QSum	The total energy deposit collected, in MIP units.
QMean	The mean energy deposit i.e. QSum / Number of Hits.
QRMS	The RMS of the energy deposit distribution.
QSkew	The skew of the energy deposit distribution.
QMax	The MIP charge in the bar with the maximum deposit.
XWid	The width of the shower, calculated as the mean of the RMS of each layer.
QXWid	Like XWid, but with the mean weighted by the summed charge of the layer.

Table 3.3: The energy fitter for EM showers uses a number of variables, listed above. The variables fall into two main categories, charge-based and shape-based, which are above and below the separating line respectively. Descriptions adapted from code documentation [63].

The order of the polynomial function is changed as necessary to achieve a good fit, although in future it may be an improvement to use splines to determine the shape, a series of polynomials connected together. The polynomials define a Gaussian distribution for each variable, changing with the hypothesised energy.

Therefore, when a set of variables is input from an unknown cluster, the energy can be varied to minimise the fit of each variable to the Gaussian produced, and this minimised energy is the returned value.

For lollipops, the second half of the object will have a similar method applied, after the conversion point, using charged pions for the training sample. The energy reconstruction will have significantly decreased accuracy compared to the EM shower, but this is not a major problem as the pion will likely leave a TPC track, allowing for an accurate measurement of the momentum.

TECALCreateOutputObjects Once the 3D deposit has been identified, the TReconClusters used throughout are converted into more advanced reconstruction formats. These objects were designed alongside the RECPACK package, so that they deliberately contain all the information required for matching between sub-detectors. There are a series of objects, each designed to fulfil a specific need in the reconstruction order. These were shown in table 3.1, which also explained the assumed shape and the information required. In general, every variable that is stored will have a variance and also co-variances with the others, as the reconstruction method often leads to systematics.

At the first stage, ecalRecon creates TReconShowers or TReconTracks. For clusters identified as tracks or showers, just a single object is required, but for the showering tracks both objects are constructed, a track from the front portion of the cluster and a shower from the back portion. The shower object is then appended to the track object as a final node, and the track object is stored, to be passed to the global reconstruction.

The code assumes that a track enters from the inner face and can be characterised by a start point, and a node for each layer with hits. The hits in each layer will have been given a 3D position earlier in the reconstruction, but a direction and curvature is also required at each point. As such, the hits in each layer are converted into a 3D point. For each point, a minimising function is applied to it and the four nearest points (usually the two before and two after). This straight line fit is then used to assign position and direction for the point, and this becomes the node. Normally it is expected for a node to have a curvature, but the large amount of matter in the ECal increases the probability of scattering drastically, and a simply curved track cannot be assumed. Instead, the curvature is set to zero with a large variance.

In this respect, the present reconstruction is heavily biased, as it assumes that the object is coming from the inner detector region and that it will be passing through the layers. In the fullness of time, it will be necessary to consider other possibilities, such as tracks originating within the ECal and/or travelling parallel to layers. These are both interesting scenarios; for instance if events starting in the barrel ECal are included, then a wide range of off-axis angles can be studied. This provides information about the beam, and allows for tuning or validation of the beam Monte Carlo, giving an improved understanding of the systematic effects in the near-far ratio.

A shower is also assumed to have come from the basket direction, and the hits are evaluated as a cone, with a starting point, direction and angle. This is a better approximation to the shower shape than the ellipse assumed by a standard PCA, but if the starting point of the shower is incorrect then large errors are introduced. A fuller method is to determine the direction of the

shower using the front/back asymmetry, and then to use an adapted PCA method, called a thrust analysis, which uses the front of the shower instead of the charge-weighted centre as a focus.

3.5 ND280 Analysis

By the end of the reconstruction, a lot of information has been created from the simple start point of a neutrino interaction from NUANCE, NEUT or GENIE. Even in its most verbose form, data from GENIE and NEUT averages out at 1 – 2 kB per interaction. In contrast, the results of Mock Data Challenge 0 (MDC0, a test of the full MC production chain with large numbers of events) showed that after the reconstruction an event was over 70 kB in size.

This makes an event file of only 10,000 events significantly larger than many users would wish to store locally (usually the preferred option for an analysis). Therefore, the oaAnalysis package was created, to distill the reconstruction information into a more usable form (7 kB). The full details of each hit, including the MC truth which caused it, is no longer stored, but instead each TReconObject is reduced to its internal variables; position, energy deposit, series of nodes, etc. In the fullness of time, the analysis file will hold a series of TReconVertices, each one with a number of TReconPIDs containing a string of TReconTracks and TReconShowers. A vertex would be based on a specific hypothesis for an event, e.g. CCQE or NCπ^0, and would provide the reconstructed values for that hypothesis, e.g. interaction location, energy of all the initial particles and energy of the incoming neutrino.

As the file would also hold the truth of each vertex, your average user with no greater understanding of the software than a knowledge of ROOT would be capable of running an analysis, tweaking the goodness of fit until they had a purity and efficiency they were happy with. As each TReconObject would be stored, the same user could rerun parts of the reconstruction with their own cuts and methods, combining objects from a number of different reconstruction methods, in an attempt to improve the efficiency or purity of the measurement.

The best combinations for each analysis are then stored as Python scripts, defining which modules to use, how to combine them and which cuts to apply to the outputs. This script of only 200 – 300 lines can then be applied to every data file, whether MC or real data, and will create a small ROOT file, containing only enough information to produce the histograms of the analysis. For example, the current CCQE analysis stores the reconstructed neutrino energy, the angle the muon was produced at and the reconstructed momentum of the muon, for any event which has passed a series of cuts.

With MC data, this can be compared to truth information to study efficiency and purity for a range of energies and angles. The real data can then be compared to the MC, with the matching of several histograms used to determine the success or failure of the MC and the overall outcome being the first step to producing an event rate for CCQE muon events.

Chapter 4

A Monte Carlo-Based Validation of the ECal Reconstruction

This chapter will show the efficiency of the ECal reconstruction methods described in detail in the previous chapter (section 3.4.5). As the detector is still in the construction phase and the testbeam of the DsECal will not be until mid 2009, the efficiency studies are all Monte Carlo-based.

The efficiencies are shown to be highly dependent on energy, with very low energy particles very difficult to reconstruct. Approximately 95% of photons and muons with less than 50 MeV kinetic energy are missed, which is shown to be due to a low number of hits being produced. The reconstruction efficiency for both particle types increases rapidly with kinetic energy; above 150 MeV the proportion of correctly reconstructed muons jumps to more than 95%, with electrons lagging behind slightly at 85%.

The cluster positions are reconstructed with very good resolution, to the order of 25 mm in comparison to the 40 mm width of the ECal bars. The cluster direction is dependent on energy and particle type, with MIP-like tracks and higher energy particles showing better resolutions. With the exception of some geometric effects and sign errors, the angle of incidence has little effect on the error of the reconstruction, which has an RMS of 10° or better for muons over 400 MeV and 16° for photons

of similar energy. The methods for estimating cluster directions are being worked on by another T2K student, Pawel Guzowski, and these resolutions will certainly improve before the ECal is installed in late 2009.

The lack of real data to test the algorithms was the motivation for adapting ecalRecon and other ND280 methods to work on data from the SciBar detector. The methods used are explained in detail in section 5.3, and the results are shown in chapter 6.

4.1 Monte Carlo Production

The Monte Carlo, which was explained in chapter 3, is capable of approximating a full spill of the T2K beam, with interactions in the hall, magnet and all sub-detectors. The reconstruction is also advanced enough to work on this full spill simulation, but those results would be overly complicated for the task of studying the efficiency of the ECal clustering algorithms.

4.1.1 Particle Gun Files

Instead, something similar to a testbeam is simulated; the first set of Monte Carlo produced consists of very simple particle gun samples, starting a short distance from the face of the DsECal, for a range of energies, incidence angles and particle types. These three variables have the largest effects on the reconstruction, as will be seen in the rest of the chapter.

Three particle types were studied, electrons, photons and muons. The muon was selected as the most MIP-like particle, although at lower energies this description becomes increasingly inaccurate. The muon is also the most likely MIP to be incident on the ECal, as charged pions are rarer and the proton is normally ranged out in the FGD target.

The electrons and photons are two representatives of the electromagnetic shower class; positrons incident on the ECal will be rare in neutrino running so are ignored.

Particle Type		K.E. (MeV)		Angle (Degrees)
		0 – 50		
		50 – 100		
		100 – 150		0 – 15
Photon		150 – 200		15 – 30
Muon	×	200 – 250	×	30 – 45
Electron		250 – 300		45 – 60
		300 – 400		60 – 75
		400 – 500		
		500 – 750		
		750 – 1000		

Table 4.1: The particle types and energy and angle ranges used to produce the particle gun files. The second column refers to the kinetic energy, which can be lost to the ECal, and does not include the rest mass of the particle. The third column shows θ, with respect to the Z axis, which is perpendicular to the DsECal's front face. 2,500 events are generated for each combination of variables, giving 375,000 events in total.

Whilst both electrons and photons were studied, it was found that there was little difference between the response of the two particles. The primary cause of any differences was the different starting points of the showers. Electrons would lose energy in the dead material in front of the ECal, whereas the photon was likely to start showering in the first couple of layers instead. This has an important effect on the energy reconstruction of electron showers, which can be compensated for after the testbeam, but for the detection and reconstruction of showers the difference is minimal. Still, the figures in this chapter are for photons and muons, as these provided the cleanest samples which most accurately matched the physics scenarios being considered.

The expected energy range of particles depends on a number of variables. For example, a photon incident on the ECal is likely to be caused by either bremsstrahlung of an electron or the decay of a π^0. For the π^0 case, the energy of the two photons varies depending on the initial energy of the π^0 and the decay axis relative to the momentum vector. Trying to determine the exact energy spectrum is possible only through a large Monte Carlo analysis, and quite unnecessary for looking at efficiencies. Instead, particles are produced with uniform distributions, and the energy ranges and numbers produced are shown in table 4.1.

Similarly, particles are produced in cones about a vector perpendicular to the front face of the ECal, again listed in table 4.1. The angle θ is measured against the Z axis of the detector, and therefore equates to the angle of incidence upon the front face of the DsECal. As any angle selected within the cone is valid, the angular effects observed by the ECal can change. A particle with $\theta = 15°$ may fall perpendicular in one view but at 15° in the other, or at 10° in both views. Both situations will have effects on the clustering or matching algorithms, so the full event must be considered, and not just the success of the algorithms in one 2D view. Even then, the varying angle may have an effect on the 2D to 3D matching algorithms, but that work is beyond the scope of this document.

2,500 events were generated for each combination, so with ten energy ranges, five angular ranges and three particle types, the full sample is 150 files or 375,000 events. However, not all of these events will be useful. So that the correct response of the ECal can be understood, the source of each particle is a randomly selected point on a square, 2×2 m^2, directly in front of the DsECal. This ensures that the effect of the attenuation length is observed even for the 0° sample, but it does mean that some of the particles produced at higher angles will completely miss the DsECal.

As such, an acceptance cut is applied to the data, requiring that the initial trajectory of the particle takes it through two squares, 1840×1840 mm^2, at $z = 2938$ mm and $z = 3000$ mm, roughly corresponding to the first and fourth layers of the DsECal. This cut ensures that the particle would have left sufficient hits to form a cluster, if all other considerations were ignored, and the effect can be seen in figure 4.1.

4.1.2 Adding a Full Bunch Background

Defining efficiency for the clustering algorithms is relatively simple. In a perfect case, a single particle enters the ECal and produces a single cluster in each view, with all the hits included in the cluster. The next section will investigate this as a definition of success and consider which alternative outcomes would still be acceptable.

However, purity is a more difficult consideration. There are a number of ways that physics events could be misreconstructed, but many of them still produce useful

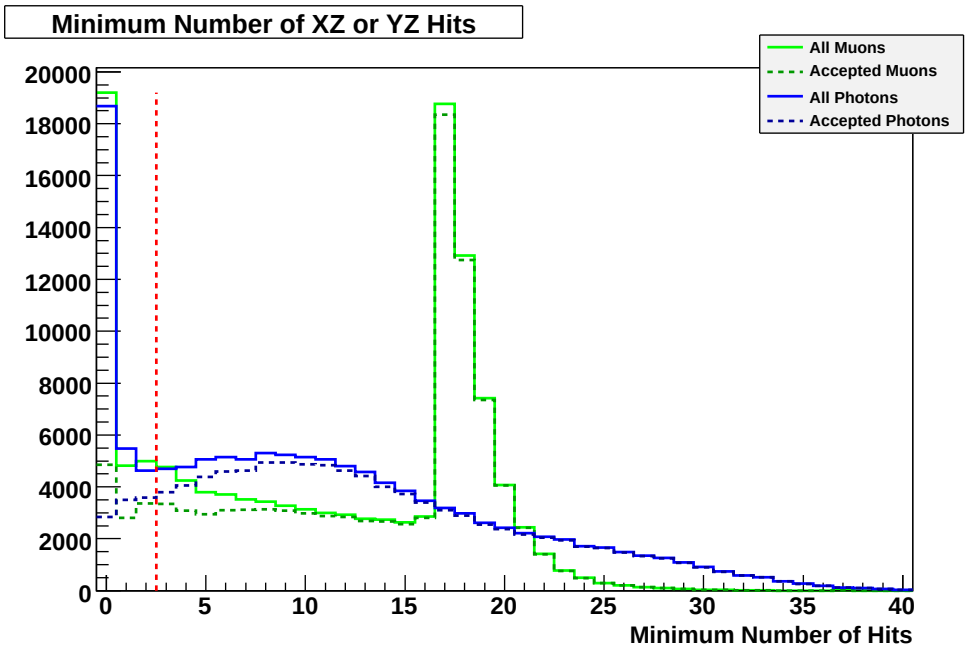

Figure 4.1: The plot shows the minimum number of hits within one 2D view for each event. Muons are marked in green and photons in blue, will solid lines for the full event sample and dashed for those that passed the cut. The vertical red line shows the 3 hit minimum required for the clustering algorithms.

output. Consider an electron travelling from the downstream TPC into the DsECal. There is a chance that the electron will produce a bremsstrahlung photon, travelling in the same direction as the electron. If they both interact with the ECal at the same point, and are reconstructed into the same shower, then the fitted energy will match the true energy well enough for the reconstruction to be a success. However, the magnetic field will bend the path of the electron, so that in the YZ view of the ECal the showers might be separated, but in the XZ they would still overlap. This situation can be recovered in the fullness of time, but for an analysis focusing purely on the clustering and its effects, it is difficult to determine which situations should be considered failures.

Another likely situation is trying to reconstruct one specific particle against a background of other particles. This is a requirement in the ND280 software, due to the expectation of multiple interactions in each bunch. If a given NC π^0 interaction in the fiducial region of an FGD is considered, then in the same bunch there will be many more neutrino interactions in the basket, ECals, magnet and walls of the ND280 pit. For the ECal, the effect of cavern events is small, and these would likely

range out in the magnet or P0D before reaching the ECal. However, the other events can all produce hits in the detector which complicate the ECal reconstruction of a specific particle.

To investigate the effect of the extra interactions, the previous particle gun method is expanded. The same particles and distributions are used for the particle gun, introducing the target particle. Then, within the same event, other neutrino interactions are simulated, generated by NUANCE from the T2K flux. These are distributed by weight throughout the entire detector mass; the number of interactions is sampled from a Poisson distribution with a mean of 7 events. (The flux expected when T2K reaches full power predicts 8 events per beam bunch, one of which is set aside for the specifically introduced particle).

The majority of the following plots are produced with the simple particle gun method. The full background method is only used when directly relevant, and will be specifically mentioned.

4.2 Clustering Efficiency and Purity

As mentioned in the previous chapter, the ECal reconstruction has been written as a series of independent algorithms, with one algorithm operating on the result of the previous. Therefore, the effectiveness of each algorithm step is considered, before determining the final efficiency of the detector.

4.2.1 Cluster Finding Efficiency

The 'basic clustering' method was not designed to fully reconstruct a shower or track, but instead to create a seed for the further clustering methods. The optimum scenario is for there to be one seed in each view; however the 'combine clusters' method will reconnect multiple clusters, therefore any number of clusters greater than one can be considered a successful outcome.

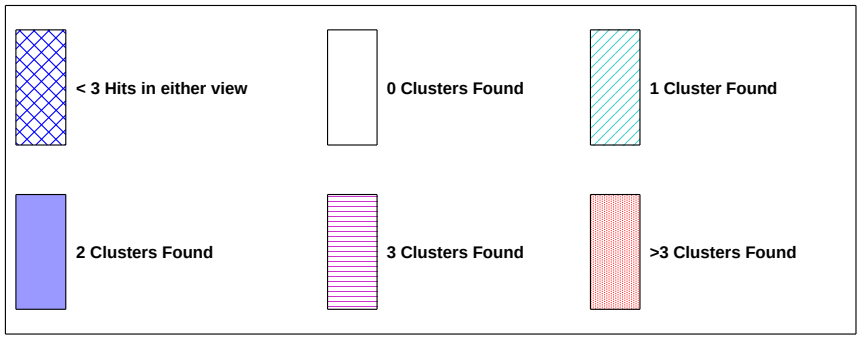

Figure 4.2: The legend for the figures 4.3 through 4.6, which all show the mean number of clusters produced between the two 2D views in an ECal.

Figure 4.3 starts by looking at the effect of energy on the reconstruction of muons from the single particle gun events. Two plots are shown, both in the same format; the X axis covers kinetic energy in 50 MeV bins, and Y shows the distribution of the events between several outcomes, normalised to 100%. The same style is used for figures 4.3 through 4.6, and figure 4.2 provides a legend.

The hatched blue region of the plots shows events in which there were less than 3 hits in one or both views of the ECal. This is the bare minimum for a successful reconstruction, and is highly dependent on the energy. Less than 5% of muons in the 0 – 50 MeV bin manage to pass through the dead material in front of the DsECal and produce enough hits. In the next energy bin, this number has jumped to 65%, which is later shown to be an effect of the angle. Above 100 MeV the vast majority of muons leave a clear signal.

Within the events which have sufficient hits, there are a number of clustering outcomes. The first two are failing outcomes: the white space shows events where no clusters were found and the region with diagonal cyan stripes shows events where a cluster was reconstructed in only one view. These are events where the clustering algorithm is considered to have failed because there are sufficient hits from the particle but they were not reconstructed. The plot clearly shows that this is often true for low energy events, and the primary cause is that there are 3 hits, but they are sparsely distributed after the muon has stopped or decayed. Deeming this to be a failure of the clustering algorithms is possibly harsh, as there is no clear signal to be found, but for the purpose of defining efficiency it is necessary.

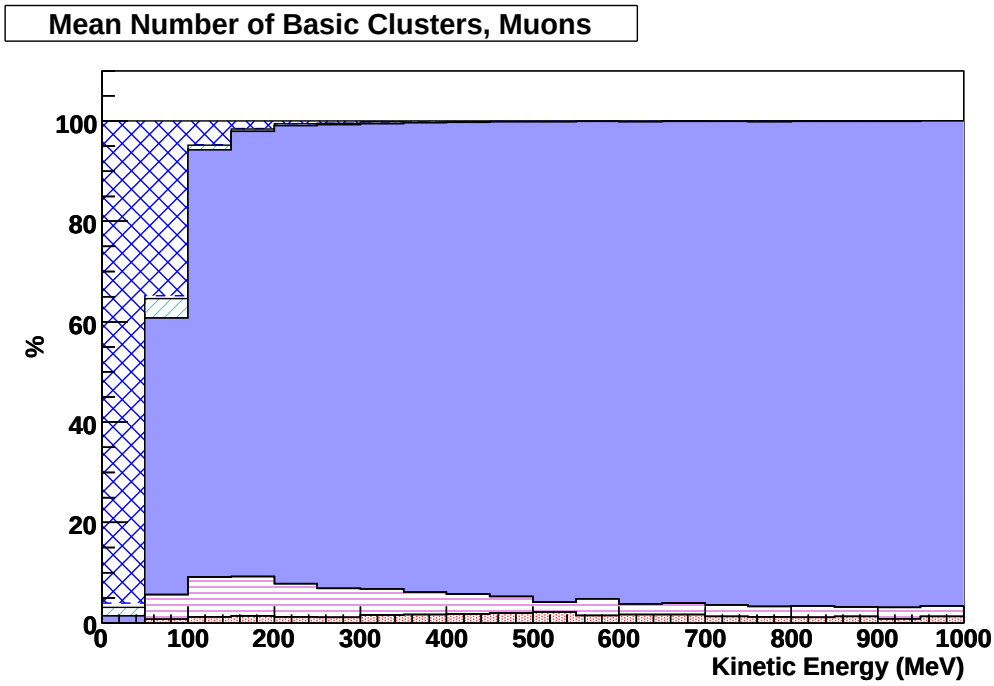

(a) Basic Clustering with respect to Energy

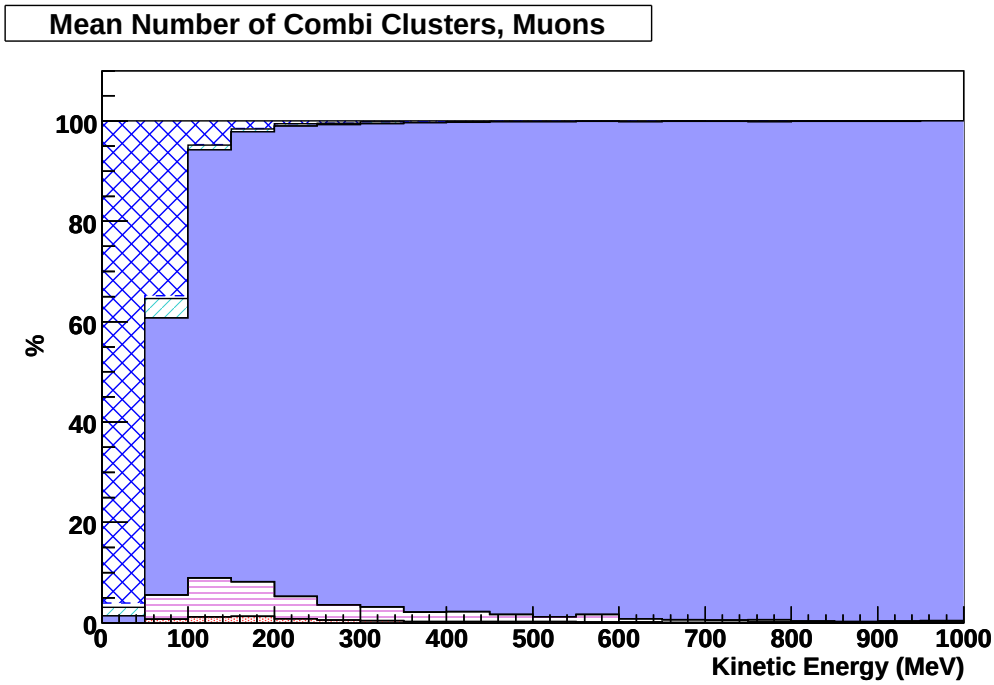

(b) Combine Clusters with respect to Energy

Figure 4.3: The effect of particle energy on the basic clustering and combine clusters methods, for muons. In each plot, the mean number of clusters found between the two views is shown. Produced from events with a single muon particle gun. See figure 4.2 for the legend.

The further layers of the plot show the varying number of clusters found, solid blue for 2 clusters (one in each view), horizontal magenta stripes for 3, and dotted red for 4 or more. Whilst the 1 cluster per view result is optimal, all these results are considered successful at this stage, as there are further algorithms to be considered. For muons, the majority of events are completely successful (1 cluster per view), with only a small contamination where a track has been split into multiple clusters.

The second plot shows that many of these events are recovered by the 'combine clusters' method, especially at higher energies. This is explained by the likely causes of the splitting and may be best seen by examining figure 4.4, which investigates the effect of angle. After 'combine clusters', any reconstructed event which has not resolved to a single cluster in each view is considered a failure of the algorithms. This is not say that the reconstructed information will not be useful, as in most failed events it is still possible to identify the clusters as a track and connect it with an incoming TPC track.

The angle of incidence has a large effect on the ECal reconstruction; it determines the thickness of lead that a particle must pass through before it encounters another active layer. Plot 4.4(a) shows a constant band of approximately 12% of events which failed the 3 hit cut, due to the lowest energy muons. However, on top of this there is an increasing trend for failure as the angle increases, for both insufficient hits at lower energy and split clusters. The most common cause for a split cluster is a geometric effect where a particle traverses so far within a layer that the hits in the layers before and after (which will be in the alternate XZ or YZ view) are separated by a full bar width.

The 'combine clusters' algorithm was designed to correct for this problem, and plot 4.4(b) shows that it does in many cases, but the success is dependent on the track shape. A long straight track from a high energy muon will be easily reconnected, whereas lower energy muons may be shorter, bent more by the magnetic field or scattered, all of which will have a detrimental effect on the reconstruction.

Figures 4.5 and 4.6 show the same information, but for the single photon particle gun events. There is the same rise in efficiency as the energy increases, with a

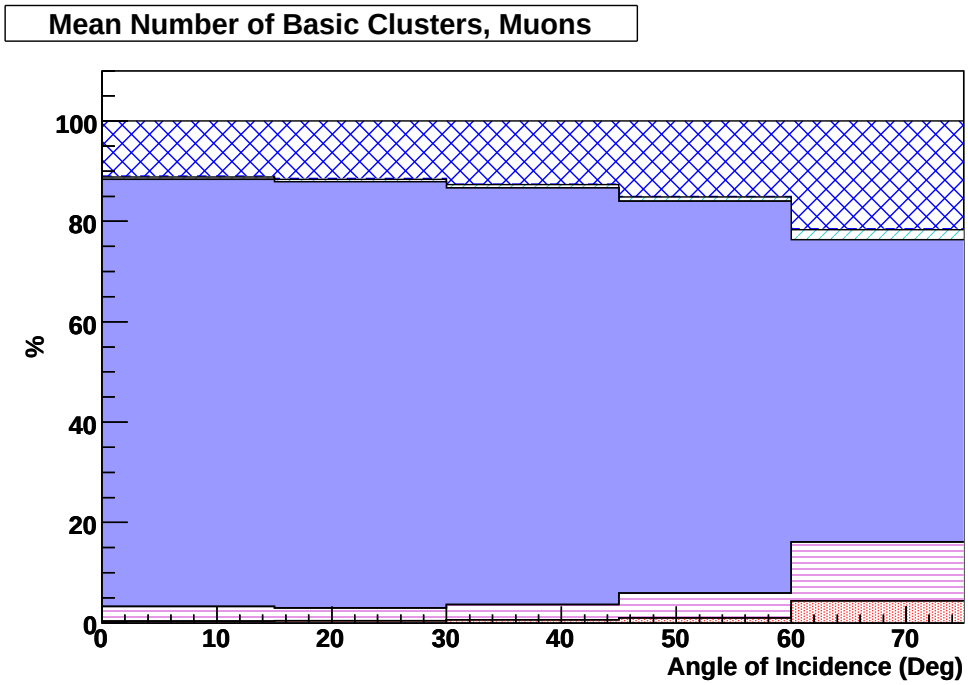

(a) Basic Clustering with respect to Angle

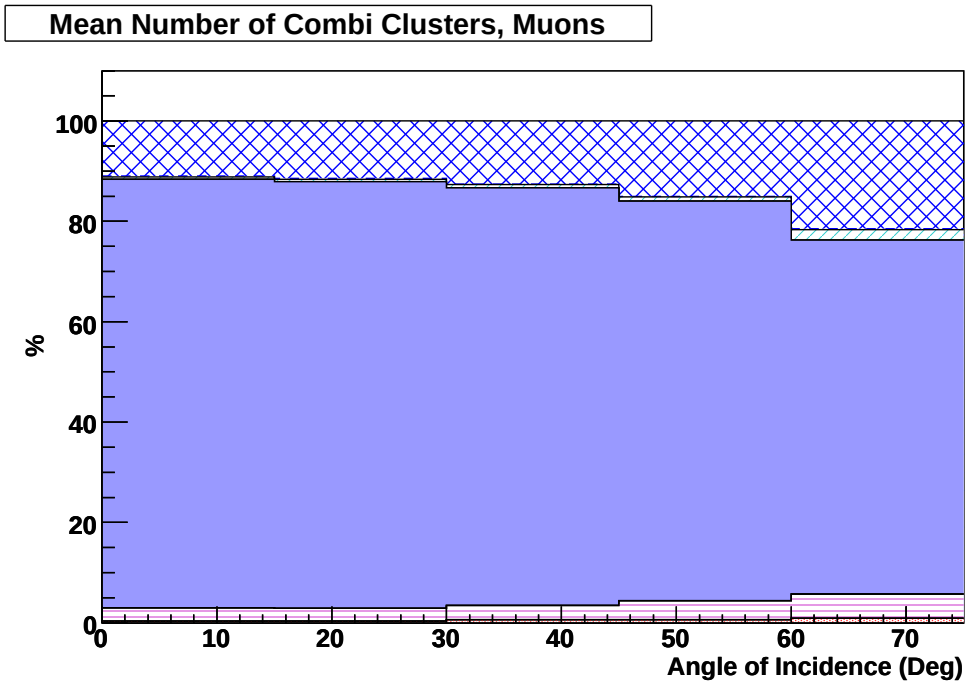

(b) Combine Clusters with respect to Angle

Figure 4.4: The effect of the angle of incidence on the basic clustering and combine clusters methods, for muons. In each plot, the mean number of clusters found between the two views is shown. Produced from events with a single muon particle gun. See figure 4.2 for the legend.

slightly improved number of events with sufficient hits at low energy (due to the photons being less affected by the dead material). However, the probability that no clusters were found in one or both views is much higher. This is because photon showers tend to be sparser objects than MIP tracks, and generally produce less hits which are more difficult to join into a clear signal.

The likelihood of a shower being split is also much higher than in the muon cases, due to the inherent nature of the shower. As the shower progresses by pair production and bremsstrahlung, a high energy photon can travel a small distance before it starts to produce charged particles and a signal. If this carries it away from the main body of the shower, either by travelling further into the ECal than the rest or by moving sideways, then two clusters are formed. Unlike with muons, there is no real angular dependence on this effect, therefore the ratio of events stays fairly constant in figure 4.6.

There is a slight change with energy, not because of an increased probability of an offshoot photon, but because of the size of the total shower, which expands with energy. After 'combine clusters' this effect is diminished, due to the form that the algorithm takes. Specifically, the method was designed to be effective for both tracks and showers, therefore the shape of a shower is not fully considered. The algorithm searches for clusters along the trajectory of the largest cluster, which is effective for muons or continuations of the shower, but will leave secondary showers to the side unattached. As the continuation showers were more likely at lower energies, these have been collected and the constant 10% of events where a side shower formed is largely unaffected.

The actual shape of a shower is much closer to a cone, and that approximation could have been used for the 'combine clusters' and 'expand clusters' methods. However, it relies on several assumptions: firstly, that the object is indeed a shower (not a track) and secondly that the direction of the shower is known. Neither of these assumptions are permissible at an initial clustering level, as an increased efficiency for showers could have a large detrimental effect on the purity of tracks; but they will be used by later steps of the reconstruction, after modules for particle identification and matching with the TPCs or FGDs.

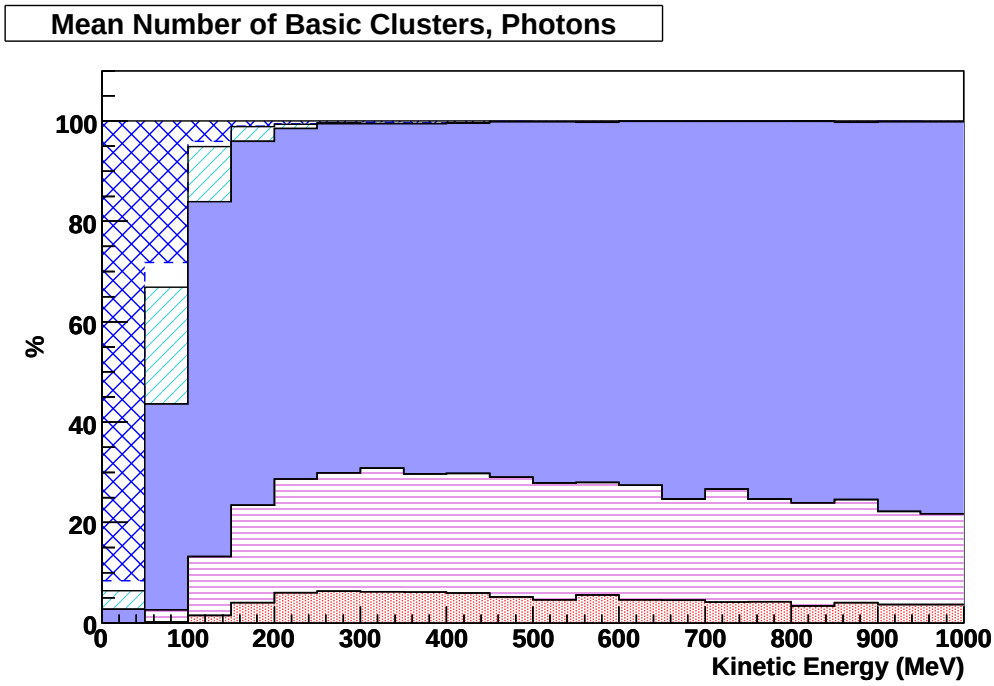

(a) Basic Clustering with respect to Energy

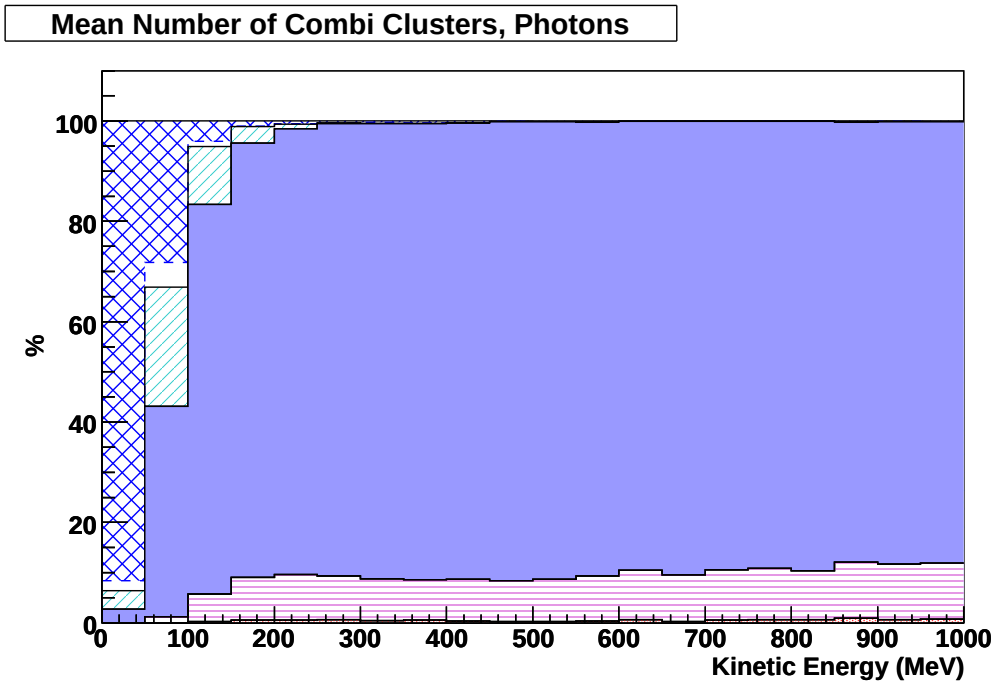

(b) Combine Clusters with respect to Energy

Figure 4.5: The effect of particle energy on the basic clustering and combine clusters methods, for photons. In each plot, the mean number of clusters found between the two views is shown. Produced from events with a single photon particle gun. See figure 4.2 for the legend.

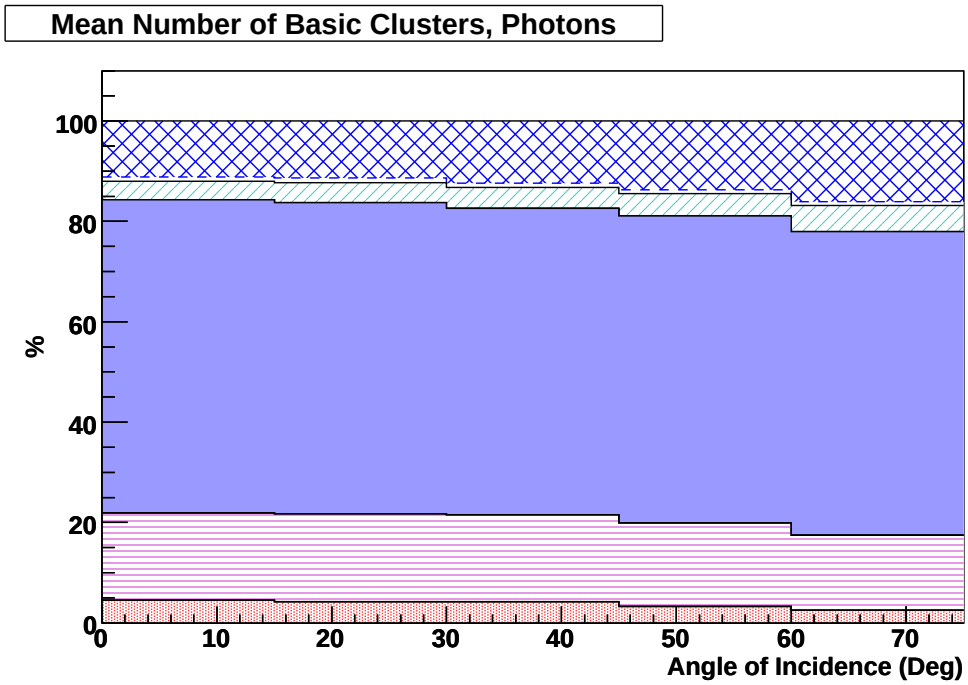

(a) Basic Clustering with respect to Angle

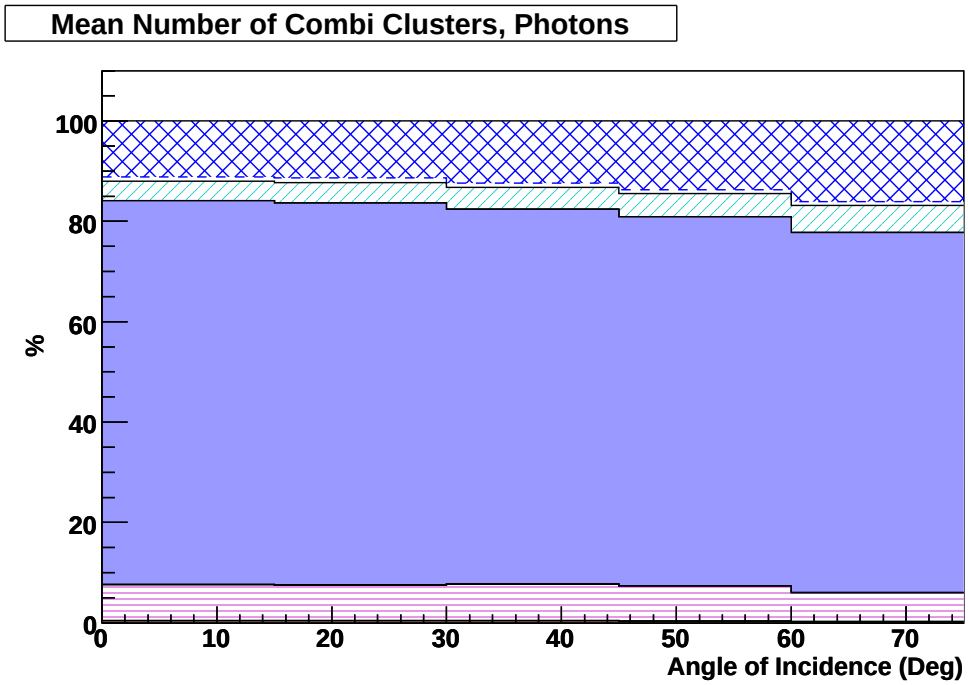

(b) Combine Clusters with respect to Angle

Figure 4.6: The effect of the angle of incidence on the basic clustering and combine clusters methods, for photons. In each plot, the mean number of clusters found between the two views is shown. Produced from events with a single photon particle gun. See figure 4.2 for the legend.

4.3 Hit Completeness and Purity

Having identified the clusters, the next quantity to consider is the hit completeness, the number of hits generated by the particle that were successfully added into the cluster. This can be considered as either a strict percentage of the hits or a percentage of the charge. Whilst it might appear that the charge is a more important quality this is not strictly true, because of the energy fitter method used for showers.

Each shower is considered as a distribution of hits, and the form of that distribution is fitted using a large number of variables, as explained in section 3.4.5, and the position of a hit can be as important as its charge. Therefore, figure 4.7 shows the percentage of hits correctly clustered.

The 'expand clusters' method has little effect on MIPs, as the majority of hits tend to be included anyway. Also, 100% completeness is rarely required for a successful reconstruction of position and angle. At higher energies, the mean number of hits produced by a MIP is determined not by the energy but by the number of layers it passes through. Therefore, the strong line at 96% (which accounts for approximately 5% of the events) is caused by one hit missing from an expected number of 17 – 19. This hit is often adjacent to the track, caused by a delta ray, and its addition to the track would not improve the position or direction measurement, but instead serve to confuse it.

In contrast, the improvement seen for photons is much more pronounced. A large proportion of the hits can be seen to be regularly missed at earlier stages, but after the complete set of algorithms it can be seen that 99% of the higher energy particles have a hit completeness of 90% or higher. At lower energies, the tail can be seen to extend downwards, but again this is an effect of the mean number of particles produced by a shower. The first bin has clear entries for 50, 60, 75 and 80% completeness, which correspond to clusters of 3 or 4 hits out of an available 4 to 6.

The concern with the expanded clusters is that they will include hits which were not associated with the primary particle being considered. These hits will likely come

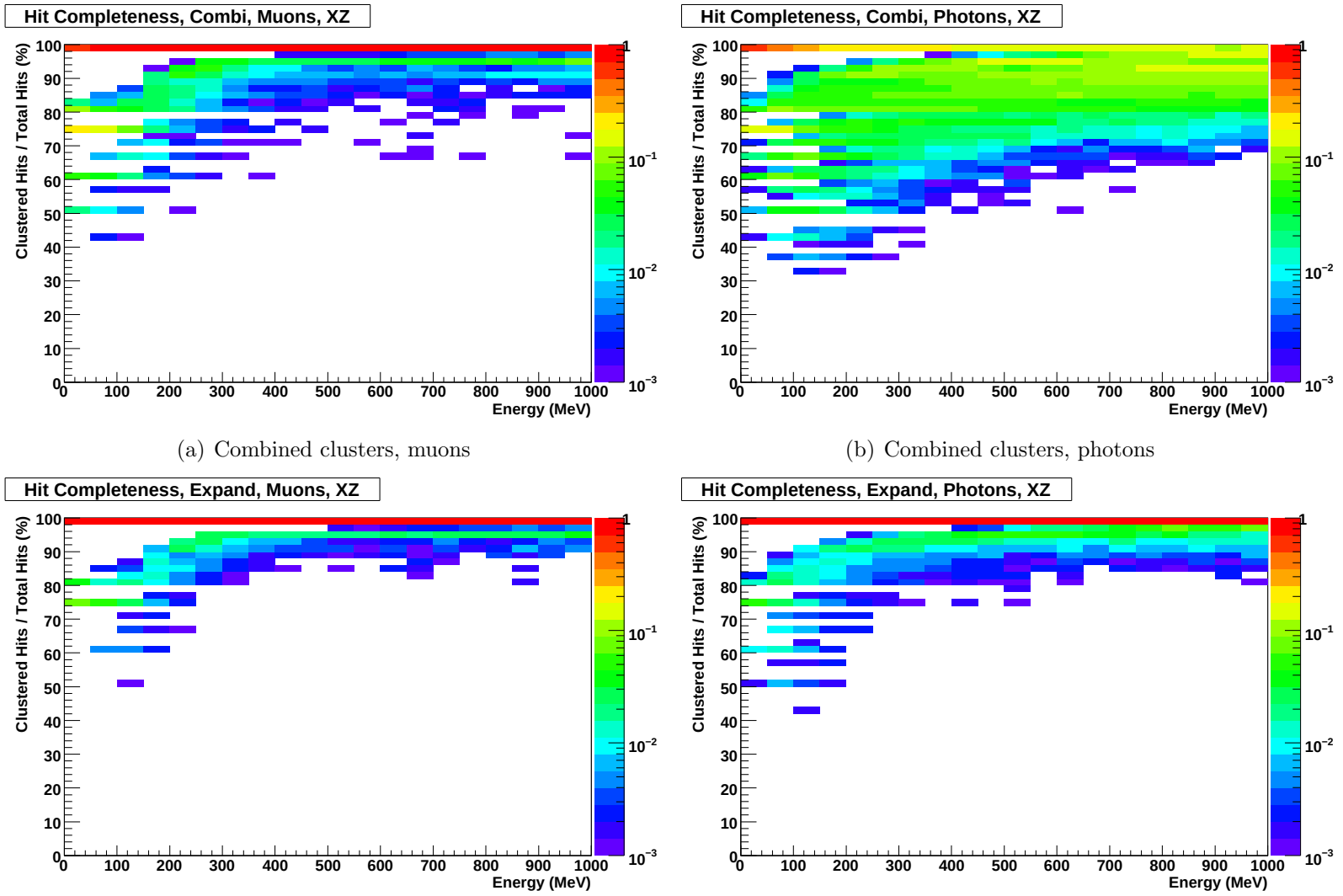

(a) Combined clusters, muons

(b) Combined clusters, photons

(c) Expanded clusters, muons

(d) Expanded clusters, photons

Figure 4.7: The effect of the 'expand clusters' algorithm on the hit completeness for muons and photons. For simplicity, only one view (XZ) of the ECal is considered, and an initial cut is applied, selecting events in which a single cluster was reconstructed. The events are particle gun events with a single muon or photon.

from one of two sources, either noise or other particle interactions in the ECal. The effect of noise was not completely simulated in the ND280 code at the time of this work, so it was not possible to optimise the algorithms with that information. In fact, it is unlikely to be possible until after the ECal beam test, which will be in mid 2009, as a full analysis will require not only the noise rate, but also the light yield of the bars in situ. Current estimates and simulations suggest that the light yield will be high enough to discount hits at the 2 p.e. level as being due to noise, and still have the majority of real hits being considered, but this is not certain.

As the noise could have a large effect on several stages of the ecalRecon algorithms, chapters 5 and 6 explain work and an analysis carried out on data from the SciBooNE experiment, aiming to demonstrate the effects of noise on the algorithms. The analysis also provides evidence to support the efficiencies and purities produced in this chapter.

To investigate the contamination of clusters with extra hits from other interactions, the full bunch background sample from section 4.1.2 is used. Figure 4.8 shows the extra charge included in the clusters, based on the truth information for the sample photon or muon and for any other particles interacting in the ECals. It can be seen that only about 3 – 4% of events have extra charge associated with them and that the amount is generally very small. The only effect not shown on the plots is the extension of the 0 – 50 MeV bin for photons, which has a very small number of events all the way up to 400%. These are clusters where the primary photon has become a contaminant to a significantly higher energy particle passing through the ECal, but are rare.

4.4 Direction Reconstruction and Resolution

Once ECal tracks and showers have been reconstructed, the reconstruction will be designed to attempt matching ECal objects to objects reconstructed in other regions of ND280, such as the TPCs or FGDs. Generally, this form of matching is achieved using two variables, position and direction. The cluster's position within the ECal

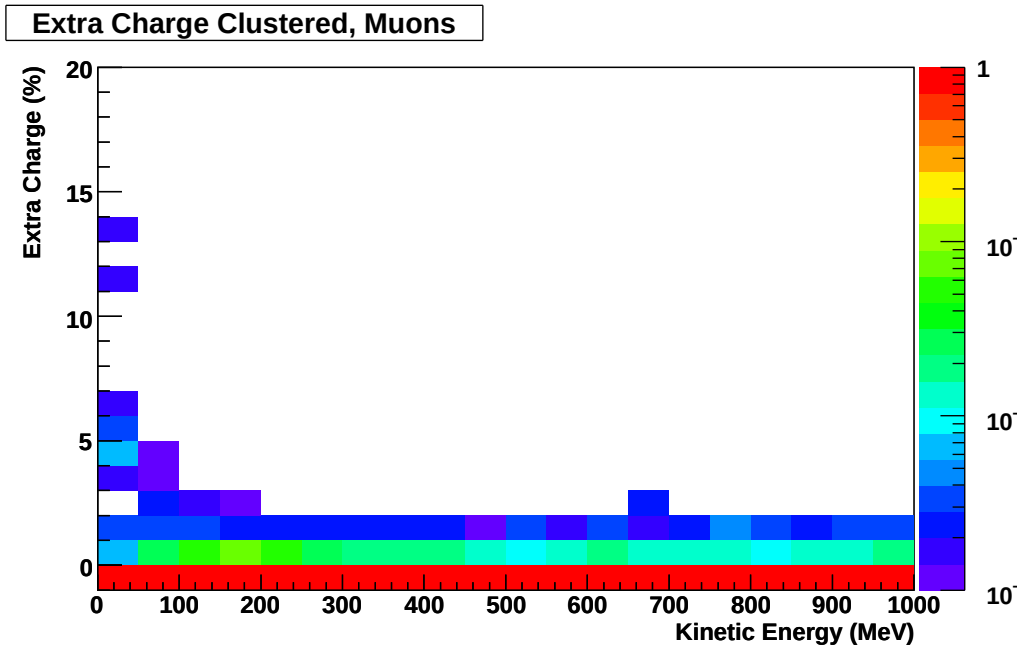

(a) Extra Charge, Muons

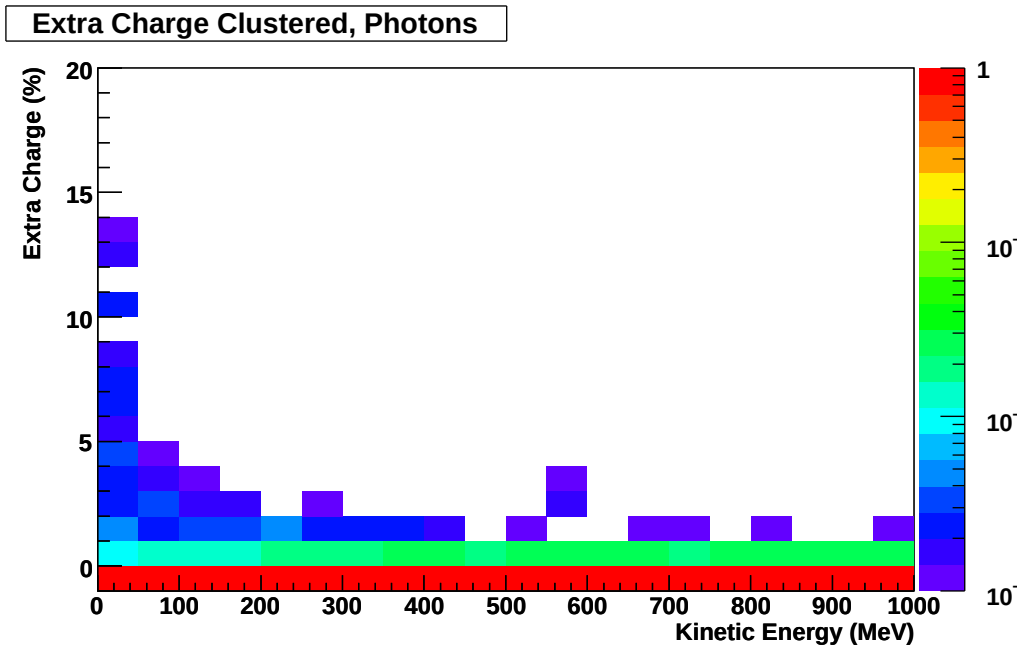

(b) Extra Charge, Photons

Figure 4.8: Extra charge clustered by the expand algorithms method. The events used include a full spill of background events, and the plot shows the extra charge, as a percentage of the 'genuine' charge included in the cluster, i.e. that produced by the target particle, determined from MC truth information.

(for the purpose of matching tracks from the TPC) is easily determined from a charge weighting of the hits in the innermost layer. The results from this method are shown, plotted against the kinetic energy, in figure 4.9.

Plots (a) and (b) show the difference between the reconstructed front point and the projected track position at the same Z, for events where 1 cluster is reconstructed in each view. Each column is renormalised to 1 and the z axis is against a logarithmic scale. Plot (c) shows Gaussian fits to each slice of plot (a), and demonstrates that there is no systematic asymmetry in the reconstruction and that muons are resolved to within 25 mm. The same plot for photons, (d), shows a comparable resolution. The lowest energy muons show a slightly worse resolution, but this effect is not seen for the photons, suggesting it is due to the magnetic field bending the particle, producing an error in the projected position instead of the reconstructed one.

The direction of clusters is more difficult to determine, and two methods are currently used within the ECal. The first is a principal component analysis (PCA), as used in the combine and expand clusters methods. The second method is referred to as a thrust method, a technique which has been used in a number of particle physics experiments. The thrust axis $\vec{n}$ of a cluster is the vector which maximises the equation:

$$T \overset{max}{=} \frac{\sum_h C_h |\vec{r}_h \cdot \vec{n}|}{\sum_h C_h |\vec{r}_h|} \tag{4.1}$$

where C_h and $\vec{r}_h$ are the charge and position of each hit, with respect to a proposed starting position of the shower or track. Therefore, unlike the PCA method, thrust has to make an implicit assumption; that the particle was travelling outwards from the centre of the detector. This is true for the particle gun files produced, but may well not be in a real event.

The angle reconstructed by the PCA and thrust methods is shown in figures 4.10(a) through 4.10(d), compared to the truth angle of the incoming particle. All angles are contained within the 2D XZ view, for the simple reason that this view of the detector is unaffected by the magnetic field of the detector. In the YZ view, the angle is still reconstructed, with a slight decrease in accuracy due to the field, but the truth value is not guaranteed to be accurate as the particle will have bent between

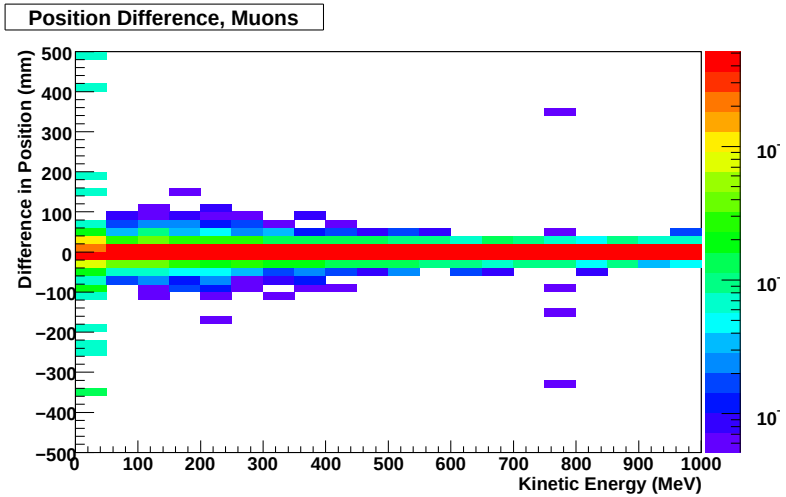

(a) Difference in Position, Muons

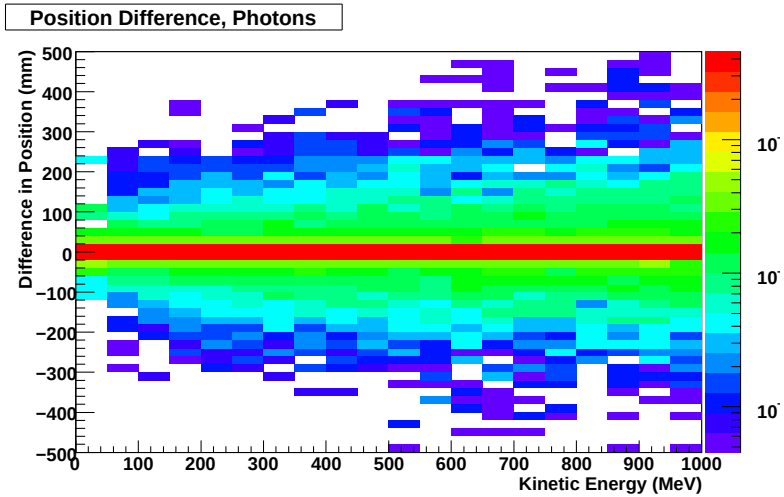

(b) Difference in Position, Photons

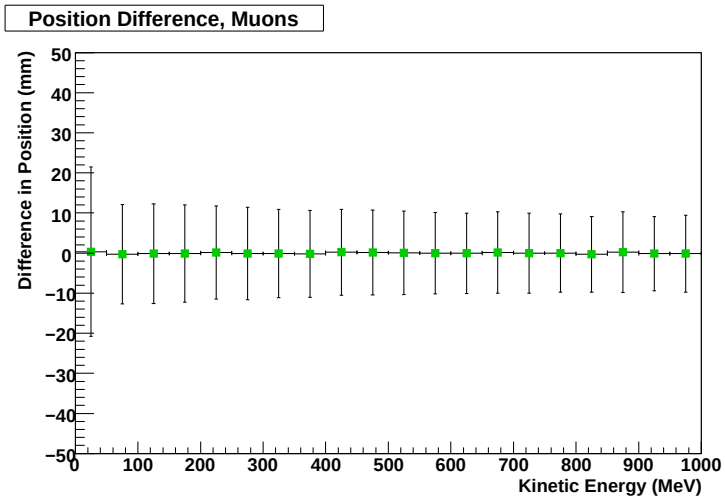

(c) Gaussian Fit, Muons

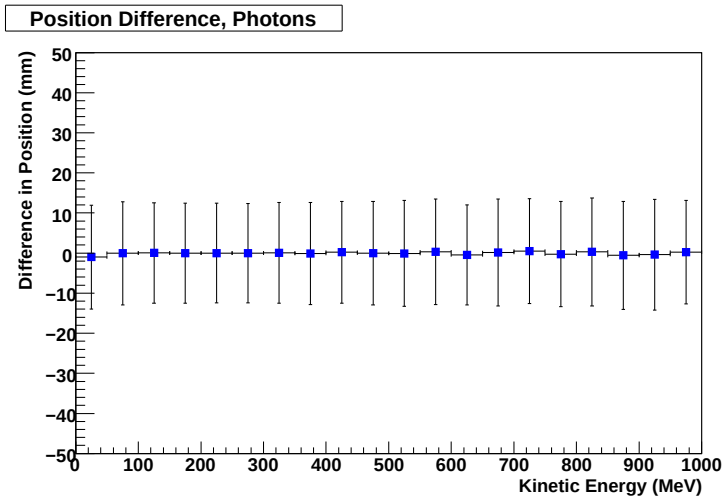

(d) Gaussian Fit, Photons

Figure 4.9: The reconstructed position of clusters, compared to the projected particle track.

production and entering the detector. As this effect is dependent on both angle and energy, it is easier to consider only the XZ view. Only events which have a single reconstructed XZ cluster are considered, i.e. those which successfully passed through the reconstruction.

The figures generally show a good agreement between the true angle and the reconstructed one, producing a band with a width of approximately $5 - 10°$. There is one artifact of the reconstruction visible, which is a strong line at $0°$, especially for the muons. This is a factor of the detector design; the ECal bars are 4 cm wide only separated by 2.1 cm in the Z direction. If a muon only passes through a number of scintillating planes before passing out of the side of the ECal, e.g. 6 planes, then a MIP travelling at $20°$ could still be reconstructed as having an angle of $0°$.

Also shown in figure 4.10 are two plots referring to 'mean', which is the mean value of the thrust and PCA methods. In general, this is an improvement over either method on its own; however it can be worse at higher angles. This is because a reconstructed angle of $90°$ and $-90°$ are the same. If one method reconstructs a large positive angle, and the other reconstructs a large negative angle, then the mean angle becomes close to $0°$, instead of $\pm 90°$.

The difference between the mean angle and the truth angle is shown in figure 4.11, with respect to the kinetic energy of the particle. The data points correspond to the mean value of a Gaussian fit, and the error bars are the RMS of the fit. The points are close to $0°$ for both muons and photons, but the widths are noticeably wider for the photons. This is not very surprising, since the nature of an EM shower makes it difficult to reliably determine its direction, as there is no guarantee that the energy will be observed symmetrically about the centre of the shower. However, the resolution of $15 - 20°$ for photons in the middle energy range is reasonably good, and the muon resolution is sufficient (given that the direction and position returned by TPC tracks will be much more accurate).

As the clustering has been shown to be very efficient with good inclusion of the hits, the suggestion is that the direction-finding methods are the weakest link. The thrust method is overly affected by small hits a long way from the origin of the cluster, an

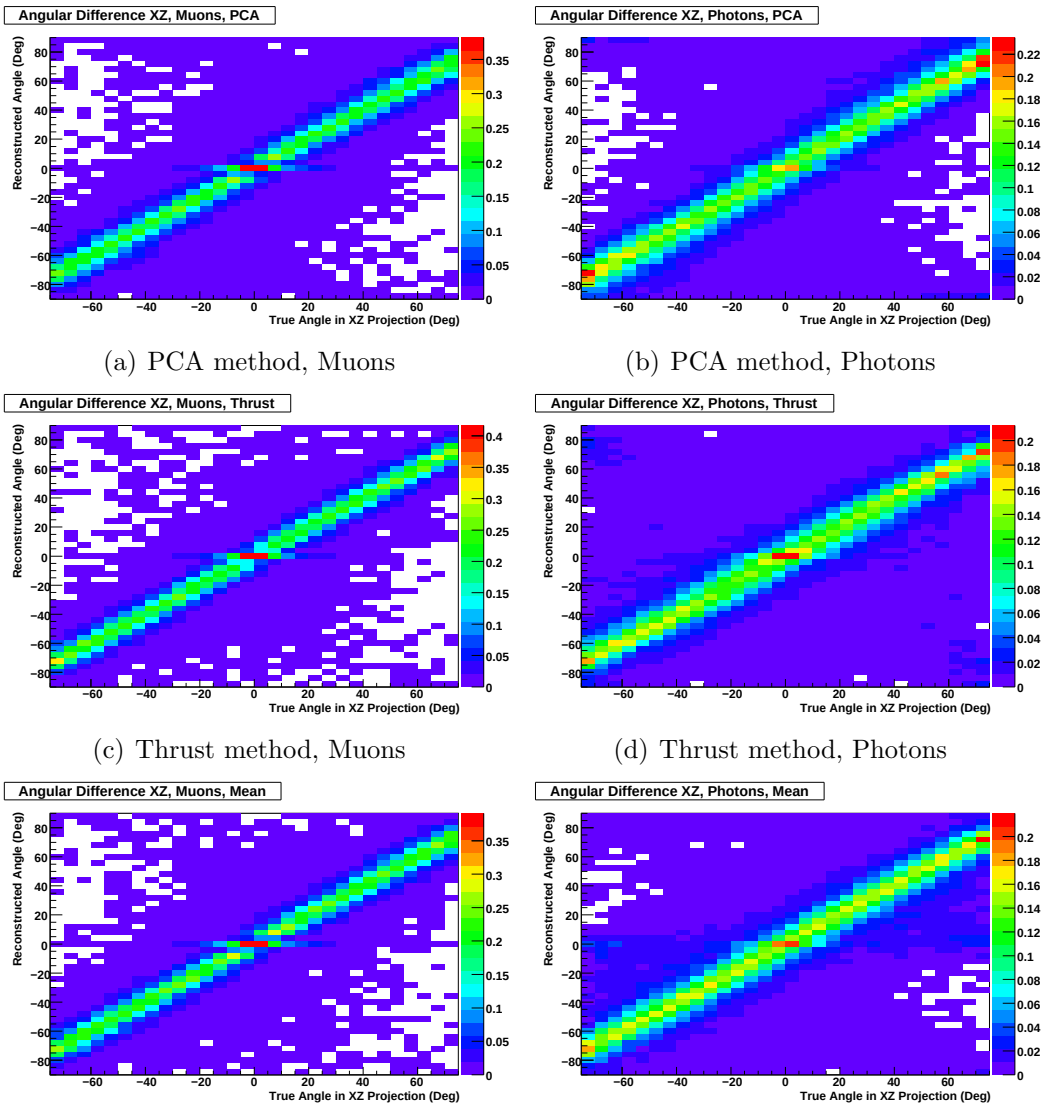

(a) PCA method, Muons

(b) PCA method, Photons

(c) Thrust method, Muons

(d) Thrust method, Photons

(e) Mean method, Muons

(f) Mean method, Photons

Figure 4.10: The reconstructed direction of expanded clusters, plotted against the true angle of the particle. In all cases, the angle is calculated within the 2D XZ view, as this view is unaffected by the magnetic field of the detector and gives the best idea of the position resolution. Three angles are shown for each particle type; those reconstructed from the PCA and thrust methods, as well as the mean of the two methods.

effect which could be limited by only considering portions of the cluster. This work is currently being examined by another T2K student.

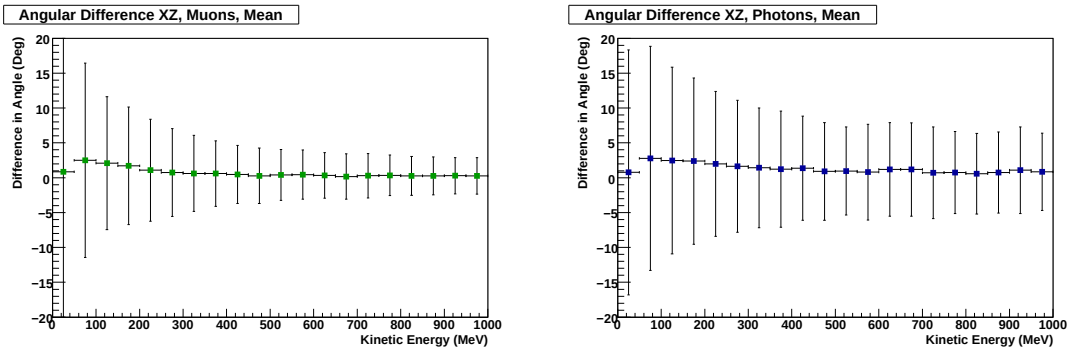

(a) Mean method, Muons

(b) Mean method, Photons

Figure 4.11: The resolution of the reconstructed direction, as calculated by the mean method and compared to the true angle within the XZ view.

4.5 Conclusions

The ecalRecon methods appear to work with good efficiency and purity on the MC simulations. The most strict definition of success for an event would be to require that one cluster was reconstructed in each view, with each cluster containing 90% or more of the hits. Figure 4.12 shows the efficiencies for five energy ranges of the two particle types. Both of the particles have a low efficiency, below 5%, in the lowest energy range, predominantly due to the low number of hits. The efficiency of the muons then rises to 50% for the 50 – 100 MeV range and approaches 90% for particles over 100 MeV. The photons tend to lag behind the muons, by approximately 10%, reaching 85% above 500 MeV.

However, this definition of success is harsher than is strictly necessary. A number of events are lost because the showers or tracks were split, but these events will still be used at a global reconstruction level. At the same time, the majority of low energy particles are missed because of insufficient hits, but there is nothing that the reconstruction can do about this without introducing a larger sample of false positives. Also, muons and electrons of this energy will be detected before they enter the ECal, so the global reconstruction will still succeed. In fact, the only

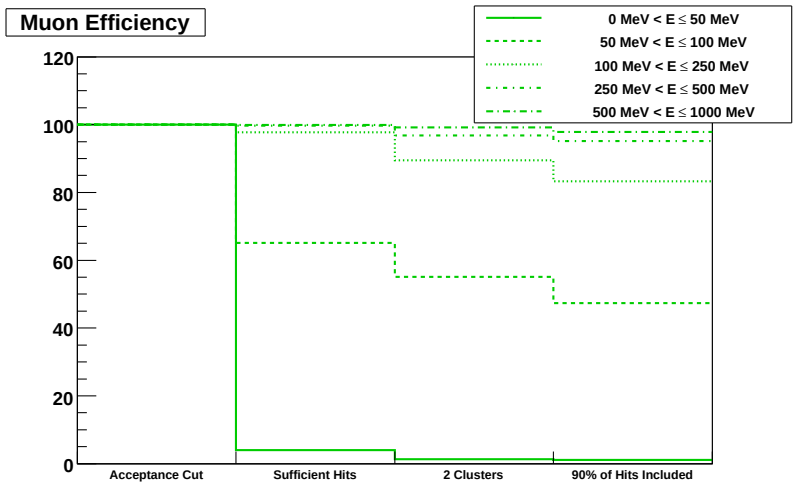

(a) Efficiency, Muons

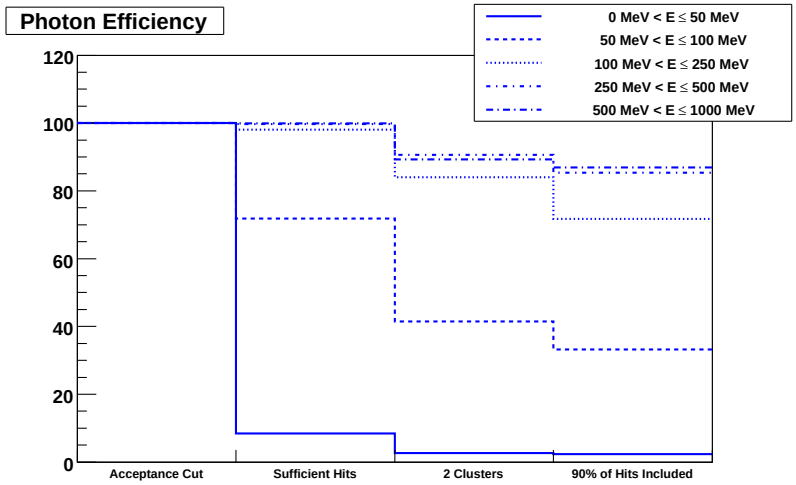

(b) Efficiency, Photons

Figure 4.12: The final efficiency of the ECal reconstruction, for photons and muons. For each particle type, lines are plotted for five energy regions, against the major requirements for a successful conclusion of the reconstruction.

particles which will be truly lost are the photons. This is the central problem in any π^0 analysis, and has been observed by many neutrino experiments. Chapter 6 demonstrates this problem within the SciBooNE experiment.

The algorithms of ecalRecon provide a strong and stable basis for the clustering of ECal events, upon which analyses or further reconstruction methods can be based. They provide a good efficiency and purity, without making any event-specific assumptions, and will act as a first stage of the global ND280 reconstruction.

Chapter 5

The SciBooNE Experiment

The SciBooNE experiment was proposed as a way of using existing resources to make measurements, that were not available to other experiments running at the time, focusing on neutrino interaction cross-sections. It was situated at the Fermi National Accelerator Laboratory (FermiLab) in Batavia, Illinois, USA, which is home to the Tevatron particle accelerator and a number of particle physics experiments, including neutrino experiments such as MiniBooNE (Mini Booster Neutrino Experiment) and MINOS (Main Injector Neutrino Oscillation Search). There are two neutrino beams at FermiLab. The NuMI (Neutrinos at the Main Injector) beam serves MINOS, taking 120 GeV protons from the Tevatron's main injector. The second beam is the Booster Neutrino Beam (BNB), which takes 8 GeV protons from the Booster, the component prior to the injector in the Tevatron's proton acceleration process.

The BNB was initially constructed for MiniBooNE, and was simultaneously used by SciBooNE. SciBooNE also made use of the SciBar and EC detectors, both of which had been previously used at K2K. The only detector which was designed and constructed solely for SciBooNE was the MRD, although even this was constructed from second-hand materials.

The neutrino flux seen by SciBooNE, which is shown in figure 5.1, was a good match in energy to the T2K flux, although of much lower power. In fact, one of the three motivations specifically mentioned in the SciBooNE proposal [66] is to make

measurements useful for the T2K experiment, concentrating on cross-sections of the signal and background channels.

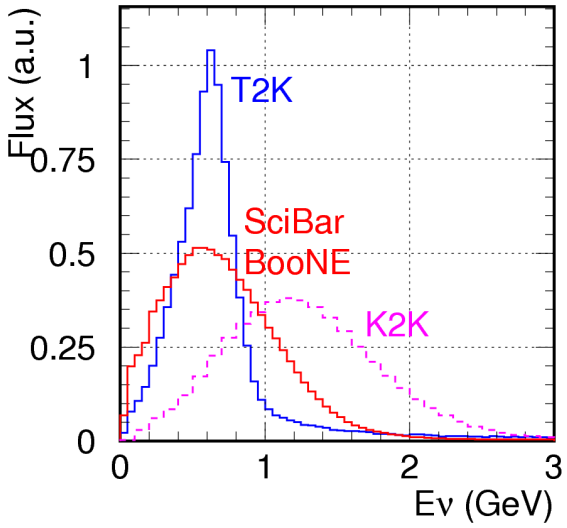

Figure 5.1: The flux seen by the SciBooNE detector, compared to flux seen by the K2K experiment and the predicted flux of T2K.

5.1 The Booster Neutrino Beam (BNB)

Full details of the BNB can be found in the BooNE technical design reports [67, 68, 69, 70], but the basics will be described here. 8 GeV protons are extracted from the booster and bent towards the target. The protons arrive in batches of 84 bunches, each bunch with a width of ~ 4 ns and a peak-to-peak separation of ~ 19 ns. Each batch contains $\sim 4.5 \times 10^{12}$ protons, and the horn is limited to 5 Hz.

The target is a cylinder of beryllium, 1 cm in diameter and 71 cm long, and mesons are produced by the proton-Be interactions. Just downstream of the target is a single magnetic horn. Depending on the polarity of the ~ 170 kA current, the horn either focuses π^+ and defocuses π^-, or defocuses π^+ and focuses π^-. The pions enter the short decay volume (50 m) and decay via the same processes as discussed in section 2.1. Therefore, focusing π^+ produces a beam of ν_μ and is called neutrino mode, as opposed to antineutrino mode for the focused π^-. As T2K will run in

neutrino mode for the first five years, only neutrino mode SciBooNE data will be used for the analysis.

Any pions or muons which reach the end of the decay volume are slowed by the absorber, limiting the production of any further high energy neutrinos or antineutrinos from pion or muon decays. The decay volume also has a movable absorber, halfway along the length, made of iron panels. These were held above the decay volume, but could have been lowered into place to change the beam composition. This only happened once, before SciBooNE started running, and was accidentally caused by the failure of chains holding the panels in place.

The SciBooNE proposal requested 2×10^{20} protons on target (POT), with a 1:3 split between neutrino and antineutrino mode. Table 5.1 shows the data collected by the experiment before it stopped running in August 2008. The full 0.99×10^{20} POT of neutrino data are used for this thesis.

Run	Period	POT
Run 1 (Antineutrino)	Jun. 2007 – Aug. 2007	0.52×10^{20}
Run 2 (Neutrino)	Oct. 2007 – Apr. 2008	0.99×10^{20}
Run 3 (Antineutrino)	Apr. 2008 – Aug. 2008	1.01×10^{20}

Table 5.1: The number of protons on target (POT) of data collected by the SciBooNE Experiment and used in chapter 6. Numbers are taken from [71].

5.2 The SciBooNE Detectors

The SciBooNE detector hall was placed 100 m downstream of the target and 441 m upstream of MiniBooNE. The detector sat directly on-axis, about 7 m below ground level with no coverage from above, so there was a high flux of cosmic muons passing through the detector. The timing signal provided a tight constraint on these as a background, which allowed them to be used for commissioning and calibration purposes.

The SciBooNE detector hall held three detectors, which can be seen in figure 5.2. The most upstream detector is a segmented plastic scintillator detector, called

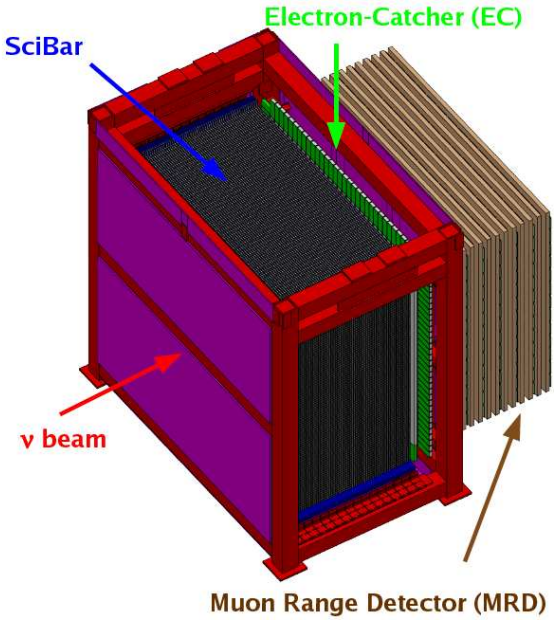

Figure 5.2: The SciBooNE detector suite, containing three detectors. Upstream is the SciBar, a fine grained detector and fiducial mass, constructed from extruded scintillator. In the centre is the Electron Catcher (EC), a 'spaghetti' calorimeter design, for measuring the energy of electromagnetic particles leaving the back of SciBar. Finally there is the Muon Range Detector (MRD), with alternating layers of iron and scintillator, where the muon's energy is determined from the number of layers traversed.

SciBar, which acts as the fiducial target. Next is the Electron Catcher, a 'spaghetti' calorimeter for measuring electrons or photons not contained by SciBar. Lastly, there is the Muon Range Detector, with alternating layers of iron and scintillator for measuring the energy of muons.

5.2.1 The SciBar

The SciBar was built in 2003 for the K2K experiment, as an additional near detector at KEK [72]. The design has similarities with ND280's FGD and P0D sub-detectors, both of which were designed after looking at the strengths and weaknesses of the SciBar. It was constructed from rectangular strips of extruded scintillator, $1.3 \times 2.5 \times 300$ cm, with a WLS fibre running down the centre of each bar. There are 14,848 bars in total (however only 14,336 are instrumented), in 64 layers, containing two panels of 116 bars each, weighing a total of 15 t. The bars ran horizontally and vertically, so that the detector can reconstruct 3D tracks (figure 5.3).

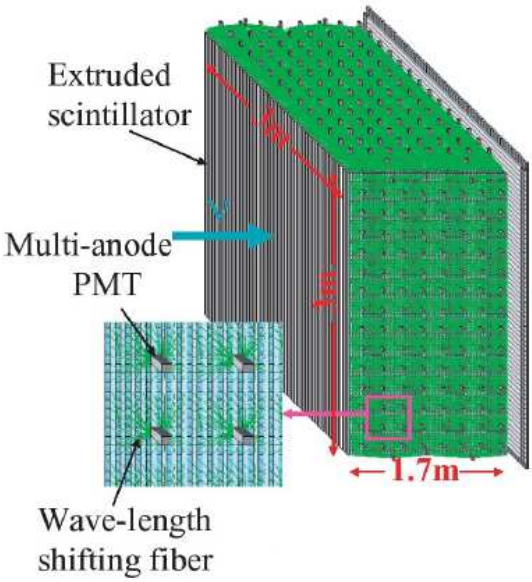

Figure 5.3: The SciBar (a contraction of scintillating bar) is constructed from extruded scintillator. Each bar has a central WLS fibre, leading to a multi-anode photomultiplier tube (MAPMT).

The fibres from each 8×8 group were read out by a 64 channel multi-anode photomultiplier tube (MAPMT), the H8804 manufactured by Hamamatsu. The electronics and DAQ are explained in detail in [73, 74, 75], but for each MAPMT there are 64 ADCs and two TDCs. Each TDC is responsible for a 32 channel cell (a 64 channel group is split front and back), and has ns timing resolution. After the first time value is recorded, there is a reset period of 50–100 ns and then the TDC is live again. These multiple TDC hits are very useful for identifying Michel electrons from muon decays. The first TDC hit also triggers the integration of all ADC channels in the cell, which integrate over 2 µs.

The SciBar produces a homogeneous detector volume, and events are reconstructed as a number of tracks. Several methods for particle identification are available, some relying on other detectors. Using thhe energy deposit per mm, dE/dx, it is possible to distinguish protons from $\pi^{\pm}/\mu^{\pm}$, as protons deposit a large amount of energy over a short track. Electrons and photons can often be distinguished using track shape and energy deposit, although this is more difficult than in the ND280 ECals or P0D, due to the lack of an absorber, such as lead, to increase showering. Any tracks which pass out the back of the SciBar can be identified as muons by a

corresponding track in the Muon Range Detector or electrons/photons from a large deposit in the Electron Catcher.

5.2.2 The Electron Catcher (EC)

Shown in figure 5.4, the EC is a 'spaghetti' electromagnetic calorimeter [72]. Originally created for CHORUS, a $\nu_\mu \rightarrow \nu_\tau$ oscillation experiment at CERN [76, 77], the detector was then shipped to KEK to be used in K2K, in the same position relative to the SciBar as it occupied for SciBooNE.

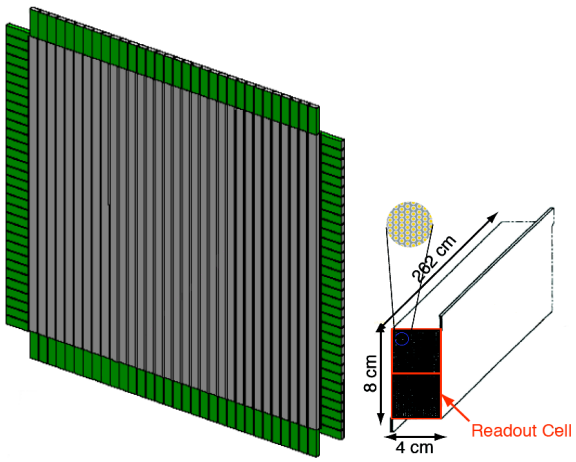

Figure 5.4: Used in both CHORUS and K2K, the Electron Catcher is an electromagnetic calorimeter, placed downstream of the SciBar, to measure the energy of particles leaving the back.

The EC has two planes, one vertical and one horizontal, each with 32 modules. 1 mm diameter scintillating fibres are laid in the grooves of lead foil sheets, and this structure is repeated layer after layer, with a shift between layers. A module contains two $4 \times 4 \times 262$ cm^3 cells, side by side, and each cell is read out by a PMT at both ends, giving four channels per module and 256 channels in total. The EC is 11 radiation lengths thick in total and has an energy resolution of $\frac{14}{\sqrt{E(\mathrm{GeV})}}\%$, with a linearity better than 10% [78].

5.2.3 The Muon Range Detector (MRD)

Due to the cost of shipping, the decision was made to construct a new MRD on-site, assembled from detector components salvaged from past Fermilab experiments.

The MRD is a sampling calorimeter, with alternating layers of steel and scintillator. There are 12 steel panels at $400 \times 350 \times 5\text{cm}^3$, giving 60 cm of steel. Sandwiched between them are 13 scintillator layers, seven vertical and six horizontal. As can be seen in figure 5.5, a vertical scintillator layer consists of two rows of 15 scintillator panels, with a 2 in PMT attached to the end of each. Each panel is therefore 1.75 m long, 25 cm wide and 1 cm deep. The horizontal layers use fewer panels (two columns of 13), but they are longer at 2 m.

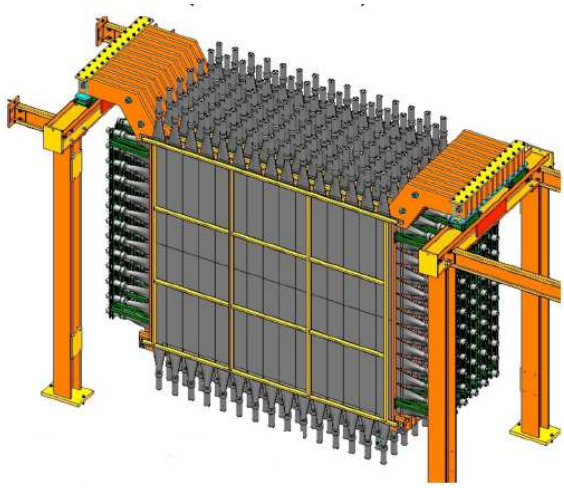

Figure 5.5: The Muon Range Detector is furthest downstream, and measures the direction and energy of muons created in the SciBar. Made from alternating 5 cm thick iron panels and scintillator layers, a muon's energy is determined from how many layers it passes through before stopping.

Due to the procurement method, there are a number of different PMT types. Each PMT type has a different characteristic noise rate, so the types were arranged to limit the chance of reconstructing a track from noise. The PMTs with the highest noise were placed in the same view as the PMTs with the lowest noise, on alternating layers. As a reconstructed MRD track must pass a number of layers, then some hits must come from low noise sensors.

Each PMT in the MRD is connected to its own electronics channel, including an ADC and a TDC. The ADC is set to integrate over the full beam spill, which results in a noise level of approx 20 hits per event, although these are comparatively low charge and a true hit is generally higher. Specifically, hits with a deposit greater than 0.35 MIP (a unit of charge calibrated from cosmic rays) are above the noise threshold. The TDC is a multi-hit design, similar to the SciBar.

The MRD was continuously monitored using cosmic ray muons outside of the beam spill. By measuring the response of the sensors and the electronics, an average efficiency of 99% for selecting real hits was achieved. A tight constraint on time coincidences gave the MRD both high efficiency and purity [71].

5.3 The SciBooNE Software

The purpose of introducing SciBooNE to this thesis is to suggest that the similarities between the detector designs of ND280 and SciBooNE will allow a test of ND280 reconstruction algorithms. Chapter 4 described a Monte Carlo analysis of this reconstruction, and demonstrated high efficiencies for detection and direction reconstruction. However, as the T2K experiment has not yet started taking data, and the beam test of the ND280 ECal will not be until 2009, this validation was completely dependent on the accuracy of the Monte Carlo simulation.

As SciBooNE's SciBar detector is similar in design and construction to the ND280 ECal, it stands to reason that techniques designed for the ECal would also be effective in SciBar. Demonstrating that the algorithms correctly reconstruct particles in SciBar provided evidence that they will be successful in ND280. However, this is only valid if a good agreement between MC and data is simultaneously demonstrated.

The best way to test the algorithms would be to apply them directly to SciBooNE MC and data files, using the ecalRecon package to reconstruct events in SciBar and oaAnalysis methods to quantify the efficiency and the differences between data and MC. However, this is obviously not possible due to the differences in geometry and data format. The rest of the chapter will cover the work required to read the data, including using SciBooNE reconstruction information to provide a 'clean' data sample, and to give ecalRecon a reasonable chance of correctly reconstructing the separate tracks.

5.3.1 Converting the SciBooNE Data into ND280 Format

The SciBooNE data are stored in a similar structure to the ND280 format. Within a specific event, any activity in a channel is stored as a Hit object, containing a coded bar position, charge and time (in both raw ADC/TDC and calibrated forms).

Fortunately, these hits were stored as arrays in a ROOT ntuple, which meant reading the information within the ND280 event structure was relatively simple. Each hit could then be converted into a ND280 THit and added to a new event, separated into three THitSelections, one for each sub-detector.

As explained in section 3.2, a THit only needs three pieces of information: a charge, a time and a geometry node ID (GeoNodeID). The need for charge and time is obvious, and these are copied directly from the SciBooNE hits. The GeoNodeID is a code used by a ROOT geometry to define a specific detector volume, such as a bar of scintillator. This has a number of serious advantages over a simple position for that bar.

As the detector geometry did not change during the SciBooNE experiment, a single ROOT geometry can be used for all three runs. As well as returning the position of each bar, the geometry can also return the orientation of the bar, the physical size or 'spread' of the volume and which end the photosensor is connected to. This method also cuts down on the disk space requirements for the data, as a single integer is stored for each hit, instead of a minimum of three double precision floats.

For this method to work, it was necessary to create a new ROOT geometry, as the SciBooNE collaboration had not used one. This was achieved by rewriting the nd280mc package into 'sciboonemc', describing the whole detector, including the pit, in GEANT. This GEANT geometry is automatically converted to a ROOT geometry, which is used as an input to the 'sciboonedataconverter' package, the final package in the conversion string. The output from sciboonedataconverter is at the same stage of the software string as the output of elecSim, ready to be fed into ecalRecon.

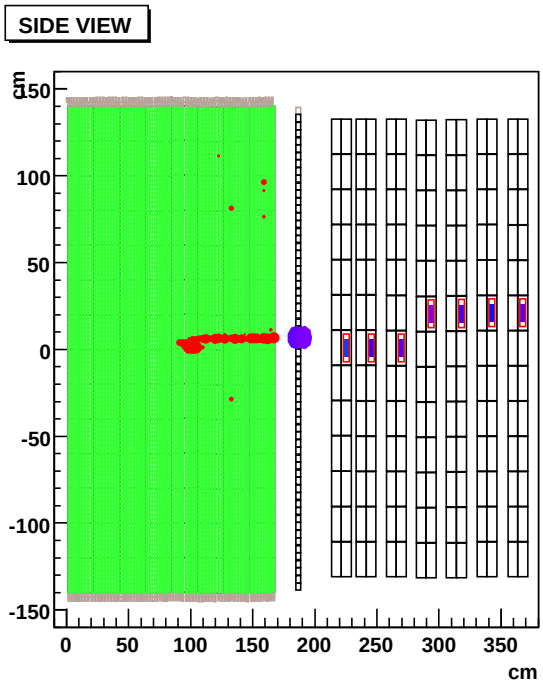

(a) SciBooNE Event Display

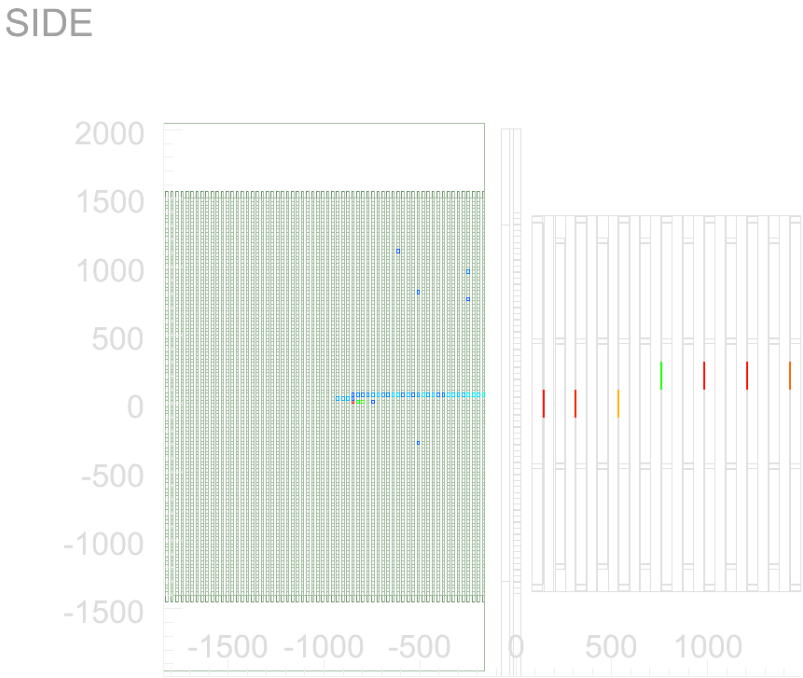

(b) T2K Event Display

Figure 5.6: A SciBooNE Monte Carlo event, shown in both the (a) SciBooNE and (b) T2K event displays.

5.3.2 A 'Clean' Data Sample

The SciBooNE data used were in a '2nd pass' state, which also included some reconstruction information. The reconstruction uses a tracking cellular automaton to find SciBar tracks, and a simple clustering and time-matching method to find MRD tracks. A matching algorithm is then used to determine if any SciBar and MRD tracks were made by the same particle. At the same time, any deposit within the EC is added to a matching track. These global matched objects are then stored as a SciBooNE track.

The SciBar-MRD matched SciBooNE tracks provide a simple way of selecting a clean sample of interesting interactions from the SciBooNE data and MC. An event with a single matched track is almost certain to be a charged current neutrino event with the muon producing the matched track. If ecalRecon can reconstruct a SciBar track which matches the position and direction of the MRD track, then this will be a clear signal of successful muon reconstruction.

The SciBooNE detector was only 7 m below ground level, with no overburden, so the rate of cosmic rays was high. At the same time, neutrino interactions in the pit walls frequently produced muons which passed through the detector. To minimise the effects of these background sources, a series of pre-cuts have been applied to the data and MC. The cuts were based on those used in SciBooNE's first paper, a search for CC coherent pion production, and are explained in detail there [71]. The three cuts are summarised here:

Timing Cut - As with all beam-based neutrino experiments, the timing of the beam gives a tight constraint on cosmic muons. The charge-weighted mean time of the SciBar hits is calculated, and any event that falls outside a 0 µs $< t <$ 2 µs beam window is rejected. By cutting on the beam window the majority of the cosmic backgrounds can be removed, and by looking at a beam-off window (5 µs $< t <$ 15 µs) it is possible to determine the cosmic rate contamination as being only 0.5%.

Number of SciBar-MRD Matched Tracks ≥ 1 - This second cut is intended to select CC events, specifically events with a muon passing from the SciBar to the MRD. This is an essential cut for testing of ecalRecon, as it guarantees the existence of an MRD track to compare to the reconstructed clusters in SciBar. It is also a requirement for the next cut.

Fiducial Volume Cut - To remove events where a cosmic or pit muon has entered the SciBar and then passed into the MRD, a cut is made based on the reconstructed vertex. The vertex is taken as the position of the upstream end of the longest matched track. This is generally fairly accurate, although backwards-going tracks from the true vertex, aligned with the forward-going muon, can confuse the sbcat reconstruction.

Any events where the vertex is in the first two planes of the SciBar are rejected, as there is a high probability that the track is from an external muon. A similar cut is applied to the x and y directions. The final fiducial constraint is for the vertex to be before the last eight layers of the SciBar. This gives enough information for the reconstruction to ensure that the track is forward going from a SciBar vertex, instead of backward going from the EC or MRD, with a second particle producing a forward going muon to create an MRD track.

$$\begin{aligned} -130 \text{ cm} &< x < 130 \text{ cm} \\ -130 \text{ cm} &< y < 130 \text{ cm} \\ 2.62 \text{ cm} &< z < 157.2 \text{ cm} \end{aligned}$$

After applying these cuts, 2.43% of the data events were left, leaving a final sample of 19,317 events, as shown in table 5.2. The percentage loss of the MC events was lower, with 10.72% passing cuts, as the generated neutrino interactions were within the SciBar and normally within the beam window. This was still a large reduction in MC data; however a quick truth analysis (table 5.3) showed that the majority of events were lost either because they did not have a primary muon or because the muon did not pass through the MRD.

Cut	Data	%	MC	%
Full Sample	796481	100.00	277917	100.00
Timing	355839	44.68	269809	97.08
> 0 Matched Tracks	49981	6.28	34674	12.48
Fiducial Volume	19317	2.43	29819	10.72

Table 5.2: The full data and MC sample, and the effects of the SciBooNE pre-cuts.

Taking all CC events as signal, the MC sample after pre-cuts has a purity of 98.0%, with an efficiency of 12.2%. Of the events lost, 92.1% were dropped because they did not leave a reconstructable signal in the MRD.

These events have passed all SciBooNE pre-cuts, and will be used as the initial sample for the analysis of ecalRecon's algorithms. One further cut is applied to the initial sample, a cut necessary for the T2K algorithms to work on the data, which will be explained in section 6.1.

Sample Description with internal divisions	# of Events	Total %	Relative %	Signal Sample
Full MC Sample	277,917	100.00		
Failed Timing Cut	8,108	2.92		
True Time Fails Cut	537		6.62	
True Time Passes Cut	7,571		93.38	✓
Failed Matched Track Count	235,135	84.61		
No Primary Muon	78,610		33.43	
Muon Missed MRD	116,883		49.71	✓
Too Few Hits for MRD Track	76,836		32.67	✓
No Reconstructed SciBar Track	4,424		1.88	✓
Track Matching Failed	4,218		1.79	✓
Vertex Outside of Fiducial Volume	4,855	1.75		
True Vertex Outside FV	4,484		92.36	
True Vertex Inside FV	371		7.64	✓
Passed all SciBooNE Pre-cuts	29,819	10.73		
True Time Fails Cut	57		0.19	
No Primary Muon	371		1.24	
True Vertex Outside FV	174		0.58	
Signal Events Passing Pre-cuts	29,217		97.98	✓

Table 5.3: The efficiency and purity of the SciBooNE pre-cuts, demonstrating the major losses.

Chapter 6

Analysis of SciBooNE Data in the T2K Framework

This chapter will show the effectiveness of the ecalRecon algorithms at reconstructing tracks within real events. After defining some cuts specific to ecalRecon, it demonstrates 100% efficiency at reconstructing the initial muon track that was required for the event to be included in the data sample, with a high degree of accuracy for matching the position and direction to the MRD track.

Other clusters are also reconstructed, and an analysis of the matching MC shows that some come from photons from π^0 decay, providing proof that the ecalRecon methods will work on real data and that the inclusion of noise should not have a large adverse effect when ND280 starts taking data in 2009. At all points, close agreement between MC and data is shown, except in one situation where SciBooNE's reconstruction also sees a discrepancy, which is currently being investigated by the SciBooNE collaboration.

6.1 Adapting ecalRecon to the SciBar Geometry

After using sciboonedataconverter, any data or MC events which passed the SciBooNE pre-cuts are stored in the ND280 format. However, there is still one major

distinction between the data and a similar event in the ND280 detector. The SciBar fulfils two roles, detector and target. The same is true for the FGD regions in ND280, but the tracker ECal sections were designed to be separate sub-detectors, surrounding the target region. As such, ecalRecon was not intended to search for and identify vertices within the ECal, but instead reconstruct and identify individual particles entering the ECal.

As the only problem with the SciBooNE data is the inclusion of the vertex within the data sample, the simplest, and arguably most effective, solution is to remove the offending hits from the data. The SciBooNE reconstruction discussed in the previous chapter provides sufficient information for this adjustment, as it provides a reconstructed vertex within the fiducial volume.

A dead zone is created around this vertex, a 20 cm by 20 cm square in each of the 2D views. This provides the reconstruction with an arrangement more analogous to the tracker ECal, with particles apparently incident on the flat front face of an ECal. Figure 6.1 uses two event display images to show the effect.

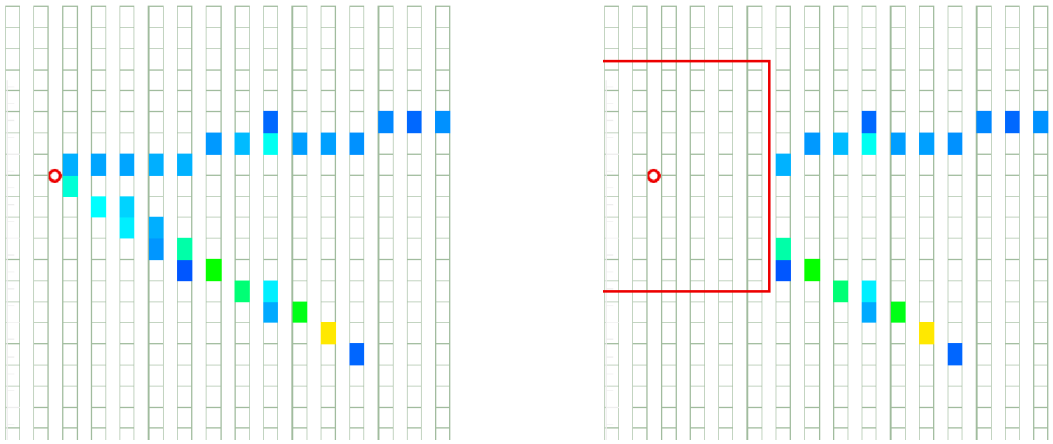

(a) Original situation (b) With the dead zone applied

Figure 6.1: A SciBooNE data event, with a two-pronged signal, most likely a muon and a proton, with the SciBooNE reconstructed vertex as a red circle. In the second image, 10 hits have been removed from a dead zone around the vertex, presenting a situation more analogous to ND280's tracker ECal.

There is still only one detector region, instead of the multiple ECal sections of the tracker ECal, but each particle is more likely to be physically separate from

the others. (This is obviously not guaranteed, as particles may be travelling on trajectories so similar that they are still conjoined after crossing the threshold).

In some circumstances, removing these hits from the sample leaves an event which no longer has sufficient information for a reconstruction. Therefore, a newly constrained fiducial volume is defined, identical in X and Y, but decreased to 145.4 cm in downstream Z. This ensures there are sufficient hits downstream of the dead zone for the ECal algorithms to reconstruct clusters.

The upstream fiducial limit is also increased (to 5.24 cm), as an examination of the reconstructed vertex showed there was still a large discrepancy between MC and data. This can be seen in figure 6.2, specifically 6.2(f), which shows the ratio of data to MC, normalised to 1. The plot clearly shows that there is an excess of 110% in the first layer of SciBar. This excess was not seen in the SciBooNE Coherent Pion paper from which the pre-cuts were taken [71]; however it appears that different versions of the cross-talk simulation and vertex correction methods were used, which would explain the differences [79].

Cut	Data	%	MC	%
'Clean' Sample	19317	100.00	29819	100.00
1 Matched Track	19084	98.79	29486	98.88
Fiducial Volume	17024	88.13	26267	88.09

Table 6.1: The effect of the ecalRecon specific cuts on the data sample.

The only other changes made to the ecalRecon methods was to change geometry-specific values. For example, whilst the physical dimensions were changed, the basic clustering algorithm will still extend to nearest neighbour in the X or Y direction and to next-to-nearest-neighbour in Z.

6.2 Reconstruction of the Primary Muon Track

The next step is to show that the primary muon track is correctly reconstructed. First, the efficiency for reconstructing a cluster from the sample is determined, then the cluster is compared with the MRD track reconstructed by SciBooNE.

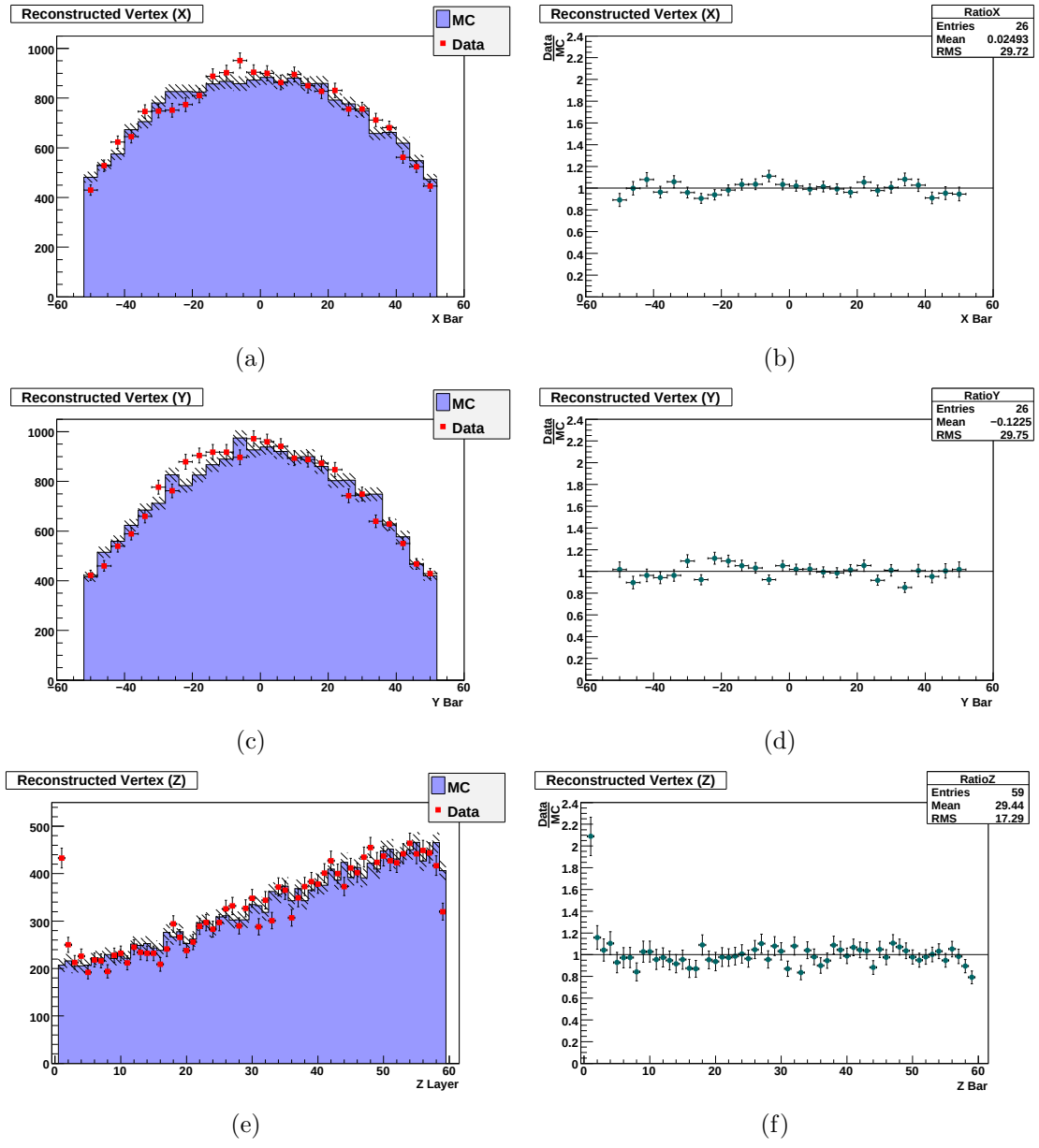

Figure 6.2: The plots compare the reconstructed vertex positions of data and MC events in X, Y and Z. The left plots show the distribution of events, with the MC (blue histogram with hatching showing statistical errors) reweighted to match the data sample, and the right plots show the ratio of data:MC, renormalised to 1.

Figure 6.3: The number of clusters found by ecalRecon, in a sample of events with only a single reconstructed SciBooNE track, matched between the SciBar and the MRD. The logarithmic y scale makes it possible to see that ecalRecon always successfully reconstructed one cluster, and occasionally found others. There is also a good agreement between MC and data.

6.2.1 Locating a Cluster

Figure 6.3 shows the number of clusters reconstructed by ecalRecon, for the situation where SciBooNE had only found a single track. These are assumed to be $\nu + n \rightarrow \mu + p$ events where the proton was too low energy to be reconstructed. The histogram shows both data and MC events, with the MC reweighted with a scaling factor of:

$$\begin{aligned} R_S &= \frac{N_{\text{Data}}}{N_{\text{MC}}} \\ &= \frac{17{,}024}{26{,}267} \\ &= 0.648 \end{aligned} \tag{6.1}$$

where N_{Data} and N_{MC} are the number of events to have passed all SciBooNE pre-cuts and the extra fiducial volume cut. This scaling factor is not related to physics; the original sample of MC is unrelated to the protons on target which provided the data sample.

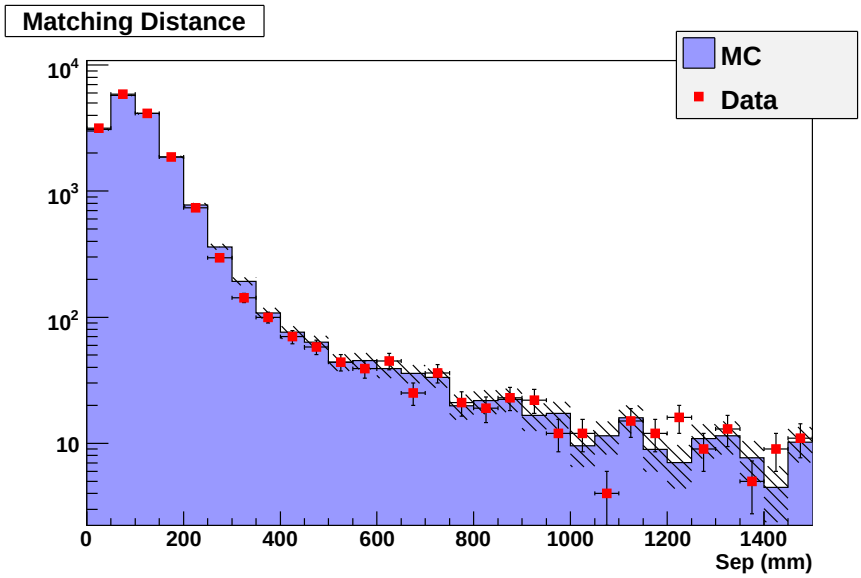

Figure 6.4: The matching of ecalRecon clusters with the MRD tracks reconstructed by SciBooNE. The scintillator panels in the MRD are 25 cm wide, but the SciBooNE reconstruction uses information from multiple layers to produce a fit, improving the resolution. Still, for data (MC), 92.6% (92.1%) of the events match within 25 cm.

6.2.2 Position Matching for Clusters

However, finding one or more clusters is insufficient to say that the muon has been correctly reconstructed. The cluster may have been caused by another particle, or may be only a small part of the full track. To confirm the clustering accuracy, the reconstructed cluster is compared to two variables provided by the SciBooNE reconstructed SciBar-MRD track; the starting point within the MRD and the direction of the MRD track.

Figure 6.4 shows the distance of the ecalRecon expanded cluster from the MRD track. The cluster direction and position is calculated from a charge-weighted principal component analysis, and the trajectory is extrapolated into the MRD, where it is compared to the track start position. As no matching has been attempted between the XZ and YZ views, each view is considered separately and all clusters in the view are considered, with the closest match being recorded. The figure shows $R = \sqrt{(\Delta X)^2 + (\Delta Y)^2}$.

6.2.3 Direction Matching of Clusters

Figure 6.5 shows six plots, related to the direction reconstruction of the ecalRecon clusters. The upper two plots compare the angle of the cluster to the angle of the MRD track, projected into the same XZ or YZ view. If there are multiple clusters in a view, the cluster which best matched to the location is used. The angle plotted is given by:

$$\theta = \theta_{\text{SciBar}} - \theta_{\text{MRD}}$$

where θ_{SciBar} is the angle of the cluster produced by ecalRecon in the SciBar and θ_{MRD} the angle in the MRD, from SciBooNE's reconstruction, both measured against the Z axis. A difference can be seen between the data and MC at this point, with the data distribution tending to a higher value.

Plots (c) and (d) show the distribution of θ_{SciBar} and (e) and (f) show θ_{MRD}. Interestingly, plots (e) and (f) are independent of ecalRecon algorithms, showing the angular distribution of the reconstructed MRD tracks, and they also show a discrepancy between data and MC results, with real muons seeming to be produced at greater angles than the MC had predicted. The SciBooNE collaboration's analysis of the muon angles is ongoing, however it appears likely that this is a genuine physical difference between MC simulations and data events.

However, this does not fully explain the discrepancy in the matching angle. An understanding of the difference also requires the realisation that the angular reconstruction is dependent on the angle of incidence. Figure 6.6 shows that as the angle of the track increases, the SciBar track tends to have a higher reconstructed angle than the MRD track (both the MRD and SciBar geometries are better optimised for lower angles). Combined, these effects explain the data/MC discrepancy observed in figure 6.5 (a) and (b).

6.3 Reconstructing Clusters from Other Particles

The previous section should show that the ECal reconstruction algorithms written for ND280 have successfully reconstructed muon tracks in the SciBar, a detector

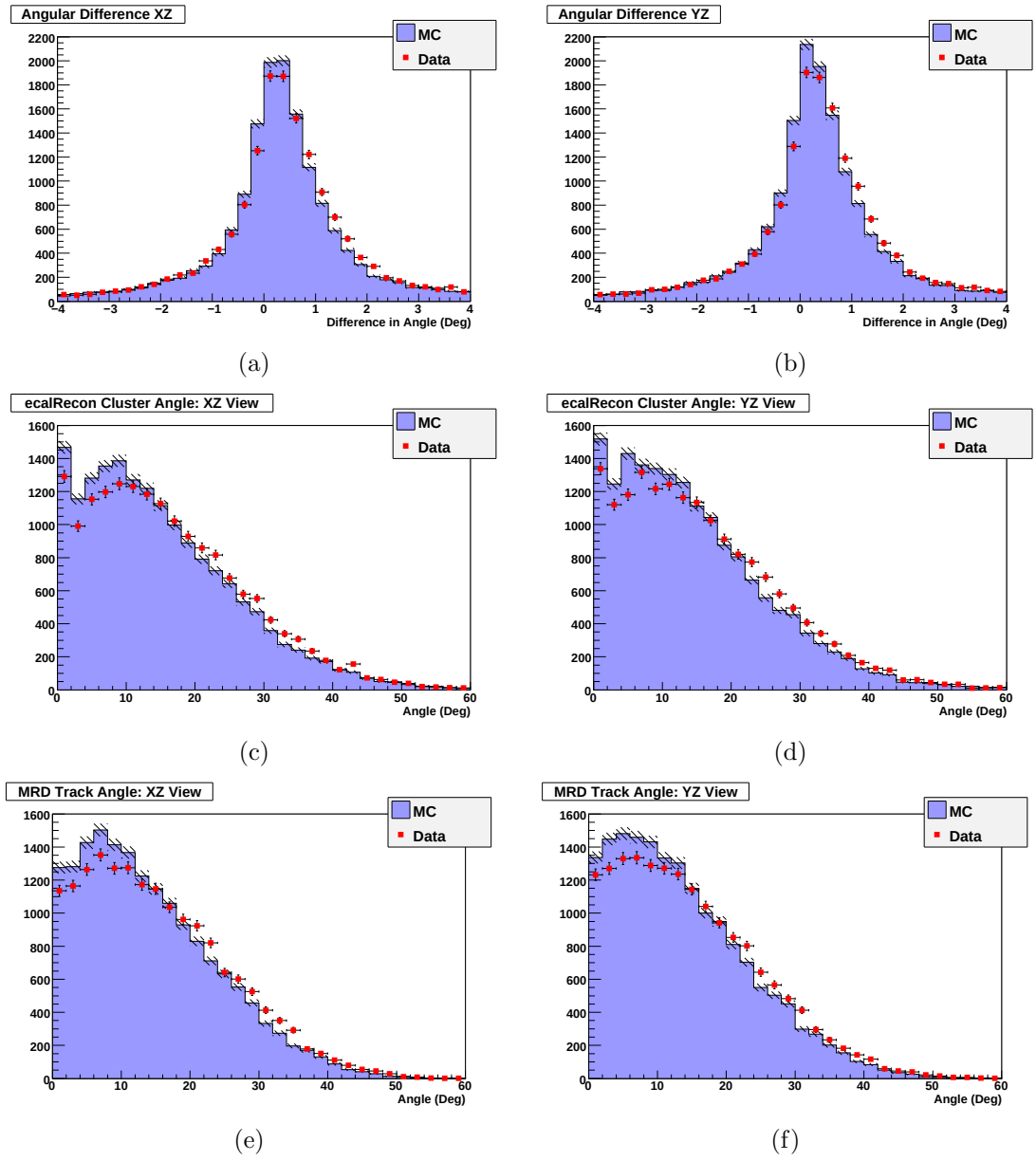

Figure 6.5: Figures (a) and (b) show the difference in reconstructed angle between the SciBar clusters and MRD tracks, as explained in the text. Figures (c) through (f) are included to demonstrate that the differences between data and MC are observed at a more fundamental level; the SciBar cluster reconstructed by ecalRecon and the matched SciBar-MRD track from SciBooNE. It can be clearly seen that muons from data are more likely to be at a higher angle than the MC predicted.

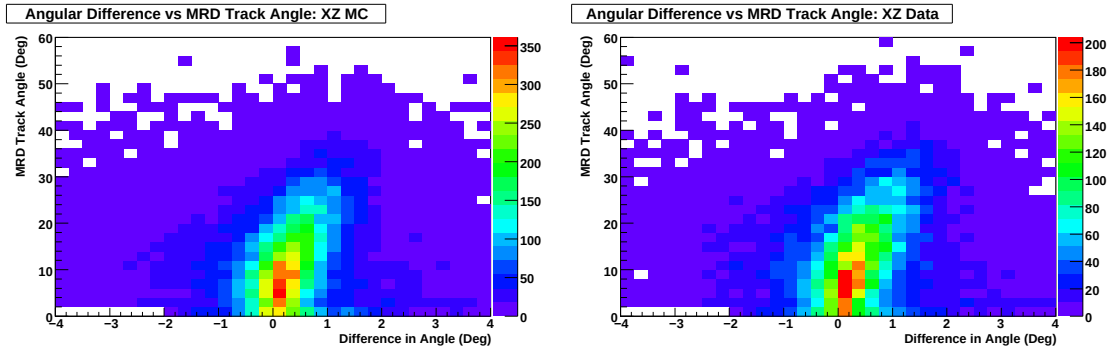

(a) (b)

Figure 6.6: Plots showing the difference in angle between the reconstructed SciBar and MRD tracks (as in the first two plots of figure 6.5), but now displayed against the varying MRD angle. It can be seen that the mean difference increases with MRD angle (only the XZ view is shown, as the YZ view shows the same trend).

with a similar design to the ECals (albeit with a better granularity and no lead). As well as recording the existence of a muon track, they also successfully projected the cluster forward and matched it with the position and direction of a known muon track in the MRD.

However, chapter 4 demonstrated the ECal's capabilities at reconstructing particles that were not MIP-like, specifically photons. As the clusters found in section 6.2 were all matched to MRD tracks, they are certainly caused by MIPs, and do not prove that other particle types have been observed.

Figure 6.3 demonstrated that in about 10% of the events where SciBooNE had reconstructed one track, ecalRecon had found two or more. Whilst these clusters may have been from distinct particles, this is not conclusive. Instead, they could be component clusters of the full track left by the MIP.

Therefore, to demonstrate the success of ecalRecon, the analysis is extended to all SciBooNE events that passed the cuts described in section 6.1. Firstly, the number of clusters reconstructed is investigated with respect to the primary particles produced in the SciBooNE MC. Secondly, the direction of the reconstructed clusters is considered, specifically how well they match the suspected vertex, reconstructed by SciBooNE.

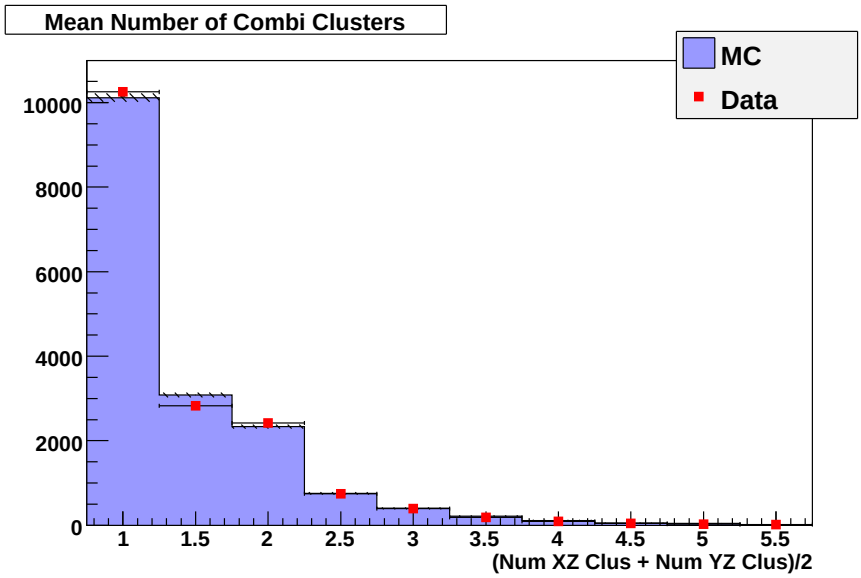

Figure 6.7: The number of clusters reconstructed by ecalRecon. The plots have been scaled using the scaling factor in section 6.1. As the reconstruction produces 2D clusters in two views, the mean number of clusters is plotted, so that the number best matches the number of SciBar tracks from the SciBooNE reconstruction.

6.3.1 Multiple Cluster Reconstruction

Figures 6.7 and 6.8 show four plots, displaying the number of clusters produced by the ecalRecon package. Figure 6.7 shows the full data and MC samples, and shows fairly good agreement. There is a slight indication that the 1 cluster bin is high for data and the 1.5 bin is low, at about the 3σ level.

As the major difference between the data and MC is the lack of noise simulation in the MC, the likely explanation is that for events where two tracks leave the vertex at similar angles, they may not be separated after leaving the dead zone. A noise hit in the space between tracks would increase the probability of them being conjoined into a single reconstructed cluster. The same situation in ND280 is less likely, as the vertex will be further from the ECal front face.

The further three plots (6.8(a) – 6.8(c)) split events from the first plot between three categories, corresponding to 1, 2 and > 2 SciBar tracks found by SciBooNE. In each, a peak can be found at the expected number of clusters, but there is a probability that the two reconstructions disagree.

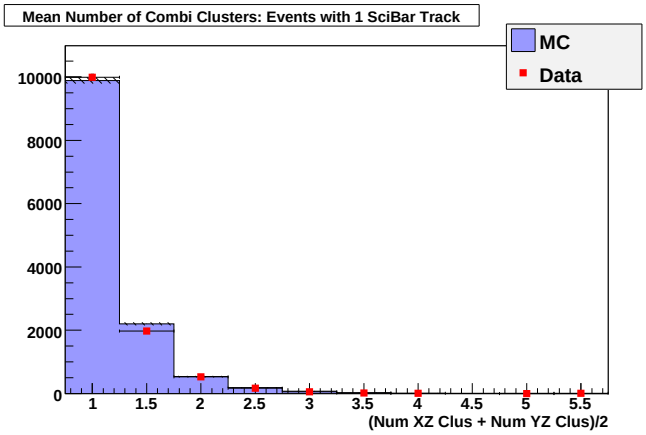

(a)

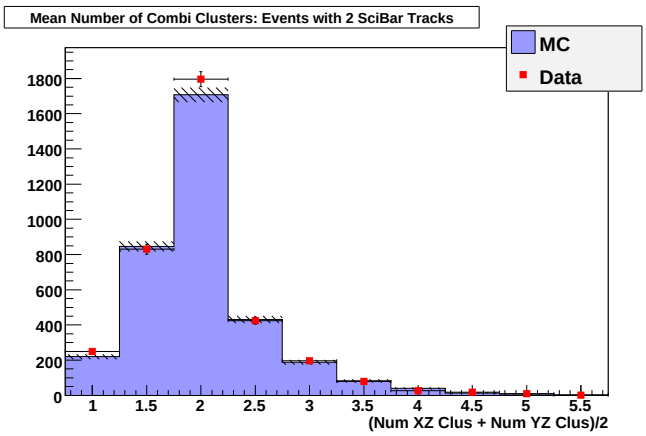

(b)

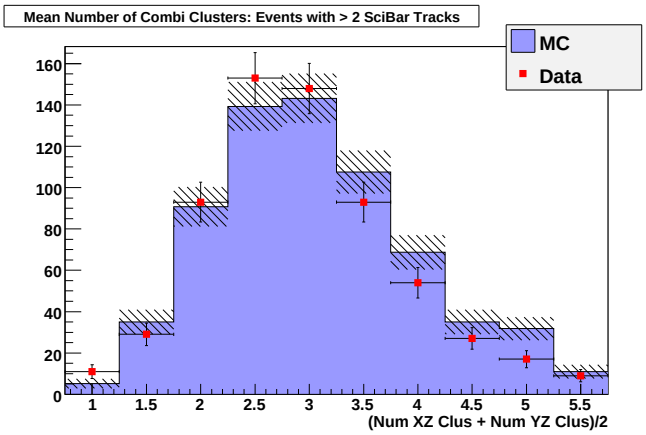

(c)

Figure 6.8: The number of clusters reconstructed by ecalRecon, separated based on the number of tracks reconstructed by the SciBooNE reconstruction, showing the selections where the SciBooNE reconstruction found 1, 2 or > 2 tracks.

This is to be expected, due to the different design strategies of the methods. There are a number of explanations for both an excess and a deficit of ecalRecon tracks. One example for a deficit was outlined above, while others include tracks which barely left the dead zone, giving insufficient hits for ecalRecon, or the splitting of tracks away from the vertex, a scenario that sbcat was designed to consider.

An excess of clusters could be caused by a failure of the ecalRecon methods, with one track split into a number of clusters; however the high granularity of the SciBar and the lack of lead make this less likely. Another scenario is ecalRecon correctly reconstructing objects that are not particularly track-like. This stage of the SciBooNE reconstruction concentrates on tracks, so photon showers or small clusters from primary neutrons are often missed.

6.3.2 Matching Clusters to the Reconstructed Vertex

The ecalRecon process has worked on the assumption that the neutrino interaction vertex is known from the SciBooNE reconstruction. Whilst there is a chance that this reconstruction was incorrect, and the vertex was elsewhere in the detector, MC suggests that 85% of events fall within 25 mm, comparable to the size of a single bar.

It is therefore interesting to determine how well the clusters found in the previous section match with the vertex. Figure 6.9 shows the minimum separation between the projected trajectory of a cluster and the reconstructed vertex, over two distance scales. The shorter distance shows that the main peak is well below the width of a bar, which provides the resolution for the vertex reconstruction.

The longer distance plot is displayed on a logarithmic scale, and shows two interesting effects. Firstly, in the tail of the distribution the incorrectly reconstructed vertices account for approximately 50% of the events, making the comparison invalid. The remainder of the events are likely to be small clusters from photons or neutrons, which travel a short distance and leave small deposits, with insufficient shape definition for a reasonable direction to be reconstructed.

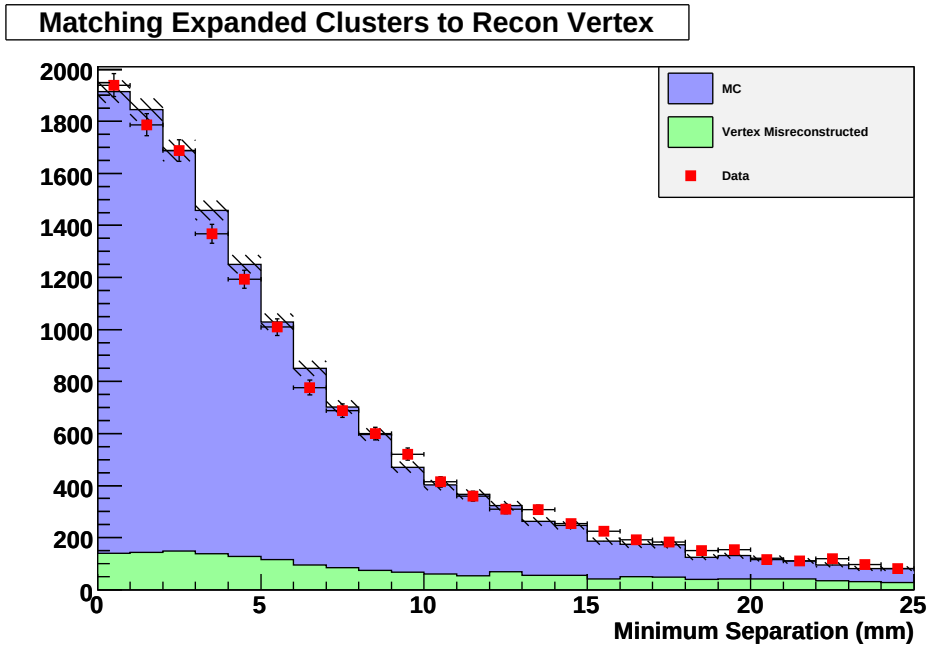

(a)

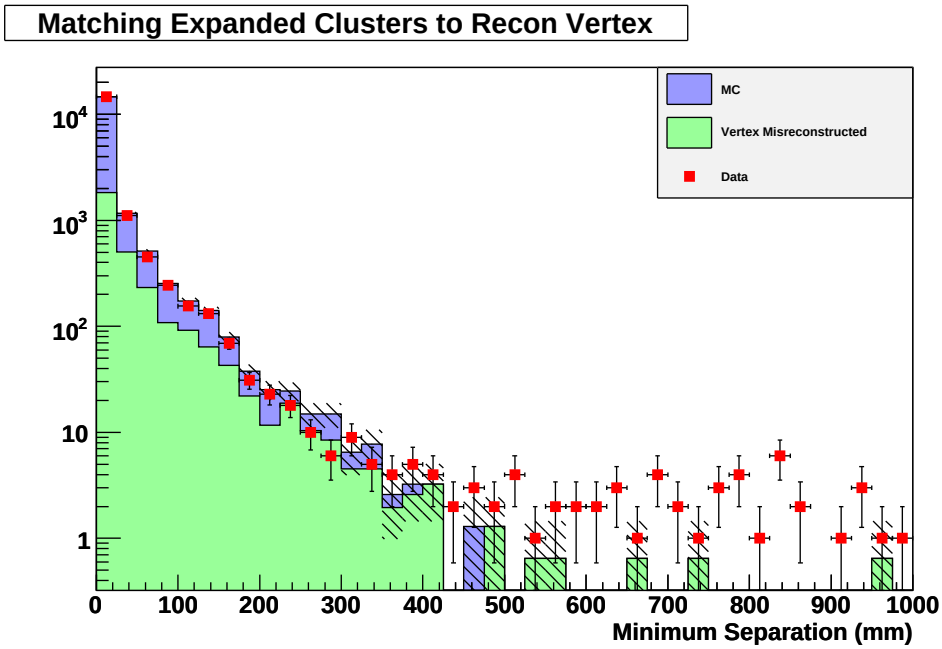

(b)

Figure 6.9: The matching of clusters reconstructed by ecalRecon to the vertex provided by the SciBooNE reconstruction. The plots show two distance scales, 0 – 25 mm for the first, and 0 – 1000 mm for the second. The first range corresponds to the first bin in the second. The smaller green distribution shows events with a misreconstructed vertex.

The second point of interest is an excess of data clusters at higher distances. The excess is small, but clearly visible and genuine. A suggested explanation for these events is that they are particles from other neutrino interactions in the dirt or cosmic rays. As they would be disassociated from the reconstructed muon that triggered the event, there would be no reason for them to point to the vertex, and they would provide a small percentage of clusters overlaying the normal distribution.

6.3.3 Considering Primary Charged Particles and Neutral Pions

The majority of the events with a single track in SciBar are expected to be CCQE interactions, where the μ^- produces the track through the MRD and the proton has insufficient energy to produce a recordable track. An examination of the MC events suggests that the threshold for the proton to produce its own track would be approx 500 MeV. Whilst there is no guarantee that a proton above 500 MeV will produce a track, one below the threshold is unlikely to be detected. In a similar way, the threshold for charged mesons (predominantly $\pi^{\pm}$ in neutrino interactions) is roughly 200 MeV.

Therefore, in MC only, it is possible to consider the likely number of tracks produced by charged primary particles. The distribution of neutral particles leaving the vertex is also known, but it is more difficult to predict the deposits left by them. For a high energy π^0, it is likely that both of the decay photons would have enough energy to create a shower, but it is not guaranteed that these will be within the SciBar detector. For a π^0 with lower energy, an asymmetric distribution of that energy between the photons may lead to one visible shower only.

Figure 6.10(a) shows the same plot as figure 6.7, but the MC histogram has been split into a stacked format, with nine categories. These are the combinations of two independent groups of three. Firstly, the number of observable primary charged particles (1, 2 or > 2)

$$\text{VisibleChargedParticles} = \text{Muons} + \text{Protons}_{E>500} + \text{ChargedMesons}_{E>200}$$

and secondly, the number of neutral pions (0, 1 or > 1).

The second figure 6.10(b) shows the same information, but each bin has been renormalised to 100%. The plots show a clear increase in clusters in events with 1 or more neutral pions (starting at 2.5 clusters), in comparison to events where the number of other detectable particles is unchanged.

The same increase can be seen clearly in the two plots in figure 6.11. In the first plot, events with a single visible charged particle (VCP) have been selected, and the mean number of clusters is displayed. The dashed red line shows events without a π^0 and has a strong peak at 1, with only a small tail. In comparison, the distribution of events with a π^0 (the solid blue line), has a significantly higher mean. The second plot shows events with two VCPs, and shows the same trend.

The two sets of figures provide a clear signal that the reconstruction is correctly clustering photons from the pion decays. Naively, one might expect to see an extra 2 clusters for each π^0 event, but this is made impossible by the SciBar geometry. The lack of absorber in the SciBar (which has been added to detectors like the ND280 ECal or P0D for this reason) means that many photons leave the SciBar without showering, therefore the small increase in clusters observed, including a significant proportion of events where no extra signal is seen, is exactly what would be expected.

6.4 A Summary of Results

The SciBooNE data has proven invaluable for testing the ecalRecon methods and algorithms. The sample of events with a known MIP track in the MRD provide a clean test of muon reconstruction, demonstrating a high efficiency for detecting particles of reasonable energy.

Other charged particles, such as protons and charged pions, are also seen to be reconstructed, both with reasonable efficiency and good position and direction resolutions, which will be vital for correctly matching TPC or FGD tracks to ECal clusters in T2K's 280 m detector.

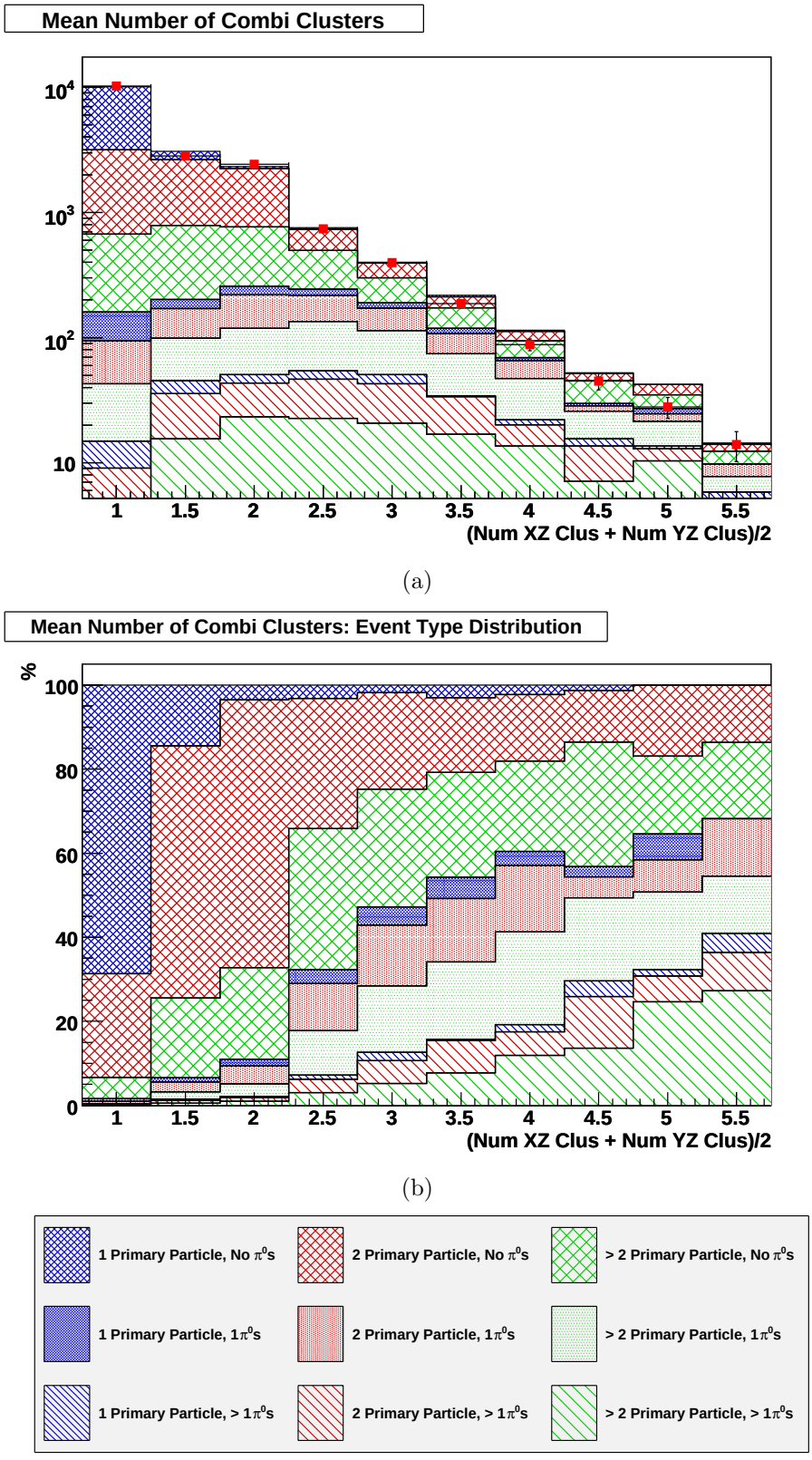

Figure 6.10: The number of clusters reconstructed by ecalRecon, divided into categories based on the number of primary particles, as explained in the text. The second plot has the same data as the first, but each bin has been renormalised to 100%, to show the varying composition.

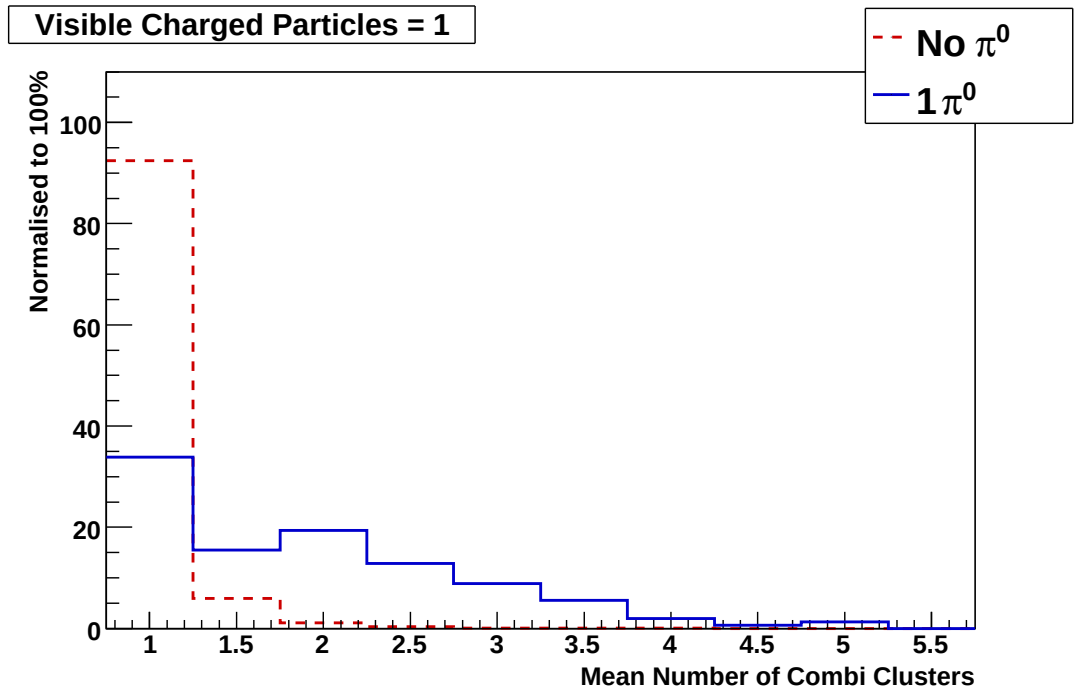

(a) 1 Visible Charged Particle

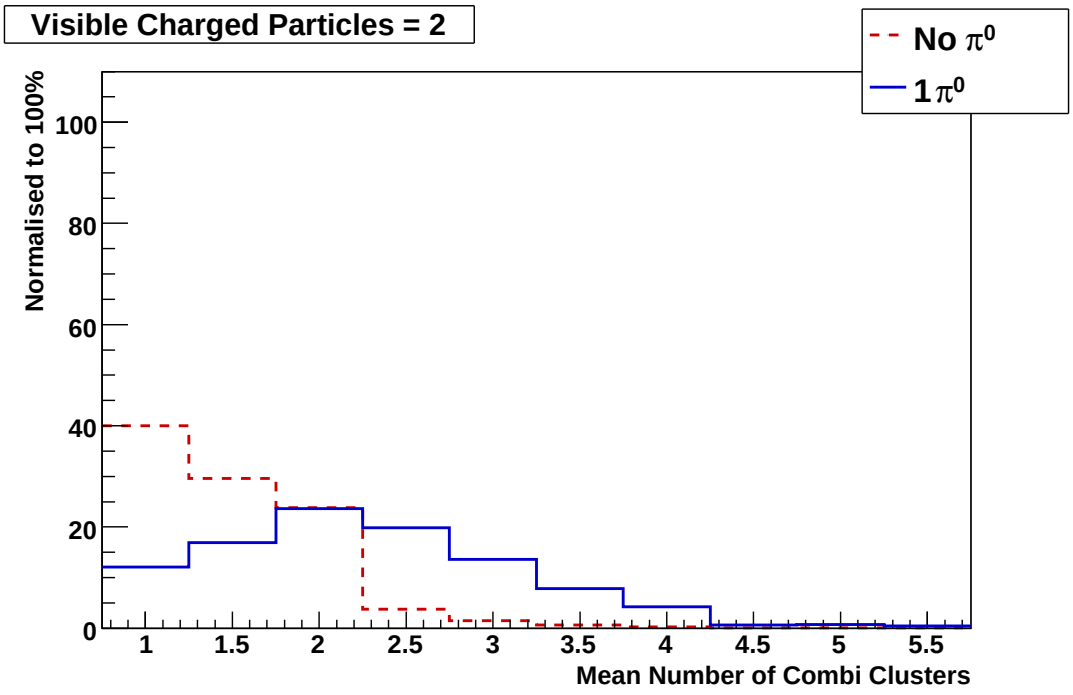

(b) 2 Visible Charged Particles

Figure 6.11: The two plots show the mean number of clusters found in events with 1 and 2 VCPs, split between events with a π^0 (solid blue line) and those without (dashed red line). Each sample has been normalised to a total of 100%. Whilst the information comes from MC only, a good agreement between MC and data has been confirmed. The extra clusters observed in π^0 events are a clear sign of the reconstruction of photon showers in the SciBar.

Also, the reconstruction of photons has been demonstrated. This is probably the only measurement attempted that is more difficult in the SciBar than it will be in the ND280 ECal (the ECal was designed specifically for stopping photons and recording their energy), but a clear signal is still seen. This is a promising result for T2K, as the measurement of photons, and hence the neutral pion cross-sections, will be vital for understanding the backgrounds of the ν_e appearance measurement.

Finally, it has been shown that the results for data and MC are in good agreement. Discrepancies were only seen in two instances; the first is believed to be a genuine physics difference, which is being investigated by the SciBooNE collaboration, and the second is a small effect which can be explained by the lack of noise simulation in the MC. This is the only point where differences are seen due to noise; in all other situations the reconstruction algorithms are shown to be robust against the addition of noise.

Chapter 7

Conclusions

This thesis has described the ND280 tracker ECals and the software written to reconstruct and analyse particle tracks and showers within them. These reconstructed particle objects will be used in all of the measurements made by the ND280 tracker; which was designed with the goal of measuring the neutrino beam flux, the background cross-sections and the ν_e contamination in the beam.

The ECal is expected to reconstruct the position and direction of any particle crossing it, and contains layers of lead to ensure that particles such as photons shower within the detector volume and do not pass undetected. After detecting a particle, PID and energy reconstruction methods will be used to categorise it, before passing the reconstructed object to the global ND280 analysis, but all stages rely on the initial success and completeness of the clustering algorithms.

Using a Monte Carlo analysis, it was shown that the algorithms have a high efficiency for clustering particles with a reasonable amount of energy. 90% of muon tracks over 100 MeV were correctly reconstructed as 1 cluster in each 2D view, containing 90% or more of the hits left by the muon. The majority of events which failed the cut did so because tracks had been split into 2 clusters, often only in 1 view. Muons at lower energies were clustered with varying efficiency, but below 50 MeV only 5% were leaving a large enough deposit for a reconstruction to be possible.

The efficiency for photons was generally lower than for muons, which was expected due to the increased difficulty of reconstructing electromagnetic showers. Photons or electrons of more than 250 MeV are reconstructed with high efficiency. However, the majority of photons from π^0 decays, which are the ones of greatest interest, will be lower energy. Approximately 50% of them will be reconstructed by the first pass of the reconstruction, but later algorithms in the reconstruction or analysis will be able to use ecalRecon as a basis, using different algorithms which increase efficiency by making assumptions about the event.

This analysis was carried out completely in MC (since the ND280 ECal will not be installed at Tokai until September 2009) and therefore relies on the accuracy of the simulation. In order to work around this dependency, data from the SciBooNE experiment were examined within the same framework. After converting both data and MC events from the SciBooNE experiment into the ND280 format, the ecalRecon methods were applied to a clean data sample.

The sample was selected based on the existence of at least one known MIP track, passing through both the SciBar and MRD detectors. The ecalRecon algorithms had 100% efficiency for independently reconstructing this track in both views, with a good resolution of position and direction, determined by matching it to the known MRD track. Other clusters were also reconstructed, the number of which was compared to the number of tracks found by SciBooNE and the number of primary particles in the MC. Both comparisons showed a good efficiency for charged track finding, with a good agreement between rates for MC and data.

The agreement between MC and data is especially important because of the lack of accurate noise simulation in both the SciBooNE and ND280 Monte Carlos. The absence of major discrepancies shows that the ECal reconstruction methods will still be effective on ND280 data, where there is an expected noise rate of 1% at the double photo-electron level, smaller than the rate observed in SciBooNE.

MC events with primary π^0 were shown to have a higher average number of clusters than similar events without. As the majority of photons do not leave a shower in the SciBar, but instead interact in the EC or escape into the detector hall, this is a strong signal that photons interacting in the SciBar were being reconstructed.

References

[1] G. Danby *et al.*, "Observation of High-Energy Neutrino Reactions and the Existence of Two Kinds of Neutrinos," *Phys. Rev. Lett.* **9** (1962) 36–44.

[2] **KARMEN** Collaboration, K. Eitel *et al.*, "The search for neutrino oscillations $\bar{\nu_\mu} \to \bar{\nu_e}$ with KARMEN," *Nucl. Phys. Proc. Suppl.* **77** (1999) 212–219, arXiv:hep-ex/9809007.

[3] **LSND** Collaboration, C. Athanassopoulos *et al.*, "Evidence for $\nu_\mu \to \nu_e$ neutrino oscillations from LSND," *Phys. Rev. Lett.* **81** (1998) 1774–1777, arXiv:nucl-ex/9709006.

[4] **The MiniBooNE** Collaboration, A. A. Aguilar-Arevalo *et al.*, "A Search for electron neutrino appearance at the $\Delta m^2 \sim 1\text{eV}^2$ scale," *Phys. Rev. Lett.* **98** (2007) 231801, arXiv:0704.1500 [hep-ex].

[5] **K2K** Collaboration, S. H. Ahn *et al.*, "Detection of Accelerator-Produced Neutrinos at a Distance of 250 km," *Phys. Lett.* **B511** (2001) 178–184, arXiv:hep-ex/0103001.

[6] **MINOS** Collaboration, P. Adamson *et al.*, "Measurement of Neutrino Oscillations with the MINOS Detectors in the NuMI Beam," *Phys. Rev. Lett.* **101** (2008) 131802, arXiv:0806.2237 [hep-ex].

[7] **NOvA** Collaboration, D. S. Ayres *et al.*, "NOvA proposal to build a 30-kiloton off-axis detector to study neutrino oscillations in the Fermilab NuMI beamline," arXiv:hep-ex/0503053.

[8] **Particle Data Group** Collaboration, C. Amsler *et al.*, "Review of particle physics," *Phys. Lett.* **B667** (2008) 1.

[9] A. D. Sakharov, "Violation of CP Invariance, c Asymmetry, and Baryon Asymmetry of the Universe," *Pisma Zh. Eksp. Teor. Fiz.* **5** (1967) 32–35.

[10] Y. Hayato, "NEUT," *Nucl. Phys. Proc. Suppl.* **112** (2002) 171–176.

[11] G. Mitsuka, "NEUT," *AIP Conf. Proc.* **981** (2008) 262–264.

[12] **T2K** Collaboration, "T2K ND280 Conceptual Design Report." T2K Internal Document, November, 2005.

[13] W. Pauli, "Dear radioactive ladies and gentlemen," *Phys. Today* **31N9** (1978) 27.

[14] F. Reines and C. L. Cowan, "The neutrino," *Nature* **178** (1956) 446–449.

[15] I. Licata, "Majorana impact on contemporary physics," *Elec. J. Theor. Phys.* **3** (2006) 1–10.

[16] **DONUT** Collaboration, K. Kodama *et al.*, "Observation of tau-neutrino interactions," *Phys. Lett.* **B504** (2001) 218–224, `arXiv:hep-ex/0012035`.

[17] J. Davis, Raymond, D. S. Harmer, and K. C. Hoffman, "Search for neutrinos from the sun," *Phys. Rev. Lett.* **20** (1968) 1205–1209.

[18] C. Pena-Garay and A. Serenelli, "Solar neutrinos and the solar composition problem," `arXiv:0811.2424 [astro-ph]`.

[19] **KAMIOKANDE-II** Collaboration, K. S. Hirata *et al.*, "Results from one thousand days of real-time, directional solar-neutrino data," *Phys. Rev. Lett.* **65** (1990) 1297–1300.

[20] **SNO** Collaboration, Q. R. Ahmad *et al.*, "Direct evidence for neutrino flavor transformation from neutral-current interactions in the Sudbury Neutrino Observatory," *Phys. Rev. Lett.* **89** (2002) 011301, `arXiv:nucl-ex/0204008`.

[21] Z. Maki, M. Nakagawa, and S. Sakata, "Remarks on the unified model of elementary particles," *Prog. Theor. Phys.* **28** (1962) 870.

[22] B. Pontecorvo, "Neutrino experiments and the question of leptonic-charge conservation," *Sov. Phys. JETP* **26** (1968) 984–988.

[23] **SNO** Collaboration, B. Aharmim *et al.*, "Electron energy spectra, fluxes, and day-night asymmetries of B-8 solar neutrinos from the 391-day salt phase SNO data set," *Phys. Rev.* **C72** (2005) 055502, `arXiv:nucl-ex/0502021`.

[24] **Super-Kamiokande** Collaboration, Y. Ashie *et al.*, "Evidence for an oscillatory signature in atmospheric neutrino oscillation," *Phys. Rev. Lett.* **93** (2004) 101801, `arXiv:hep-ex/0404034`.

[25] **K2K** Collaboration, Y. Oyama, "K2K (KEK to Kamioka) neutrino oscillation experiment at KEK-PS," `hep-ex/9803014`.

[26] T. Ishia, "Neutrino and Other Beam Lines at J-PARC,". Particle Accelerator Conference PAC07 25-29 Jun 2007, Albuquerque, New Mexico.

[27] Accelerator Group, JAERI/KEK Joint Project Team, "Accelerator Technical Design Report for J-PARC," tech. rep., Japan Atomic Energy Research Institute, JAERI, and High Energy Accelerator Research Organization, KEK, 2003.

[28] I. Sugai *et al.*, "Development of thick hybrid-type carbon stripper foils with high durability at 1800-K for RCS of J-PARC," *Nucl. Instrum. Meth.* **A561** (2006) 16–23.

[29] T. Sekiguchi, "T2K horn," *AIP Conf. Proc.* **981** (2008) 345–347.

[30] Y. Fukuda *et al.*, "The Super-Kamiokande detector," *Nucl. Instrum. Meth.* **A501** (2003) 418–462.

[31] **Super-Kamiokande** Collaboration, Y. Fukuda *et al.*, "Evidence for oscillation of atmospheric neutrinos," *Phys. Rev. Lett.* **81** (1998) 1562–1567.

[32] C. Yanagisawa and T. Kato, "Report on the Super-Kamiokande accident (November 22, 2001)." Can be found at `http://superk.physics.sunysb.edu/nngroup/publication_theses/SKaccident.ps`.

[33] C. Yanagisawa, "Report on the Super-Kamiokande accident II (January 31, 2002)." Can be found at `http://superk.physics.sunysb.edu/nngroup/publication_theses/SKaccident02.ps`.

[34] R. Becker-Szendy *et al.*, "IMB-3: A Large water Čerenkov detector for nucleon decay and neutrino interactions," *Nucl. Instrum. Meth.* **A324** (1993) 363–382.

[35] W. W. M. Allison and P. R. S. Wright, *Experimental Techniques in High Energy Physics*, ch. The Physics of Charged Particle Identification. Addison-Wesley, 1987.

[36] Y. Takeuchi, "Low-energy neutrino observation at Super-Kamiokande-III," *J. Phys. Conf. Ser.* **120** (2008) 052008.

[37] **T2K** Collaboration, "A letter of intent to extend T2K with a detector 2 km away from the J-PARC neutrino source." Submitted to the J-PARC PAC, June, 2007.

[38] **UA1** Collaboration, M. Barranco-Luque *et al.*, "The Construction of the Central Detector for an Experiment at the CERN anti-p p Collider," *Nucl. Instr. Meth.* **176** (1980) 175.

[39] **NOMAD** Collaboration, J. Altegoer *et al.*, "The NOMAD experiment at the CERN SPS," *Nucl. Instrum. Meth.* **A404** (1998) 96–128.

[40] Taking $F = q(\boldsymbol{v} \times \boldsymbol{B})$ from Maxwell's equations and $F_c = mv^2/R$ as the equivilant centripetal force, we arrive at $v = qBR/m$.

[41] **T2K** Collaboration, T. Lux, "A TPC for the near detector at T2K," *J. Phys. Conf. Ser.* **65** (2007) 012018.

[42] **T2K** Collaboration, M. Di Marco, "Test-bench for the characterization of MicroMegas modules for the T2K ND280 TPC," *J. Phys. Conf. Ser.* **65** (2007) 012019.

[43] **T2K UK** Collaboration, D. Wark *et al.*, "UK Contributions to the T2K Experiment: Case for Support," 2006.

[44] A. Vacheret, M. Noy, M. Raymond, and A. Weber, "First results of the Trip-t based T2K front end electronics performance with GM-APD," *PoS* **PD07** (2006) 027.

[45] C. Bouchiat and L. Michel, "Theory of mu-Meson Decay with the Hypothesis of Nonconservation of Parity," *Phys. Rev.* **106** (1957) 170–172.

[46] D.-E. Groom, "Atomic and Nuclear Properties of Materials," 2007. Available at `http://pdg.lbl.gov/2007/AtomicNuclearProperties/index.html`.

[47] A. Pla-Dalmau, A. D. Bross, and V. V. Rykalin, "Extruding plastic scintillator at Fermilab,". FERMILAB-CONF-03-318-E.

[48] J. B. Birks, "Scintillations from Organic Crystals: Specific Fluorescence and Relative Response to Different Radiations," *Proc. Phys. Soc.* **A64** (1951) 874–877.

[49] M. Hirschberg, R. Beckmann, U. Brandenburg, H. Brueckmann, and K. Wick, "Precise measurement of Birks kB parameter in plastic scintillators," *IEEE Trans. Nucl. Sci.* **39** (1992) 511–514.

[50] **MINERvA** Collaboration, A. Pla-Dalmau, A. D. Bross, V. V. Rykalin, and B. M. Wood, "Extruded plastic scintillator for MINERvA,". To appear in the proceedings of 2005 IEEE Nuclear Science Symposium and Medical Imaging Conference, El Conquistador Resort, Puerto Rico, 23-29 Oct 2005.

[51] A. Vacheret, M. Noy, M. Raymond, and A. Weber, "First results of the Trip-t based T2K front end electronics performance with GM-APDs," in *International Workshop on new Photon-Detectors*. June, 2007. PoS(PD07)027.

[52] F. Retière, on behalf of the T2K ND280 FGD group, "Using MPPCs for T2K Fine Grain Detector," in *International Workshop on new Photon-Detectors*. June, 2007. PoS(PD07)017.

[53] P. Baron *et al.*, "AFTER, an ASIC for the readout of the large T2K time projection chambers," *IEEE Nucl. Sci. Symp. Conf. Rec.* **3** (October, 2007) 1865–1872.

[54] F. Retière. Personal communication, June, 2008.

[55] R. Brun and F. Rademakers, "ROOT: An object oriented data analysis framework," *Nucl. Instrum. Meth.* **A389** (1997) 81–86. See `http://root.cern.ch/`.

[56] C. Arnault, "CMT: A software configuration management tool,". Prepared for International Conference on Computing in High- Energy Physics and Nuclear Physics (CHEP 2000), Padova, Italy, 7-11 Feb 2000.

[57] L. Lonnblad, "CLHEP: A project for designing a C++ class library for high-energy physics," *Comput. Phys. Commun.* **84** (1994) 307–316.

[58] **GEANT4** Collaboration, S. Agostinelli *et al.*, "GEANT4: A simulation toolkit," *Nucl. Instrum. Meth.* **A506** (2003) 250–303.

[59] J. Allison *et al.*, "Geant4 developments and applications," *IEEE Trans. Nucl. Sci.* **53** (2006) 270.

[60] D. Casper, "The nuance neutrino physics simulation, and the future," *Nucl. Phys. Proc. Suppl.* **112** (2002) 161–170, `arXiv:hep-ph/0208030`.

[61] E. A. Hawker, "NUANCE at MiniBooNE," *Nucl. Phys. Proc. Suppl.* **139** (2005) 260–265.

[62] C. Andreopoulos, "The GENIE universal, object-oriented neutrino generator," *Nucl. Phys. Proc. Suppl.* **159** (2006) 217–222.

[63] The T2K ND280 Software Working Group, "ND280 Software Reference," July, 2008. `http://superk.physics.sunysb.edu/~mcgrew/t2k/nd280Doc/v1r0/dox/nd280SoftwareReference.html`.

[64] T. L. Phouc. Personal communication, 2009.

[65] P. Hough, "Method and means for recognizing complex patterns." US Patent 3069654, December, 1962.

[66] **SciBooNE** Collaboration, M. O. Wascko, T. Nakaya, *et al.*, "Bringing the SciBar detector to the booster neutrino beam," `hep-ex/0601022`.

[67] **BooNE** Collaboration, I. Stancu *et al.*, "Technical design report for the 8 gev beam," tech. rep., FNAL, 2001. `http://www-boone.fnal.gov/publicpages/`.

[68] **BooNE** Collaboration, I. Stancu *et al.*, "Technical design report for the miniboone neutrino beam," tech. rep., FNAL, 2001. `http://www-boone.fnal.gov/publicpages/`.

[69] **BooNE** Collaboration, I. Stancu *et al.*, "The miniboone detector technical design report," tech. rep., FNAL, 2001. `http://www-boone.fnal.gov/publicpages/`.

[70] **MiniBooNE** Collaboration, A. A. Aguilar-Arevalo *et al.*, "The Neutrino Flux prediction at MiniBooNE," `arXiv:0806.1449 [hep-ex]`.

[71] **SciBooNE** Collaboration, K. Hiraide *et al.*, "Search for Charged Current Coherent Pion Production on Carbon in a Few-GeV Neutrino Beam," `arXiv:0811.0369 [hep-ex]`.

[72] K. Nitta *et al.*, "The K2K SciBar detector," *Nucl. Instrum. Meth.* **A535** (2004) 147–151, `arXiv:hep-ex/0406023`.

[73] **SciBooNE** Collaboration, K. Hiraide, "The SciBar detector at FNAL booster neutrino experiment," *Nucl. Phys. Proc. Suppl.* **159** (2006) 85–90.

[74] M. Yoshida *et al.*, "Development of the readout system for the K2K SciBar detector," *IEEE Trans. Nucl. Sci.* **51** (2004) 3043–3046.

[75] M. Yokoyama, "Scibar/ec electronics system." SciBooNE-DAQ-001 available at `http://www-sciboone.fnal.gov/sciboone/daq/notes.html`.

[76] **CHORUS** Collaboration, E. Eskut *et al.*, "The CHORUS experiment to search for $\nu_\mu \to \nu_\tau$ oscillation," *Nucl. Instrum. Meth.* **A401** (1997) 7–44.

[77] S. Buontempo *et al.*, "Construction and test of calorimeter modules for the CHORUS experiment," *Nucl. Instrum. Meth.* **A349** (1994) 70–80.

[78] S. Buontempo *et al.*, "Performance of the CHORUS lead-scintillating fiber calorimeter," *Nucl. Phys. Proc. Suppl.* **54B** (1997) 198–203.

[79] M. Wascko. Personal communication, 2008.